

Cite this: DOI: 10.1039/c9cs00883g

## Regulating electrodeposition morphology of lithium: towards commercially relevant secondary Li metal batteries

 Jingxu Zheng,<sup>a</sup> Mun Sek Kim,<sup>b</sup>  Zhengyuan Tu,<sup>c</sup> Snehashis Choudhury,<sup>b</sup> Tian Tang<sup>a</sup> and Lynden A. Archer<sup>b</sup>  \*<sup>ad</sup>

Lithium, the lightest and most electronegative metallic element, has long been considered the ultimate choice as a battery anode for mobile, as well as in some stationary applications. The high electronegativity of Li is, however, a double-edged sword—it facilitates a large operating voltage when paired with essentially any cathode, promising a high cell-level energy density. It is also synonymous with a high chemical reactivity and low reduction potential. The interfaces a Li metal anode forms with any other material (liquid or solid) in an electrochemical cell are therefore always mediated by one or more products of its chemical or electrochemical reactions with that material. The physical, crystallographic, mechanical, electrochemical, and transport properties of the resultant new material phases (*interphases*) regulate all interfacial processes at a Li metal anode, including electrodeposition during battery recharge. This Review takes recent efforts aimed at manipulating the structure, composition, and physical properties of the solid electrolyte interphase (SEI) formed on an Li anode as a point of departure to discuss the structural, electrokinetic, and electrochemical requirements for achieving high anode reversibility. An important conclusion is that while recent reports showing significant advances in the achievement of highly reversible Li anodes, e.g. as measured by the coulombic efficiency (CE), raise prospects for as significant progress towards commercially relevant Li metal batteries, the plateauing of achievable CE values to around  $99 \pm 0.5\%$  apparent from a comprehensive analysis of the literature is problematic because CE values of at least 99.7%, and preferably  $>99.9\%$  are required for Li metal cells to live up to the potential for higher energy density batteries offered by the Li metal anode. On this basis, we discuss promising approaches for creating purpose-built interphases on Li, as well as for fabricating advanced Li electrode architectures for regulating Li electrodeposition morphology and crystallinity. Considering the large number of physical and chemical factors involved in achieving fine control of Li electrodeposition, we believe that achievement of the remaining  $\sim 0.5\%$  in anode reversibility will require fresh approaches, perhaps borrowed from other fields. We offer perspectives on both current and new strategies for achieving such Li anodes with the specific aim of engaging established contributors and newcomers to the field in the search for scalable solutions.

Received 13th December 2019

DOI: 10.1039/c9cs00883g

[rsc.li/chem-soc-rev](http://rsc.li/chem-soc-rev)

## 1. Introduction

### 1.1 Broader context

Electrochemical cells as platforms for storing electrical energy have a history of more than two hundred years. Alessandro

Volta first described the operating principles for such cells and in 1800 demonstrated the first device-scale examples capable of generating continuous electric current.<sup>1,2</sup> Since then, electrochemical battery technology has progressed in fits and starts, but the most sustained periods of progress coincide with advances in human society in diverse domains—implanted medical devices,<sup>3</sup> mobile phones to robots,<sup>4</sup> cars.<sup>5</sup> In short, batteries have emerged as an essential, enabling technology for modern life<sup>6</sup>—that in turn drives demand for better devices for storing and transporting electrical energy.

Particularly after the millennium the challenge of achieving electrochemical energy storage in battery systems at densities

<sup>a</sup> Department of Materials Science and Engineering, Cornell University, Ithaca, NY 14853, USA. E-mail: laa25@cornell.edu

<sup>b</sup> Department of Chemical Engineering, Stanford University, Stanford, CA 94305-4125, USA

<sup>c</sup> Global R&D Department, Gotion Inc., Independence, OH 44131, USA

<sup>d</sup> Robert Frederick Smith School of Chemical and Biomolecular Engineering, Cornell University, Ithaca, NY 14853, USA

competitive with fossil fuels has emerged as a global priority. The supply of fossil fuels, including petroleum, natural gas and coal, is finite and non-renewable but presently accounts for approximately 80% of the total U.S. energy consumption. It is therefore a serious concern that the depletion times for the

commercially most important fossil fuels—oil, coal and gas—are approximately 24, 96 and 26 years, respectively.<sup>7</sup> Energy generation using fossil fuels is also based on combustion processes that first convert the stored-up chemical energy to heat. Subsequent conversion of this energy to mechanical or



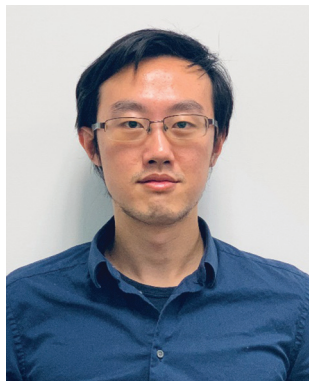
**Jingxu Zheng**

*Jingxu (Kent) Zheng is currently a third-year PhD student at Cornell University. Under Prof. Lynden Archer's supervision, his current research mainly focuses on the design of reversible metallic anodes in batteries, including Li, Zn, Al, etc., by regulating their electrodeposition morphologies. Jingxu earned his bachelor's degrees in engineering and in history from Shanghai Jiao Tong University in 2017. His undergraduate research focused on the atomic-scale characterization of crystalline materials and their phase transformations using advanced transmission electron microscopy. He has co-authored more than 40 research papers during his academic career.*



**Mun Sek Kim**

*Mun Sek Kim received BS degree in Chemical Engineering from University California, Berkeley in 2014 and MS degree in Chemical & Biomolecular Engineering from Cornell University in 2016. He was a research scientist as in lieu of military serve at Korea Institute of Science and Technology in Energy Storage Research Center from 2016 to 2019. He is now a PhD student in Chemical Engineering department at Stanford University. His research is mainly focused on the secondary battery systems especially for lithium metal anodes.*



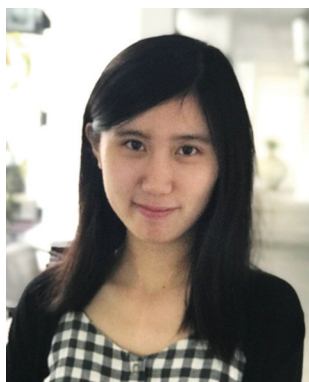
**Zhengyuan Tu**

*Zhengyuan Tu received his PhD from the Department of Materials Science and Engineering at Cornell University, with a research focus on hybrid nanomaterials and engineered interphase for high energy alkali metal-based batteries. He currently serves as a research scientist at the global R&D center at Gotion Inc. to develop advanced battery systems for electric vehicles and energy storage.*



**Snehashis Choudhury**

*Snehashis Choudhury received his PhD in Chemical and Biomolecular Engineering from Cornell University in 2018, with a focus on development of organic-inorganic hybrid nanomaterials for electrolytes and interphases in alkali metal batteries. He is currently a postdoctoral researcher in the Department of Chemical Engineering at Stanford University.*



**Tian Tang**

*Tian Tang is a second-year PhD student in the Department of Materials Science and Engineering at Cornell University. She joined Prof. Archer's research group in 2018, and currently works on the design of artificial interphases for high-performance Li metal anodes and Si-based anodes. Tian received her bachelor's degree in Engineering from Zhejiang University.*



**Lynden A. Archer**

*Lynden A. Archer is the James A. Friend Family Distinguished Professor of Engineering and the David Croll Director of the Cornell Energy Systems Institute (CESI). His research focuses on transport properties of complex fluids—including polymers, organic-inorganic hybrids, and electrolytes—at liquid-solid interfaces. His work also considers applications of these materials for cost-effective electrochemical energy storage.*

electrical energy is for fundamental thermodynamic reasons less efficient than the direct conversion of chemical energy to electricity in an electrochemical cell. Additionally combustion of all fossil fuels produce  $\text{CO}_2$ ,<sup>8</sup> a greenhouse gas that has been implicated in climate change.<sup>9,10</sup> Thanks to the rapidly falling costs of energy generation from renewable technology, including solar and wind, the levelized unit cost is now at levels, *i.e.*  $\$0.05 \text{ kW}^{-1} \text{ h}^{-1}$ ,<sup>11</sup> which makes them competitive with traditional combustion-based energy generation technologies. However, the inherent intermittency and variability of energy generated from the sun or wind is problematic because it renders energy generation from either source non-dispatchable and hence immensely difficult to integrate in an electric power network/grid with complex duty demand. Availability of electrical energy storage technologies that can be manufactured at scale and which are able to achieve amortized unit costs competitive with the levelized cost of production would provide fresh, even disruptive opportunities for the design of cost-effective, dispatchable electric power systems (see Fig. 1A<sup>12</sup>).

Currently, battery systems cost too much and suffer from a variety of technical and safety limitations that have limited market penetration. For example, though costs have been falling rapidly in recent years, the unit cost of Li batteries currently range from approximately  $\$20 \text{ kW}^{-1} \text{ h}^{-1}$  (Li-S) to  $(\$120\text{--}\$200) \text{ kW}^{-1} \text{ h}^{-1}$  (Li-ion). This makes them uncompetitive for large scale energy storage applications.<sup>13</sup> The argument for developing highly reversible battery systems is then explicit; the amortized unit power cost of a battery system is inversely proportional to its life time, since the acquisition cost is an essentially one-time investment, which also includes the manufacturing and installation costs.<sup>14</sup> As a short-term goal, a Li-ion battery system with

an installed cost of  $\$100 \text{ kW}^{-1} \text{ h}^{-1}$  would require a cycle life of at least 3000 cycles to achieve an amortized that is comparable to the levelized cost of energy generation from renewables. Since one would ideally like the overall system (generation + storage) levelized costs to be competitive with present day costs of electricity, lower cost batteries and much longer battery lifetimes are clearly required. For example, at an installed cost of  $\$20 \text{ kW}^{-1} \text{ h}^{-1}$ , a Li-S battery that achieves a cycle life of 1000 cycles, would add only  $\$0.02$  to the overall power cost. It is straightforward to show that if the life time of such metal anode Li batteries can exceed 2000 cycles their amortized cost become competitive with other lower cost and more earth abundant candidate battery anode chemistries, *e.g.* Zn<sup>15</sup> and Al.<sup>16</sup>

Fossil fuels play as important a role in powering transportation as in electric power generation. In addition to cost and cycle life, batteries able to replace fossil fuels in the transportation sector must achieve high energy density. For example, the energy density of a commercial grade gasoline is  $12.2 \times 10^3 \text{ W h kg}^{-1}$  which is 1–2 orders of magnitude higher than the  $1\text{--}3 \times 10^2 \text{ W h kg}^{-1}$  (*e.g.*  $280 \text{ W h kg}^{-1}$  for graphite-LiCoO<sub>2</sub>,  $400 \text{ W h kg}^{-1}$  for Zn-MnO<sub>2</sub>) that can be achieved in contemporary battery technology. As illustrated in Fig. 1B and C advanced lithium battery designs in which the graphite anode is replaced with a metallic lithium foil, in principle provide the most promising battery platform for bridging the large gap in energy density between fossil fuels and batteries. We note that prototype versions of such batteries in which Li metal or Li-Al metal alloy anodes were paired with a TiS<sub>2</sub> cathode were among the first examples of rechargeable Lithium batteries pioneered by Whittingham.<sup>17</sup> Later studies by Goodenough<sup>18</sup> showed that replacing the TiS<sub>2</sub> with a LiCoO<sub>2</sub> cathode would nearly double the cell potential (from 2 V to approximately 4 V); opening the way

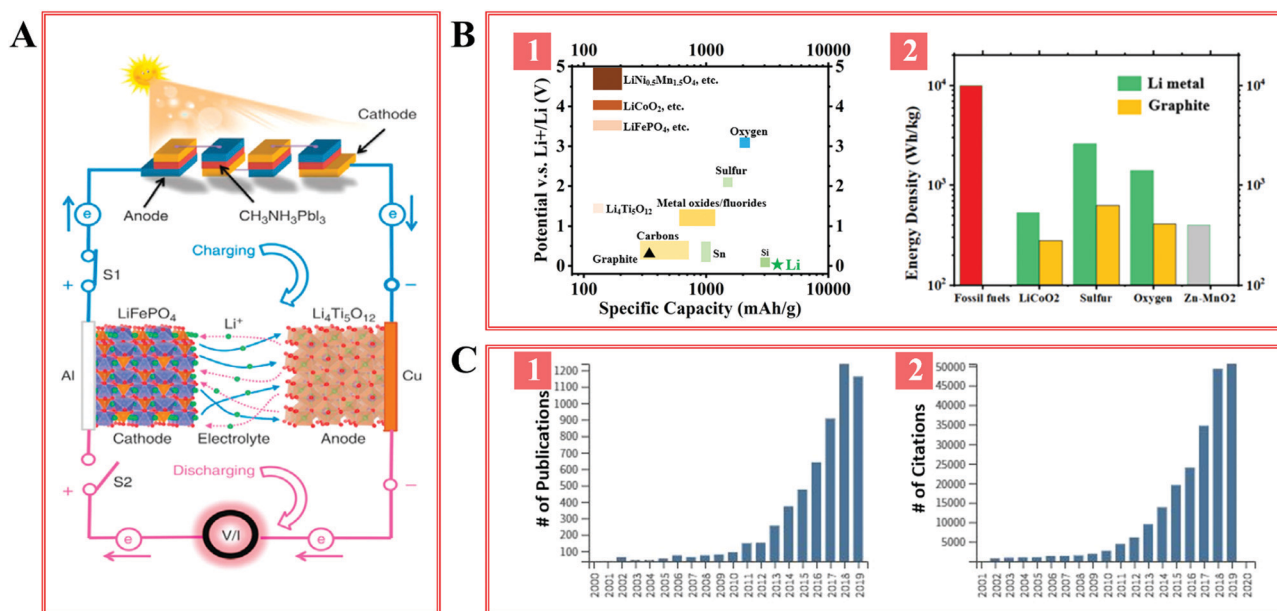


**Fig. 1** Motivations for developing stable Li metal anode. (A) The role of battery systems in green energy industry. Reprinted with permission from ref. 12. Copyright (2015) Springer Nature. (B-1) Electrochemical potentials and specific capacities of Li-based battery chemistries. (B-2) Energy densities of fossil fuels (red), Li metal batteries (green), Li-ion batteries (yellow) and Zn-MnO<sub>2</sub> battery (grey) as a reference. (C-1) number of publications and (C-2) number of citations related to "Lithium metal anode", up to October, 2019. Database: Web of Science.

for today's commercial Li-ion battery chemistries that took advantage of Yoshino's<sup>19</sup> discovery that use of graphitic carbons as the host for Li at the anode dramatically improved the cycle life, stability, and manufacturability of lithium batteries. For this troika of discoveries and for the associated transformational changes to human life brought about in the 28 years since the Li-ion batteries' commercialization by Sony in 1991, Whittingham, Goodenough, and Yoshino shared the 2019 Nobel Prize in Chemistry. In search of better batteries that offer higher storage capacity and in some cases lower cost than possible with Li-ion technology, there has been a recent global reviving of published papers (Fig. 1C-1) and number of citations (Fig. 1C-2) in battery designs that use Li metal as the anode.<sup>20</sup> The fundamental obstacle though is that in order to create lithium-metal batteries capable of meeting the safety and cycle life requirements for practical implementation, scalable approaches are required both for regulating Li metal electrodeposition and for achieving levels of electrode reversibility that are comparable to the graphite anode in state-of-the-art Li-ion batteries.

## 1.2 Promise and fundamental requirements for practical lithium metal anodes

Lithium metal has been dubbed the Holy Grail battery anode material for at least three reasons that underscore the promise of Li metal batteries. First, Li has the lowest electrochemical potential which translates into a high battery working voltage when paired with a variety of cathode chemistries. Second, Li is the lightest metal, yielding a high storage capacity per unit anode mass. Finally, a Li metal anode provides an energy-dense source of  $\text{Li}^+$  ions, which makes the anode compatible with a broad range of cathodes, including non-lithiated earth-abundant materials (*e.g.*  $\text{MnO}_2$ , S,  $\text{O}_2$ ,  $\text{CO}_2$ ), which provides more versatility in the battery design than possible with any other electrode chemistry.

In order to realize the promise of the Li anode, fully reversible Li plating/stripping must occur upon battery cycling. When this condition is achieved in a battery, the mass of Li in the anode exactly matches that required to fully lithiate the cathode material, and the so-called negative to positive (N:P) capacity ratio = 1 : 1, Fig. 2A. In practice, this condition is rarely achieved<sup>21,22</sup> with the result that most published results touting

advances in Li metal anode stability do so in cells in which  $\text{N/P} \gg 1$ . In each plating/stripping cycle, a portion of the Li metal is irreversibly lost, meaning that the high cycle life of the battery is achieved only by adding enough Li to compensate for this loss. A quantitative measure of the plating/stripping reversibility, the coulombic efficiency (CE = amount of Li that can be stripped/the amount of Li that is plated), may be used to roughly estimate the excess of Li required for a desired cell operating lifetime under specified operating conditions. Fig. 2B-1 illustrates this point more concretely by reporting the dependence of battery cycle life on CE for Li metal batteries with N:P ratio equal to 1 : 1. Currently, the end-of-life of a battery is defined as the time at which its discharge capacity decreases to 80% of the initial value. Under this definition, in order to achieve a cycle life of 200 cycles, a CE of 99.9% is required, which has so far not been possible with any battery utilizing a Li metal anode.

One might naively think that the cycle life achieved for a specified CE can be arbitrarily increased by increasing the N:P ratio (*e.g.* when the N:P ratio is 3 : 1, a cycle life of 200 requires a CE of around 99% (Fig. 2B-2), which has already been reported in multiple literatures). Unfortunately, as illustrated in Fig. 2A the specific capacity of the Li metal anode is a strong decreasing function of the N:P ratio. Such that from the perspective of the amount of energy stored per unit mass, a Li metal battery with N:P ratio greater than 3 : 1, corresponding to an effective specific capacity of  $1000 \text{ mA h g}^{-1}$  for the anode, is no more advantageous than a Li-ion cell in which the graphite anode is replaced by Sn. We note further that for the more typical case studied in the majority of papers reported thus far,  $\text{N:P} \geq 10$ , the Li metal anode for all of its theoretical promise offers no practical improvement in the amount of energy stored per unit mass that a state-of-the-art Li-ion battery. Hence, it is imperative that in a practical lithium metal cell, the N:P ratio is kept below 3:1 (true specific capacity =  $1286 \text{ mA h g}_{\text{Li}}^{-1}$ ), preferable below 1.2:1, (true specific capacity =  $3216 \text{ mA h g}_{\text{Li}}^{-1}$ ) and best exactly at 1 : 1 (true specific capacity =  $3860 \text{ mA h g}_{\text{Li}}^{-1}$ ) in order to realize the promise of this "Holy Grail" anode material chemistry in practical batteries. Of note is that, the last situation where no extra Li is prestored is particularly, called "anode free", is particularly desired since no

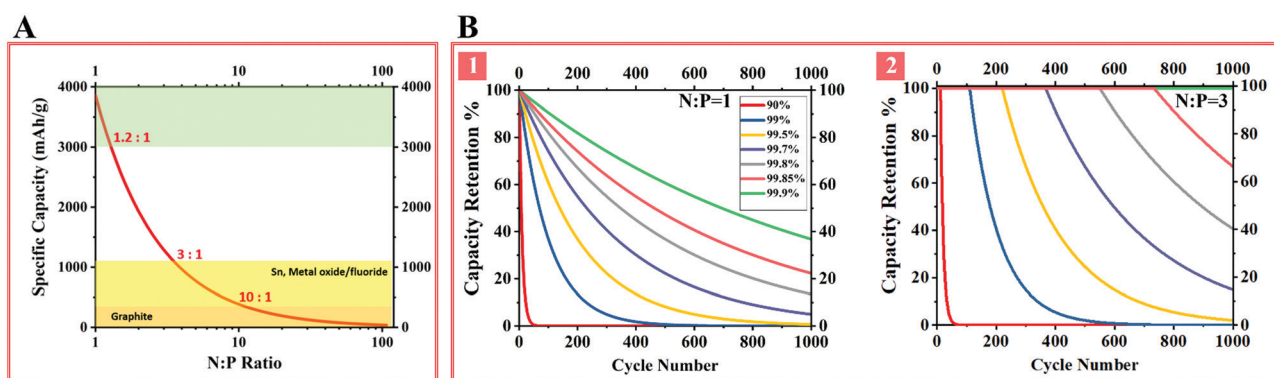


Fig. 2 Reversibility requirement for a practical lithium metal anode. (A) Dependence of specific capacity of Li metal anode on N:P ratio. Capacity retention of Li metal under a (B-1) N:P = 1 : 1 condition and a (B-2) N:P = 3 : 1 condition.

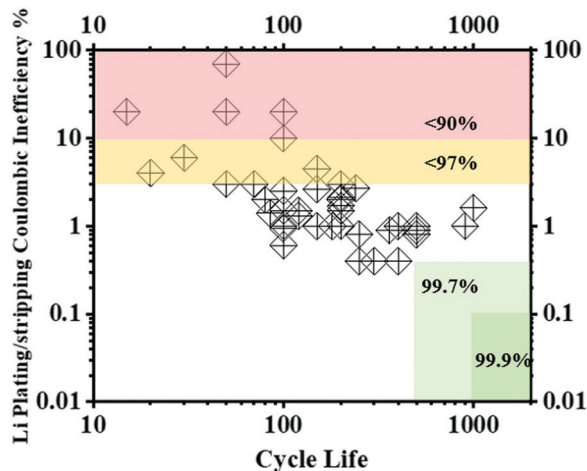


Fig. 3 Summary of Li plating/stripping reversibility reported in the literature.

handling of highly reactive, air sensitive Li metal is required during manufacturing.

Fig. 3 summarizes the Li anode reversibility in terms coulombic inefficiencies ( $CIE = 1 - CE$ ) and corresponding cycle life reported for Li metal anodes in the literature. For clarity Coulombic Inefficiency (y-axis) is plotted in a logarithmic scale. The details are tabulated in Table 1. It should be noted further that the cycle life (x-axis) values reported in the figure is a measure of how many cycles the specified CE value can be maintained and is therefore different from the cycle life of a full battery discussed in the previous paragraph. The figure shows that great progress has been made towards a close to unity Li plating/stripping CE, from  $\sim 50\%$  in 1974 to the state-of-the-art values of  $99\% \pm 0.5\%$  in 2018 and 2019. The plateauing at 99.0–99.5% apparent from the figure is nonetheless a source of concern because as depicted in Fig. 2B, the compounding effect of the remaining 0.5% on cycle life is substantial. The plateau may also be interpreted as proof that further advancement in improving Li plating/stripping CE is getting increasingly difficult and could reflect fundamental chemical stability limits imposed by the nature of currently available Li metal foils and electrolytes. We note however, that anodes composed of Na, a more reactive counterpart of Li, have been reported to achieve plating–stripping efficiencies of  $>99.9\%$  in ether-based electrolytes and  $>99.5\%$  in conventional carbonates<sup>23</sup> indicating that the analogous search for scalable strategies for achieving CEs that overcome this remaining 0.5% Li is an achievable priority research direction. Fig. 4 provides a roadmap that we believe could be used to guide such research towards commercially-viable Li metal anodes. The development of practical battery systems that utilize Li metal anode relies on a high Li plating/stripping efficiency that is directly determined by the electrodeposition morphology of Li, as will be discussed in Section 1.3. Multiple factors play nonnegligible roles in the electrodeposition of Li in a coupled manner, meaning that this process is fundamentally complicated; it however also means that, there are ample opportunities that one could use to regulate Li growth, on the basis of the decoupling of their roles in the process.

Apart from the need for developing Li anodes with high reversibility, anode and electrolyte configurations that facilitate safe operations under normal running conditions, as well as in battery abuse scenarios, is a requirement for practical interest in Li metal battery technology. It is in our view the most important driver for research aimed at achieving fine control of Li electrodeposition morphology during recharge. It is understood for instance that non-planar, rough or dendritic electrodeposition of Li during battery recharge compound already serious safety concerns about any of the aprotic liquid electrolyte used in Li-ion batteries. Here, however, details of the various morphologies formed upon recharge of a Li anode matter in terms of whether the anode fails as a result of poor reversibility, generation of undesirable side products, or due to dendrite-induced short circuiting.<sup>24,25</sup> Wu *et al.* for example reported that two types of dendrites are created during continuous Li plating/stripping: one mainly causes an increase in impedance, while the other aggressively propagates towards the counter electrode causing battery short.<sup>26</sup> Similarly fatal Li dendrite penetration was reported in solid-state electrolyte.<sup>27</sup> A less abrupt but similarly problematic issue is gassing. Gaseous products are continuously generated during cycling as Li undergoes parasitic chemical reactions with the electrolyte.<sup>28</sup> For example,  $Li + C_3H_4O_3(EC) \rightarrow Li_2CO_3 + C_2H_4$ .<sup>29</sup> Gassing could lead to serious safety issues, such as ignition of the highly flammable volatile organic solvents vented into the ambient atmosphere.<sup>30</sup> The continuous gassing is in the first place because of the high reactivity dictated by the thermodynamics, but also caused by the creation of fresh, unpassivated Li surface upon unregulated electrodeposition.<sup>31</sup> Particularly, the dendritic, porous nature of electrodeposited Li renders a large exposed surface area for the undesirable reaction. This effect can be quantitatively evaluated using a simple geometric model. Assuming a  $3 \text{ mA h cm}^{-2}$  areal deposition capacity, the total surface area of Li fibers that are  $2 \mu\text{m}$  in diameter is 20 times higher than that of compact Li. Despite that a larger surface area enhances the reaction kinetics during Li plating/stripping as revealed in a recent simulation study,<sup>32</sup> the aggravated side reactions over cycling could pose additional challenge in designing safe Li metal anode with prolonged cycle life. Achieving compact Li morphology by regulating the electrodeposition is therefore necessary for practical Li metal batteries.

Even Li-ion batteries using intercalation anodes, such as graphite and Si, suffer from analogous issues faced by Li metal batteries. Tens of thousands cases of Li-ion battery fires/explosions have been reported;<sup>31</sup> these accidents are caused by instabilities associated with either the cathode or the anode. The working potentials of the intercalation anode materials are close to Li redox couple, *i.e.*  $-3.04 \text{ V vs. SHE}$ . This means that side reactions occurring *via* reduction mechanisms can proceed owing to the low potential, generating gaseous products.<sup>33</sup> The low potentials of the intercalation anodes also indicate that, under certain charge conditions (*e.g.* battery abuse, low temperature), Li cations can be electrochemically reduced and plated onto the anode in the form of metal,<sup>34–36</sup> rather than intercalate into the host material in the form of ion. The undesirable Li plating is thought to be the key

Table 1 Summary of Li plating/stripping coulombic efficiency (CE) reported in the literature

Year	CE	Cycle life	Electrolyte	Strategy	Current density (mA cm <sup>-2</sup> )	Areal capacity (mA h cm <sup>-2</sup> )	Ref.
2017	0.996	225	4 M LiFSI in DME	Substrate	2	0.3–1.2	394
2019	0.994	100	LiTFSI/LiNO <sub>3</sub> in DOL/DME	Temperature	0.5	1	185
2019	0.994	100	LiPF <sub>6</sub> in EC/DMC/FEC	3D framework	0.8	8	44
2018	0.992	250	10 M LiFSI in DMC	Electrolyte	0.2	1	395
2018	0.992	500	LiPF <sub>6</sub> in FEC/FEMC/HFE	Electrolyte	0.2	1	396
2019	0.991	450	LiTFSI/LiNO <sub>3</sub> /LiFSI in DOL/DME	Electrolyte	0.5	1	397
2015	0.991	400	LiTFSI/Li <sub>2</sub> S <sub>8</sub> /LiNO <sub>3</sub> in DOL/DME	Electrolyte	2	1	273
2015	0.991	500	4 M LiFSI in DME	Electrolyte	0.2	1	264
2017	0.991	360	LiTFSI/Py <sub>13</sub> TFSI in DOL/DME	Electrolyte	1	1	249
2019	0.990	400	LiTFSI/LiNO <sub>3</sub> in DOL/DME	Substrate	2	1	368
2019	0.990	900	LiTFSI/LiNO <sub>3</sub> in DOL/DME	Substrate	1	1	398
2019	0.990	180	LiTFSI/LiNO <sub>3</sub> in DOL/DME	Substrate	0.5	1	399
2019	0.990	140	10 M LiFSI in DMC	Substrate	1	1	400
2017	0.990	90	LiTFSI in DOL/DME	Interphase	0.5	1	148
2018	0.990	150	LiTFSI/LiNO <sub>3</sub> in DOL/DME	3D framework	0.5	0.5	401
2014	0.990	150	LiTFSI/LiNO <sub>3</sub> /Li <sub>2</sub> S <sub>8</sub> in DOL/DME	3D framework	0.25	1	402
2018	0.990	200	LiTFSI in DOL/DME	3D framework	0.5	2	403
2017	0.990	150	LiPF <sub>6</sub> /AlCl <sub>3</sub> in EC/DMC/DEC	Electrolyte	0.5	2	404
2014	0.990	120	LiFSI/LiTFSI in DOL/DME	Electrolyte	0.25	0.625	267
2019	0.989	150	LiTFSI/LiNO <sub>3</sub> in DOL/DME	3D framework	0.5	1	405
2018	0.987	250	LiTFSI/LiNO <sub>3</sub> in DOL/DME	Interphase	1	2	406
2017	0.987	120	LiTFSI/LiNO <sub>3</sub> in DOL/DME	Interphase	0.5	1	386
2016	0.986	200	LiTFSI/LiNO <sub>3</sub> /Li <sub>2</sub> S <sub>8</sub> in DOL/DME	3D framework	1	2	407
2019	0.985	350	LiTFSI/LiNO <sub>3</sub> in DOL/DME	Interphase	0.5	0.5	408
2019	0.985	100	LiTFSI/LiNO <sub>3</sub> in DOL/DME	Charging protocol	0.5	1	409
2017	0.985	200	LiTFSI/LiNO <sub>3</sub> in DOL/DME	3D framework	1	3	410
2017	0.985	100	LiTFSI/LiNO <sub>3</sub> in DOL/DME	3D framework	1	1	411
2015	0.985	50	LiTFSI/LiNO <sub>3</sub> /Li <sub>2</sub> S <sub>8</sub> in DOL/DME	3D framework	0.5	1	412
2017	0.985	600	LiTFSI/LiNO <sub>3</sub> in DOL/DME	3D framework	1	2	413
2017	0.985	38	LiPF <sub>6</sub> in FEC/DMC	Electrolyte	0.5	1	414
2017	0.985	300	LiTFSI/LiNO <sub>3</sub> in DOL/DME	Interphase	0.25	0.5	352
2017	0.983	200	LiPF <sub>6</sub> in EC/EMC/FEC	Interphase	0.5	1	415
2019	0.983	160	LiTFSI/LiNO <sub>3</sub> in DOL/DME	3D framework	1	2	416
2017	0.982	100	LiTFSI/LiNO <sub>3</sub> in DOL/DME	Interphase	1	1	344
2017	0.980	350	LiPF <sub>6</sub> in EC/DEC/FEC	Interphase	0.5	1	417
2016	0.980	300	LiPF <sub>6</sub> in EC/DEC/FEC/VC	Substrate	0.5	1	418
2018	0.980	100	LiPF <sub>6</sub> in FEC	Electrolyte	0.5	2	155
2017	0.980	200	LiTFSI/LiNO <sub>3</sub> in DOL/DME	Substrate	1	1	419
2016	0.980	90	LiTFSI/LiNO <sub>3</sub> in DOL/DME	Separator	0.5	0.5	420
2017	0.980	100	LiPF <sub>6</sub> in EC/DEC/FEC	Electrolyte	0.1	0.5	151
2018	0.979	200	LiTFSI in DOL/DME	3D framework	1	1	421
2015	0.979	120	LiTFSI/LiNO <sub>3</sub> in DOL/DME	3D framework	1	1	422
2016	0.977	80	LiTFSI/LiNO <sub>3</sub> in DOL/DME	Interphase	1	3	423
2016	0.976	240	LiTFSI/LiNO <sub>3</sub> in DOL/DME	Interphase	1	0.5	424
2017	0.975	100	LiTFSI/LiNO <sub>3</sub> in DOL/DME	3D framework	0.5	1	425
2019	0.974	150	LiTFSI/LiNO <sub>3</sub> in DOL/DME	3D framework	1	1	426
2018	0.972	120	LiTFSI/LiNO <sub>3</sub> in DOL/DME	Interphase	0.5	1	339
2018	0.970	200	LiTFSI/LiNO <sub>3</sub> in DOL/DME	3D framework	1	2	427
2014	0.970	50	LiPF <sub>6</sub> in EC/DEC	Substrate	0.5	1	428
2016	0.970	150	LiPF <sub>6</sub> in EC/DMC/FEC	3D framework	0.5	2	429
2016	0.970	180	LiFNFSI in DOL/DME	Electrolyte	0.5	1.5	430
2016	0.970	250	LiTFSI/LiNO <sub>3</sub> in DOL/DME	3D framework	0.5	1	431
2017	0.950	70	LiPF <sub>6</sub> in VC	Electrolyte	0.5	2	432
2017	0.950	100	LiTFSI in DOL/DME	Interphase	0.2	0.1	433
2017	0.950	300	LiTFSI/LiNO <sub>3</sub> in DOL/DME with 20 nm pore-size Al <sub>2</sub> O <sub>3</sub>	Electrolyte	0.25	0.25	201
2016	0.950	50	LiTFSI/LiNO <sub>3</sub> /CsNO <sub>3</sub> in DOL/DME	Interphase	0.5	0.5	343
2004	0.950	50	LiPF <sub>6</sub> /VC in EC/DMC	Electrolyte	0.6	0.44	143
2012	0.940	45	LiPF <sub>6</sub> in EC/EMC	3D framework	2	4	434
2016	0.930	50	LiFSI/LiTFSI in DOL/DME	Substrate + electrolyte	0.5	0.5	435
2015	0.920	100	LiPF <sub>6</sub> in EC/DEC	Separator	0.5	1	436
2017	0.900	50	LiPF <sub>6</sub> in EC/DEC	Interphase	1	2	437
2016	0.900	120	LiPF <sub>6</sub> in EC/DMC/LiF	Electrolyte	0.25	1	149

cause of battery thermal runaway.<sup>37</sup> To understand the Li metal plating process in Li-ion batteries, a three-electrode system, which includes a reference electrode, was used to monitor the potential evolution on the anode during battery charge at different rates.<sup>38</sup>

The results show that the anode potential can drop below 0 V vs. Li<sup>+</sup>/Li when the battery is charged to certain voltages (*i.e.* 3.93 V for 0.5C and 1C; 4.10 V for 0.2C, at 25 °C). A potential below 0 V vs. Li<sup>+</sup>/Li means that the Li plating reaction is electrochemically allowed.

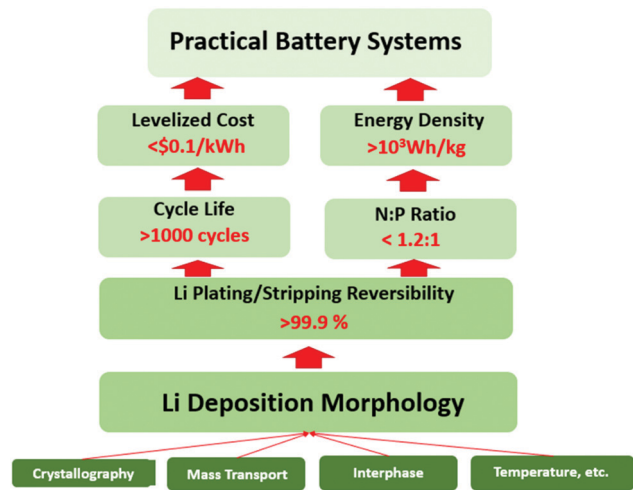


Fig. 4 A roadmap for developing practical lithium metal battery systems.

At sub-ambient temperatures, Li plating becomes more prominent owing to the slower  $\text{Li}^+$  intercalation kinetics.<sup>39</sup> An *in situ* neutron diffraction study revealed that at a temperature of  $-2^\circ\text{C}$ , 5.5% and 10% of the charged capacity should be attributed to Li metal plating when the charge currents are  $C/2$  and  $1C$ , respectively.<sup>40</sup> The authors further claimed that at lower current densities, *e.g.*  $C/20$ ,  $\sim 3\%$  of charging capacity is contributed by Li metal plating. Based on modelling studies, Yang *et al.* claim that SEI growth in the anode over cycling reduces the electrode porosity and thereby slows down the intercalation kinetics, giving rise to the onset of Li metal plating. The presence of Li metal further lowers the porosity by forming additional SEI,<sup>41</sup> resulting in a positive feedback loop that causes exponential increase of Li plating capacity in each cycle.<sup>42</sup> The “dead” Li metal deposits formed during cycling act as an additional layer that restrict ion transport, giving rise to a growing resistance.<sup>43</sup> Therefore, uncontrolled Li growth poses issues associated with battery safety and battery performance in not only Li metal batteries but also commercial Li-ion batteries. On

this basis, we conclude that regulating Li metal electrodeposition emerges as a question of broad, commercially-relevant interest.

### 1.3 Fundamental sources of irreversibility of the Li metal anode

The irreversible Li loss during cycling is thought to stem primarily from two origins: (1) chemical instability and (2) physical instability (Fig. 5A). The former describes Li metal’s propensity for chemical reactions with other battery components, *e.g.* the electrolyte, during which it converts into other Li-containing species, *e.g.*  $\text{Li}_2\text{CO}_3$ , where the Li is no longer metallic. The latter describes Li metal’s propensity for physical isolation from the electrochemical system upon reversibly plating/stripping, during which it loses its electrical connection to the current collector though it is still metallic Li, called “orphaned” or “dead” Li.<sup>44</sup>

Although the amount of overall Li loss can be easily quantified by coulombic inefficiency, the individual contributions of these two factors are under active investigation. The existence of dead Li has been consistently reported in the literature based on XRD,<sup>44</sup> SEM,<sup>45</sup> optical microscopy,<sup>46,47</sup> *etc.* Recent reports show that the formation of “dead” Li in some cases account for the majority of the Li irreversibility. Zheng *et al.* for example used a nonplanar conductive architecture as Li deposition substrate to evaluate the contribution of dead lithium to the overall plating/stripping irreversibility.<sup>44</sup> The authors found that, although the Li is deposited in obvious dendritic morphology that has a greater surface exposure area, an above 99.4% Li plating/stripping efficiency is maintained over 100 cycles. This observation implies that maintaining electrical contact with the Li electrodeposits throughout the charging and discharging process in a Li metal anode is a requirement for high Li reversibility. Deng *et al.* visualized the formation of “dead” sodium metal using operando optical microscopy and confirmed that control of electronic access to metal electrodeposits plays a key role in achieving high levels of electrode reversibility.<sup>48</sup> In stripping, the authors reported that large mossy electrodeposits can be disconnected from the current collector. The consequence is an extremely low plating/stripping

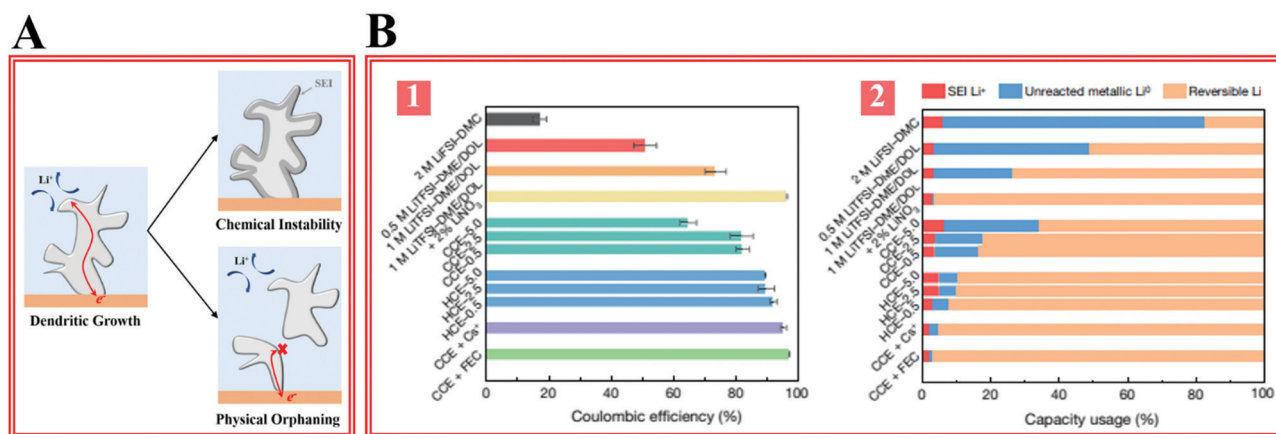


Fig. 5 The origins of Li loss. (A) Irregular, noncompact growth of Li leads to chemical and physical instabilities. Reprinted with permission from ref. 44. Copyright (2019) American Chemical Society. (B-1) Li plating/stripping coulombic efficiency in different electrolytes. (B-2) Quantification of Li loss via different mechanisms. Reprinted with permission from ref. 50. Copyright (2019) Springer Nature.

CE of only 3%. Cheng *et al.* visualized the morphology evolution in Li plating/stripping by in operando transmission X-ray microscopy.<sup>49</sup> They suggest that the dead lithium is mainly generated by dendritic Li electrodeposits at high current density, as opposed to the mossy Li deposits at low current density. A further observation is that dead lithium, once formed, will be pushed out towards the counter electrode and remain inactive throughout the cycling. The amount of the chemically-reacted and the physically-disconnected Li in multiple electrolytes can be quantified by titration gas chromatography.<sup>50</sup> The amount of “dead” Li is strongly dependent on the electrolyte recipe (from 80% in LiFSI–DMC to ~0% in CCE–FEC), while the amount of chemically reacted Li is almost independent of the electrolyte chemistry (Fig. 5B).

While the relative importance of chemical and physical instability remains a matter for ongoing study in the field, there is consensus that both effects are exacerbated by the propensity of Li to electrodeposit in irregular, non-planar morphologies at planar electrodes. Ideally, an anode metal should deposit in a regular, compact and smooth morphology to preserve sharp interfaces between the metal electrode and other cell components. A large body of work has now established that Li in contrast deposits as irregular, fragile structures that typically bear no obvious structural correlation to the geometry of the substrate at which the deposition occurs. This behavior is problematic for at least three reasons: (1) it creates a high surface area of Li, leading to continuous parasitic reactions; (2) the high-aspect ratio electrodeposits easily break away from the current collector upon stripping at the base; and (3) the Li electrodeposits gradually propagate through the separator, causing fatal, dangerous battery short. Consequently, we believe efforts to precisely control the Li electrodeposition morphology are therefore a high priority to achieve the required breakthroughs in reversibility of Li metal anodes needed for practical battery systems.

As a first step towards understanding and overcoming the factors that presently limit control of Li electrodeposit morphology, section two of the Review will focus on the fundamental aspects of Li electrodeposition. Armed with a complete picture of the factors determining Li deposition morphology, section three will review promising strategies for regulating and stabilizing Li deposition. On this basis, we will outline areas that we believe are priorities for future research towards the goal of enabling practical rechargeable batteries that utilize Li metal anodes.

## 2. Understanding electrodeposition at the Li metal electrode

Electrodeposition of metals is a two-century-old process that has been used in multiple industries for creating metal coatings on electrically conductive substrates. Enormous effort has been devoted to understanding process conditions that enable fine control of the electrodeposit morphology and crystal structure. Fundamentally, metal electrodeposition is an electrochemically

driven phase transition in which a new solid phase is formed at interfaces where electron and ion conduction are in direct contact, *e.g.* the interface between the electron-conducting current collector and the ion-conducting electrolyte. The morphology of the new solid phase, *i.e.* the metal electrodeposit, is determined by the interplay of multiple factors including chemistry, crystallography, mass transport and others such as temperature, mechanical pressure, *etc.* For metals such as Li that are chemically reactive and undergo reduction at low potentials, new material phases (*e.g.* the solid–electrolyte interphase (SEI)) may also form at the metal/electrolyte interface, providing additional sources of complexity in understanding their morphology during electrodeposition. As a result, whereas the factors that prevent fine control of metal electrodeposition in some commercially important cases (*e.g.* Cu and Ni plating) are well understood within the classical Nernst–Planck theoretical framework, understanding of the stability limits of Li electrodeposition require additional physics.<sup>29</sup> Fortunately, the advancement in characterization techniques has in recent years enriched the toolbox of methods that can be used to interrogate Li electrodeposition morphology, which has accelerated the progress towards a more complete understanding of Li metal electrodeposition.

### 2.1 Crystallography, texturing, and morphological evolution

The metal electrodeposits formed at the Li anode during battery charging are crystals in most cases, which by their nature are anisotropic. It is then understood that despite the large variety of macroscopic shapes a certain metal can be induced to adopt, the underlying crystal structure at the atomic scale remains invariant and as illustrated in Fig. 6 can induce texturing of the overall electrodeposit morphology. Indeed in many situations, the shape of electrodeposited crystals reflects the underlying lattice symmetry (see Wulff plots in Fig. 7<sup>51</sup>), which indicates the equilibrium external shape of a crystal structure, even in regimes dominated by mass transport. Simulation results show that anisotropic metals (*e.g.* HCP Zn) tend to grow in a fractal, branching dendritic manner, while metals whose crystal structure is more isotropic (*e.g.* BCC Li) grow needle-like dendrites.<sup>52</sup> Experimentally, Glocker and Kaupp showed in 1924 by X-ray diffraction that textures (also known as preferred/predominant orientation) are present in the electrodeposition of Cu, Ag, Ni, Cr and Fe.<sup>53</sup> Compared with metals of cubic lattice symmetry, hexagonal close packing (HCP) metals that have more anisotropic lattice, *e.g.* Zn, demonstrate a stronger relation between the intrinsic crystal symmetry and the electrodeposition morphology.<sup>15,54</sup>

The texturing of metal electrodeposits is mainly determined by two factors: substrate and the bath conditions.<sup>55</sup> The substrate is either epitaxial or inert. When the lattice misfit between the substrate material and the metal electrodeposit is <15%, the electrodeposits can be epitaxially templated within a certain thickness; otherwise the substrate does not affect the texturing. Bath conditions include current density, temperature, pH, ions in the electrolyte, *etc.* Regarding bath conditions, when the electrodeposition is performed under conditions close to equilibrium, *i.e.* low current density and high temperature, metals have a

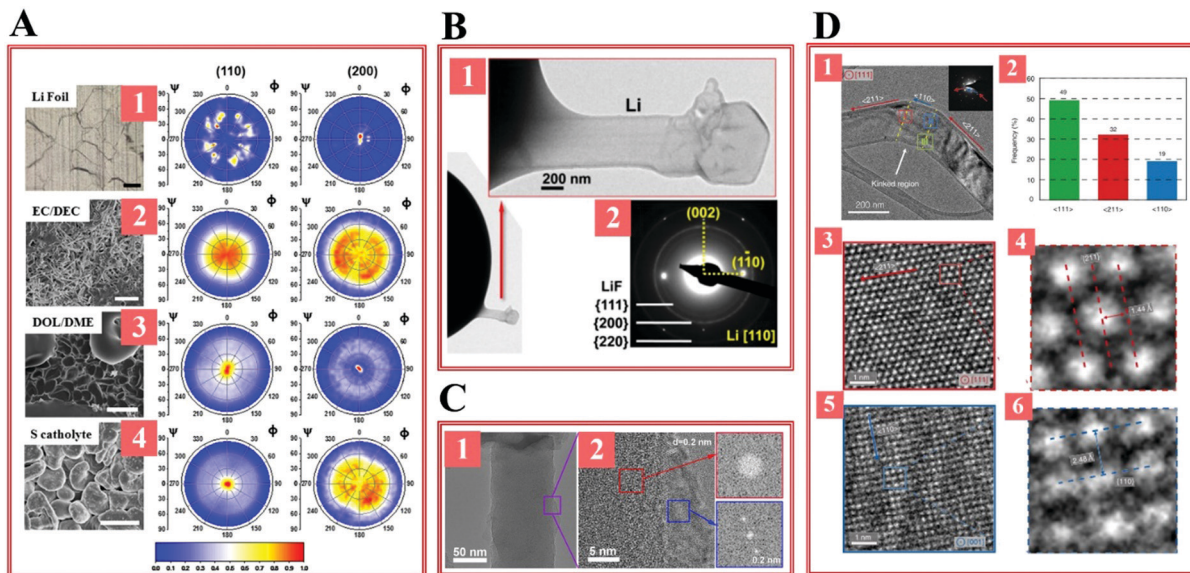


**Fig. 6** Influence of crystal anisotropy on Li electrodeposition. (A) X-ray diffraction characterization of texturing in Li foil and Li deposits. Reprinted with permission from ref. 58. Copyright (2017) National Academy of Sciences. (B) TEM characterization showing single crystalline Li electrodeposit. Reprinted with permission from ref. 61. Copyright (2011) AIP Publishing. (C) TEM characterization showing amorphous Li electrodeposits covered by polycrystalline LiF. Reprinted with permission from ref. 63. Copyright (2017) American Chemical Society. (D) Atomic-resolution cryo-TEM characterization showing single crystalline Li electrodeposits. Reprinted with permission from ref. 65. Copyright (2017) AAAS.

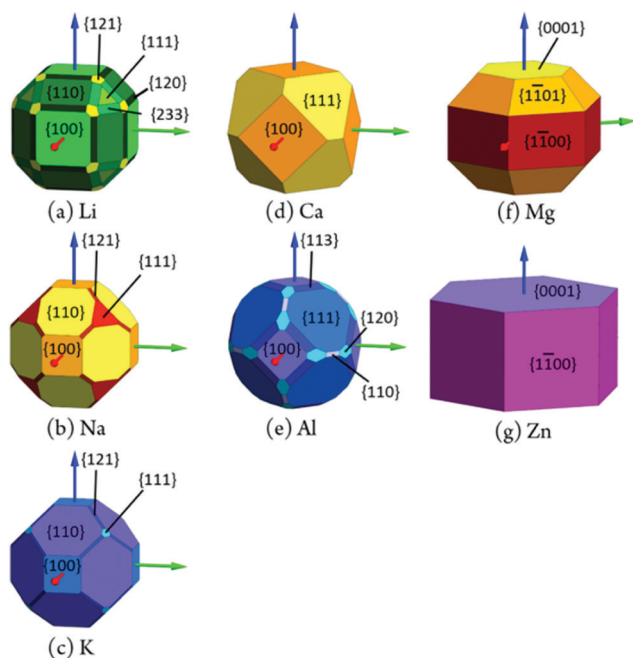


**Fig. 7** Wulff plots of metals of interest as battery anode. Reprinted with permission from ref. 51. Copyright (2019) American Chemical Society.

propensity to expose their close-packed facets, *i.e.* (111) for FCC, (0001) for HCP and (110) for BCC. Whereas under conditions far away from equilibrium, *i.e.* high current and low temperature, the deposited metals tend to grow outwards along the close-packed directions, *i.e.* [110] for FCC,<sup>56</sup> [112̄0] for HCP and [111] for BCC.

The role of texturing in Li electrodeposition is receiving increasing attention. The growth of wire-like (also sometimes

referred to as “dendritic” or “mossy”) Li deposits has for example been interpreted as a result of crystal anisotropy. Stark *et al.* imaged the Li electrodeposition by *in situ* optical microscopy.<sup>57</sup> The results show that the growth of the Li occurs mainly on the dendrite tips, suggesting that the deposition rate at the tips are far faster than that that on the sidewalls of the Li deposit. The authors hypothesized certain crystal facets are preferred over the others during the electrochemical growth, resulting in the preferential growth of Li along certain directions. Direct confirmation of texturing is provided by crystallographic characterization techniques including X-ray diffraction (XRD) and transmission electron microscopy (TEM). The former is able to provide statistical information about the crystal texturing; while the latter visualize the crystallographics of individual crystallites. Shi and co-workers used X-ray diffraction to study the texturing of Li deposited on Cu foil from three electrolytes:<sup>58</sup> (E-1) 1 M LiPF<sub>6</sub> in EC/DEC, (E-2) 1 M LiTFSI + 1% LiNO<sub>3</sub> in DOL/DME and (E-3) 5 M S<sub>8</sub> + 1 M LiTFSI + 1% LiNO<sub>3</sub> in DOL/DME. The results (Fig. 6A) show that, in the E-1 electrolyte, Li deposits in the form of whiskers and does not show texturing; whereas in E-2 and E-3, the roundish Li deposits are (110) textured; in other words, the (110) planes of Li are parallel to the substrate. The authors attribute this feature to the presence of inhibitor that decreases the exchange current density. We note that, since Li has a BCC crystal structure, (110) is the close-packed plane of Li, suggesting a low surface energy. This observation underscores the important role that crystal structure plays in determining Li deposition morphology.

Advanced transmission electron microscopy has emerged as a powerful tool to resolve crystallographic characteristics of electrodeposition of Li.<sup>59</sup> Zeng *et al.* visualized the lithiation of

an Au substrate followed by subsequent Li dendrite growth on it,<sup>60</sup> although no crystallographic information was extracted due to the oxidation of Li into Li<sub>2</sub>O. It suggests that the observation needs to be performed under strict protection. Liu *et al.* reported the formation of long, single crystalline Li metal fibers covered with a thin layer of polycrystalline LiF in an *in situ* TEM observation on the lithiation process of SnO<sub>2</sub> and Si, respectively (Fig. 6B).<sup>61</sup> In fact, Li metal and related SEI structures are highly sensitive to beam damage, moisture and other factors that can introduce artifacts, making the TEM characterization of electrodeposited Li very challenging.<sup>59,62</sup> Unlike normal inorganic crystals, the TEM observation of Li preferably needs to be performed under cryogenic condition (*i.e.* cooled by liquid N<sub>2</sub>) with low electron doses to prevent artifact generation. Advanced cryo-TEM characterizations have revealed spatially resolved crystallographic information about Li deposition. Wang *et al.* reported that at nucleation stage (0.04 mA h cm<sup>-2</sup>), Li deposits are amorphous coexisting with some crystalline LiF<sup>63</sup> (Fig. 6C). Current density can influence the crystallinity of Li. Wang *et al.* concluded that the formation of amorphous Li domains are favored at low current densities (*e.g.* 0.1 mA cm<sup>-2</sup>).<sup>64</sup> At normal deposition current density of 2 mA cm<sup>-2</sup>, Li *et al.* showed that the Li nanowires are single crystalline. These nanowires primarily grow along three directions:  $\langle 111 \rangle_{\text{Li}}$  (49%),  $\langle 110 \rangle_{\text{Li}}$  (32%) and  $\langle 211 \rangle_{\text{Li}}$  (19%)<sup>65</sup> (Fig. 6D). It is further claimed that the growth along  $\langle 111 \rangle_{\text{Li}}$  direction can maximize the surface area of  $\langle 110 \rangle_{\text{Li}}$  close-packed planes. He *et al.* also reported the observation of  $\langle 211 \rangle_{\text{Li}}$  as the axial crystallographic direction of the Li whiskers.<sup>66</sup>

There is evidence that crystal texturing is related to the wire-like growth pattern observed in Li electrodeposition. However, many fundamental questions remain that should provide opportunities for fruitful future investigations. For example, it is so far unknown if an amorphous/glassy state exist before the nucleation of crystalline Li. Although amorphous structures have been reported in lithiation/Li plating experiments, further proof (*e.g.* using EELS<sup>67</sup>) is needed to conclude that they are elemental Li. It is likewise unclear if the wire-like Li growth observed in experiment are a direct result of crystal anisotropy. Statistical methods like XRD can provide data that complements TEM characterization of individual Li crystals. It is also unknown how the deposition conditions, including current density, electrolyte, areal capacity, influence Li's crystallinity and texturing behavior. It is reported that these factors can affect the morphology and reversibility of Li metal, but insufficient efforts have been given to understanding the role Li crystallinity and/or texturing may play. Finally, it is largely unknown how correlations between the deposited Li crystals and the underlying crystal structure of the substrate may affect Li electrodeposition morphology. Recently, our group showed that an epitaxial substrate can effectively lock Zn electrodeposits into particular crystallographic orientations to regulate electrodeposition of Zn in a battery anode (see illustration in Fig. 8A).<sup>15</sup> The whole electrochemical epitaxy in Zn anode includes two steps: hetero- and homo-epitaxy (Fig. 8A-1). The former describes the influence of the substrate on the initial Zn deposition layers;

the latter refers to the tendency that new Zn deposits follow the crystallographic features set by the initial Zn deposition layers. The governing principle of an epitaxial growth is the system's tendency to minimize interfacial energy upon the creation of new phase(s). When the new phase is crystalline and has a small lattice misfit (*i.e.*  $\delta < 15\%$  as an empirical rule) with the substrate, the so-called "coherent" interface can form between the new phase and the substrate, showing a lower interfacial energy compared with "semi-coherent" or "incoherent" interfaces. This type of phenomena has been widely discussed in multiple fields whose research interests involve the growth of a crystalline phase, *e.g.* heat treatment of metals,<sup>68-70</sup> chemical vapor deposition<sup>71,72</sup> and electrochemical deposition.<sup>73-75</sup> Since the charging process of a Zn-ion battery is in essence a electrochemical deposition process of Zn metal, it can be hypothesized that a substrate that has low lattice misfit with Zn can epitaxially regulate the growth of Zn (Fig. 8A-2). As revealed by X-ray diffraction and electron microscopy, the intrinsic growth pattern of Zn upon electrodeposition is to form plate-like microstructures, which preferentially expose the close-packed (0002)<sub>Zn</sub> basal plane. This observation is consistent with the analysis we made earlier in this subsection, and with the simulation results based on the anisotropic energy landscape of Zn crystals.<sup>51</sup> Whether this concept can work as effectively for Li remains an open question, owing to the presence of a passivating SEI at the Li reduction potentials. Evidence for homoepitaxial growth of Li has been reported in LiBr-LiNO<sub>3</sub> in tetraglyme electrolyte system under O<sub>2</sub> atmosphere.<sup>76,77</sup> In this case, the authors claim that the newly-deposited Li follows the crystallographic orientation and the shape of the polycrystalline Li substrates (Fig. 8B). Scanning electron microscopy and electron back scattered diffraction (EBSD) mapping were utilized to characterize the homoepitaxial growth process. To illustrate the concept, the authors first show that the grain boundaries of Li crystals are observable after electrochemical stripping (Fig. 8B-1-B-4). Then, Li was plated onto the same polycrystalline Li foil; the morphology hardly changes after the plating (Fig. 8B-5 and B-6). The EBSD characterizations do not suggest any significant alteration in terms of crystallographics (Fig. 8B-7-B-10). These results indicate that the plated Li undergoes a homoepitaxial process in this electrolyte. The authors attribute the uniform, homoepitaxial growth of Li to the formation of a thin, Li<sub>2</sub>O-enriched SEI layer. In contrast, a thick SEI layer formed in a "LiNO<sub>3</sub>-only" electrolyte can disrupt the homoepitaxial growth of Li, engendering dendritic Li deposition. The reported homoepitaxial growth of Li is, on one hand, essential to the successful epitaxial regulation of Li – the effect of heteroepitaxy alone will be rather limited, if homoepitaxy is blocked by SEI. On the other hand, a heteroepitaxy substrate that maintains its physical and chemical properties is necessary – as one strips a large portion of the Li pre-stored in the anode under low N:P ratio conditions, the homoepitaxy mechanism will fail. Searching for heteroepitaxial substrates for Li appears as the crucial next step. Promising progress has been reported by Li *et al.* in their

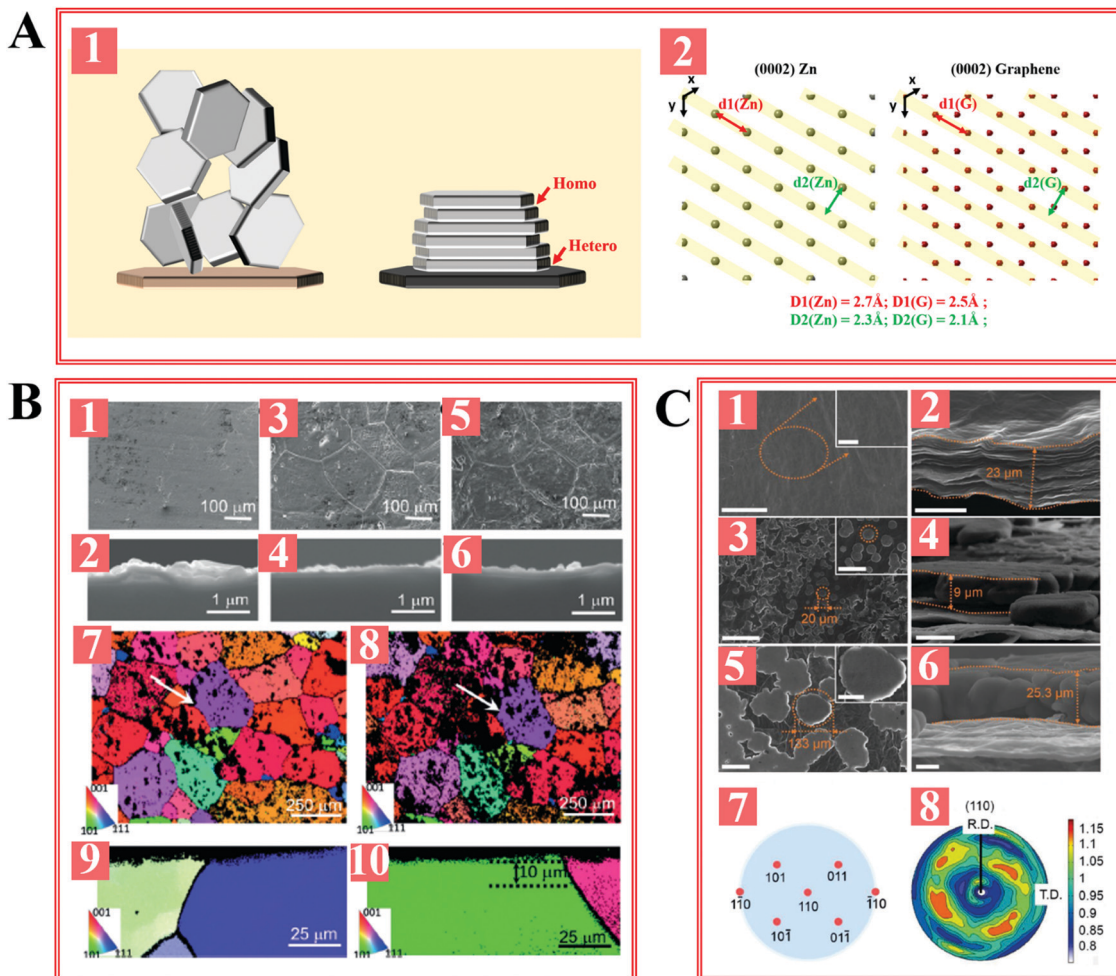


Fig. 8 Electrochemical epitaxy in battery anodes. (A) Schematic diagram illustrating the epitaxial growth of Zn metal on graphene. Reprinted with permission from ref. 15. Copyright (2019) AAAS. (B) Homoeptitaxy of Li observed in a tetraglyme-based electrolyte. Reprinted with permission from ref. 77. Copyright (2018) John Wiley and Sons. (C) Textured Li meta deposits on reduced graphene oxide. Reprinted with permission from ref. 78. Copyright (2019) John Wiley and Sons.

recent paper (Fig. 8C), where they show that Li deposition on graphene is planar and (110)-textured, although the lattice matching between HCP graphene and BCC Li is not ideal.<sup>78</sup>

## 2.2 Mass transport limitations and instability

In any metal electrodeposition processes, metal cations that are electrochemically generated at one electrode are reduced at the surface of the anode. The process can therefore be analyzed in a similar way to mass transport of ions across the interelectrode phase in an electrolyte bounded at one end by cation-selective interface. For a dilute electrolyte, this transport is governed by the Nernst-Planck (N-P) equation:  $N_i(x) = -D_i \frac{\partial C_i(x)}{\partial x} - \frac{z_i F}{RT} D_i C_i \frac{\partial \phi(x)}{\partial x} + C_i v(x)$ , where the terms describe diffusion, migration and convection that contribute to the ionic flux  $J_i$ .<sup>79</sup> Assuming the contribution from convection is negligible, the N-P equation has a simple analytical solution for any symmetric binary electrolyte,<sup>80</sup> and the current at steady state,  $J$ , can be related to the potential difference  $V$  between the electrodes by the following expression:

$$J \equiv F \sum_i z_i N_i = \left( \frac{4zcFD}{\delta} \right) \left( 1 - e^{-\frac{FV}{2RT}} \right) / \left( 1 + e^{-\frac{FV}{2RT}} \right)$$
. Here  $F$  is the Faraday constant;  $z$  the electrolyte valency;  $c$  the salt concentration in the electrolyte;  $D$  the ambipolar diffusivity for the ions in the electrolyte solvent; and  $\delta$  is diffusion boundary layer thickness. When  $V \geq 8RT/F$  ( $RT/F$  is the thermal voltage), the exponential terms vanish and the expression shows that the current density reaches an asymptotic limit  $J = J_{\text{lim}} \approx \left( \frac{2zcFD}{L} \right)$ , termed the “diffusion-limited” or limiting current density (also called the limiting current density), where we’ve considered the limiting case where the diffusion boundary layer thickness is the inter-electrode spacing  $L$ .  $J_{\text{lim}}$  is then evidently the highest mass transport flux that can be sustained by diffusion in the electrolyte.<sup>80,81</sup> In other words, above this current density, diffusion cannot sustainably replenish the metal cations near the electrode surface. The concentration of cations therefore falls to zero in a fluid layer near the electrode after a characteristic time,  $t_{\text{Sand}} = \pi D \frac{(z_0 c_0 F)^2}{4(J_a)^2}$ ,<sup>82</sup> termed Sand’s time required for the non-uniform ion distribution to form.

The existence of a charge depleted, or extended space-charge layer (ESCL) near the electrode can drive non-planar, dendritic electrodeposition of any metal by two interrelated mechanisms. In the first mechanism, newly arriving metal cations preferentially deposit on protrusions (*e.g.* created by earlier deposits or by natural irregularities on the metal electrode surface) outside the ion-depleted zone. This so-called morphological instability is self-reinforcing and ultimately results in fractal, dendritic electrodeposition patterns.<sup>79,80,83,84</sup> In the second mechanism, the large electric fields required to drive ion migration through the ESCL may couple with charge fluctuations in the fluid to drive a hydrodynamic instability termed electroconvection.<sup>85–89</sup> Electroconvection is advantageous in some situations (*e.g.* electro dialysis) because it augments diffusion to increase the ionic current in an electrolyte above the diffusion limit (*i.e.* over-limiting conductance);<sup>88–90</sup> it is undesirable in others (*e.g.* electrodeposition) because the electroconvective fluid motions are non-uniform in space (see inset in Fig. 9A) and time and create localized stagnation flow that produces bursts of cation flux at a metal electrode. These spatially non-uniform fluxes produce non-planar deposits, which grow much more rapidly than the morphological instability that may arise by electro-migration and diffusion alone.<sup>89,91–95</sup>

The essential prediction that  $J_{\text{lim}}$  sets a current density limit, beyond which uniform metal electrodeposition is fundamentally unstable has been verified in experimental studies using metals such as Cu, Zn, and Sn in aqueous electrolyte media.<sup>93,94,96</sup> The spontaneously appearance of convective rolls

at  $V \geq 8RT/F$  has likewise been verified by both Direct Numerical Simulation (DNS) studies<sup>90,94,95</sup> and very recently by operando tracer particle visualization experiments.<sup>96</sup> The latter studies show that the hydrodynamic instability develops more quickly and produce stronger convective fluxes in electrolytes with low salt concentration and at high overpotentials. The N-P analysis reveals that the electroconvective instability produces flow with dominant components  $\langle \mathbf{v} \rangle$  normal to the electrode and  $\langle \mathbf{u} \rangle$  parallel to the electrode surface (Fig. 9A). Importantly, analysis of the strength of the  $\langle \mathbf{u} \rangle$  component of the flow as a function of distance from the electrode surface ( $y$ ), reveals a clear flow transition from a strong inner shearing flow near the electrode, in which  $\langle \mathbf{u} \rangle$  rises approximately linearly with  $y$ , to an outer flow in which  $\langle \mathbf{u} \rangle$  decays approximately exponentially with  $y$ . The transition is consistent with the idea that the ESCL thickness defines a boundary layer for the electroconvective flow, which when viewed from far away would create the impression that electrolyte moves with an electroconvective slip velocity,  $U_{F,s} = \frac{\epsilon}{\eta_F} L \cdot V^2$ , that increases quadratically with the applied voltage  $V$  and decreases linearly with the electrolyte viscosity,  $\eta_F$ , in the ESCL. It means that the strength of the inner convective flow and thereby the rate at which the non-planar electrodeposit grows can be manipulated both through the overpotential at the metal electrode and the viscosity of the electrolyte in the region closest to the electrode surface.

Among the first studies of mass transport effects on Li electrodeposition is work by Langenhuizen.<sup>97</sup> The author used

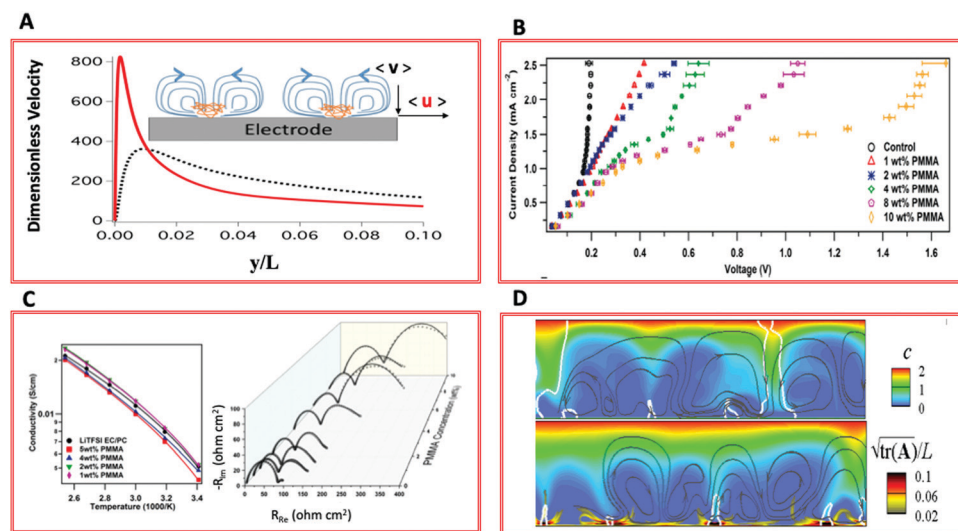


**Fig. 9** Suppressing electroconvective instabilities at the Li anode using ultra high molecular weight polymers as additives in liquid electrolytes. (A) Components of the velocity field near a cation selective membrane predicted by Direct Numerical Simulations (DNS) as a function of distance from the electrode normalized by the inter-electrode spacing  $L$ . The calculations are for  $V = 40RT/F$  and for  $\kappa^{-1}/L = 10^{-5}$ . Here  $\kappa^{-1}$  is the Debye screening length determined by the salt concentration in the electrolyte. The inset shows that the electroconvective flow has velocity components with non-zero average values both parallel  $\langle \mathbf{u} \rangle$  and normal  $\langle \mathbf{v} \rangle$  to the electrode surface. Reprinted with permission from ref. 95. Copyright (2019) American Physical Society. (B) Current voltage diagram measured in a 1 M LITFSI EC-PC electrolyte with varying concentrations of a high molar mass polymethyl methacrylate PMMA ( $M_w = 1.5 \times 10^6$ ,  $M_w/M_n = 1.1$ ). Reprinted with permission from ref. 81. Copyright (2018) AAAS. (C) Left: Ionic conductivity versus temperature and Right: Electrochemical impedance spectra at 25 °C for the electrolytes in (B) with varying PMMA concentration. Reprinted with permission from ref. 81. Copyright (2018) AAAS. (D) Velocity field, cation concentration field, and distribution of polymer chain stretch predicted by DNS. Reprinted with permission from ref. 95. Copyright (2019) American Physical Society.

a rotating disk electrode to determine the influence of an imposed, well-defined convective flow on the morphology of Li electro-deposits. A 1 M LiPF<sub>6</sub>-EC/DEC electrolyte with different amounts of HF additives (6, 9, 60 ppm). Under low HF concentration conditions (*i.e.* 6 and 9 ppm), the Li plating current density was enhanced at moderate rotation rate (625 rpm) due to convection. Furthermore, by scanning the potential in the negative direction to 200 mV vs. Li<sup>+</sup>/Li, the current–voltage ( $J$ - $V$ ) curve measured in the presence of convection do not show the typical overpotential maximum associated with poor mass transport to the electrode during Li plating, implying that the deposition is strongly influenced by mass transport in this regime.

Visualization studies using optical microscopy reveal a more direct relationship between electrodeposition morphology and transport. These studies show that Li electrodeposition can be divided into two stages—stage I, referred to as the incubation or nucleation stage is observed at low deposit capacities.<sup>98</sup> During this stage, no obvious non-planar Li growth is observed. In stage II, termed the initiation and dendritic growth phase, high-aspect ratio non-planar Li deposits form at the anode surface and grow aggressively to proliferate in the inter-electrode space. Nishikawa *et al.* observed that in a LiClO<sub>4</sub>-PC electrolyte<sup>99</sup> the deposit length in stage II is linearly proportional to the square root of time, indicating the process is governed by mass transport, as opposed to surface chemistry. The authors also studied the Li<sup>+</sup> ion concentration profile near the electrode by holographic interferometry. They found that the Li<sup>+</sup> concentration gradient is much larger around the rapidly growing dendrite tips than at the substrate surface. This is the expected result for mass-transport limited growth and is attributable to the uneven distribution of current density. The same group investigated the evolution of the diffusion boundary layer in a LiClO<sub>4</sub>-PC electrolyte<sup>100,101</sup> and reported that at current densities higher than 5 mA cm<sup>-2</sup> (approximately twice  $J_{lim}$  for the electrolyte studied), convective flow is initiated spontaneously in the electrolyte and serves as the main Li<sup>+</sup> transport mechanism. This finding is consistent with earlier studies by Huth *et al.*<sup>93</sup> for Cu deposition and has been confirmed in more recent tracer-particle visualization studies by Wei *et al.*<sup>81</sup> for a variety of metals, including Li and Na. It is also in qualitative agreement with operando transmission X-ray characterization reported by Cheng *et al.*<sup>49</sup> who reported that there is a distinct current density threshold for mass-transport limited, dendritic deposition of Li.

The study by Wei<sup>81</sup> provides insights into how one might design electrolytes to selectively suppress electroconvective flow near an electrode, without compromising bulk ion transport in a liquid electrolyte. Specifically, the authors observed that both the electroconvective flow and its effect on electrodeposition can be substantially reduced by adding small amounts of high molecular weight polymers to any liquid electrolyte. The only requirements appear to be that the polymer must be soluble in the electrolyte at the concentrations of interest and must be chemically stable at the electrodes of interest. As illustrated in Fig. 9B the added polymer also produces a substantial enlargement of the diffusion-limited transport regime, particularly at concentrations where rheology measurements show that the

long polymer chains begin to form physical entanglements in an electrolyte and where complementary Electrochemical Impedance Spectroscopy (EIS) analysis (Fig. 9C) reveal a large enhancement in film resistance of the electrode surface (see the emergence and enhancement in radius of the second semicircle), but a much smaller change in the electrolyte bulk ionic conductivity (see left panel of Fig. 9C). Both findings have been explained with the help of linear stability analysis of the N–P equations<sup>89</sup> and Direct Numerical Simulations (DNS),<sup>95</sup> which couple the Nernst–Planck equations to polymer constitutive equations to capture the effects of viscoelastic and normal stresses induced by polymer on the electroconvective flow. The DNS simulations reveal that the polymer normal stresses created by stretching of polymer chains in the inner region near the electrode surface (see heat/stretch map in Fig. 9D, lower panel) drive a substantial *back-flow*, which produces a more uniform cation flux, which in-turn favors more uniform electrodeposition. These discoveries indicate that polymer coatings either formed inadvertently (*e.g.* by adsorption of polymer chains dissolved in a liquid electrolyte or by electro-reduction and polymerization of electrolyte components) or by design (*e.g.* by application of coatings on the electrode to create Artificial Solid Electrolyte Interphases (see Section 3.2) provide potentially powerful mechanisms for limiting the effects of transport on stability of Li electrodeposition without substantially adding to the electrode mass or volume.<sup>102,103</sup>

While the body of work summarized in the previous sections indicates that mass transport plays a role in morphology control of Li electrodeposition, there is a substantial body of literature which reveals that the Li electrodeposition story, particularly at current densities  $< J_{lim}$ , involves additional physics that are not captured in the N–P theoretical framework. As an example, Nishida *et al.*<sup>104</sup> and Nishikawa *et al.* studied the electrodeposition of Li in LiTFSI-ionic liquid,<sup>105</sup> and in LiPF<sub>6</sub>-PC electrolytes.<sup>106</sup> The conclusion is consistent with the study of LiClO<sub>4</sub>-PC electrolyte that the dendrite growth after initiation is a mass transfer-controlled process. Interestingly, however, the authors observed that Li electrodeposition patterns at current densities well below  $J_{lim}$  (*e.g.* 0.1 and 0.2 mA cm<sup>-2</sup>), are much more non-planar and aggressive than those measured at higher current densities (*e.g.* 0.5, 2, and 5 mA cm<sup>-2</sup>). Specifically, long, fiber-like deposits, which are multiple times greater in length, are observed at low current densities of 0.1 and 0.2 mA cm<sup>-2</sup>. This observation indicates that the Li growth at low current densities is not governed by mass transport. More in-depth study is clearly needed to fully understand these observations. As remarkable, nonetheless, are the high-resolution optical microscopy studies of Steiger *et al.*,<sup>107,108</sup> which indicate that Li deposition is dominated by non-tip growth processes in defective regions (*e.g.* near the base) of initial, needle-like Li deposits. In other words, Li atoms are thought to “insert” into defective sites on Li deposits. In light of these findings the authors contend that non-planar Li electrodeposits ought not be termed dendrites, which are conventionally described as ramified structures where growth occurs near the tips but should instead be termed whiskers or needles for differentiation.

The recent report by Bai *et al.*,<sup>84</sup> provide a simple framework in which these seeming contradictory observations can be reconciled to develop a unified understanding. On the basis of experiments summarized in Fig. 10, the authors identified two stages of Li electrodeposit growth—mossy (root-growth) and dendritic (tip-growth). Specifically, Bai *et al.* investigated the morphological transition using direct optical visualization studies in tandem with indirect electrochemical analysis using the voltage–time ( $V-t$ ) curve (Fig. 10A). The electrodeposition of Li was first performed galvanostatically at  $2.61 \text{ mA cm}^{-2}$ . At the first stage of growth, the authors reported root-growing Li deposits in a porous, mossy morphology (Fig. 10A-1 and A-2), with the growth occurring at a weakly rising overpotential (Fig. 10A-6). After 40 minutes of deposition, the slope of the  $V-t$  curve rises rapidly with time and begins to fluctuate. At the same time, tip-growing Li dendrites are observed (Fig. 10A-3–A-5). Complementary theoretical analysis of the ion concentration profile (Fig. 10A-7) indicates that the transition coincides with development of an ESCL layer at the electrode surface, consistent with expectations based on classical transport theory.

The observations of Bai *et al.* seems reasonable, particularly considering that the classical theory that predicts dendrite formation by tip growth neither considers the effect of transport through an SEI on the structure of the ESCL,  $J_{\text{lim}}$ , or the salt concentration profile in the vicinity of the deposit. For example, results from a recent analysis of early-stage growth of Li electrodeposition shows that the ambipolar diffusion coefficient through interphases formed on Li in typical carbonate electrolytes can be seven or more orders of magnitude larger than the bulk diffusivity typically used to compute  $J_{\text{lim}}$ . It means

that even at current densities well below  $J_{\text{lim}}$ , local imperfections in a poorly formed or mechanically degraded SEI provide far more favorable pathways for arriving cations to access electrons that that transport through the SEI. The effect of electrode reaction kinetics on the rate at which arriving cations are reduced is also an important consideration. If the electrode kinetics are fast, a slow-down in ion transport rates in the SEI would favor random attachment of Li to all parts (tips, sides, base, *etc.*) of localized deposits, which would produce electrodeposits in a broad spectrum of morphologies (fibers, mosses, classical dendrites, *etc.*). The study by Rehnlund *et al.*, nonetheless underscore the danger of overgeneralizations.<sup>109</sup> The authors studied electrodeposition of Li in electrolytes with low salt concentration assisted by a supporting salt to minimize electromigration. Such electrolytes are uncommon in the Li batteries field but are important in high-rate metal electroplating because they eliminate the migration term from the N–P equation. Remarkably, SEM analysis of Li electrodeposits formed under these conditions show no evidence of dendritic (tip-growth) or mossy Li under plating conditions firmly in the diffusion-controlled regime. The results then imply that transport limitations do play a role in both mossy and classical dendritic electrodeposition of Li.

We close this section by drawing the reader's attention to an important body of work that analyzes the role of transport in the fuller context, where the ion flux also includes a term that accounts for the rate of Li ion disappearance as a result of the reduction reaction at the Li anode. To evaluate the importance of this effect, the so-called Second Damkohler Number is defined to measure the relative magnitude of chemical reaction

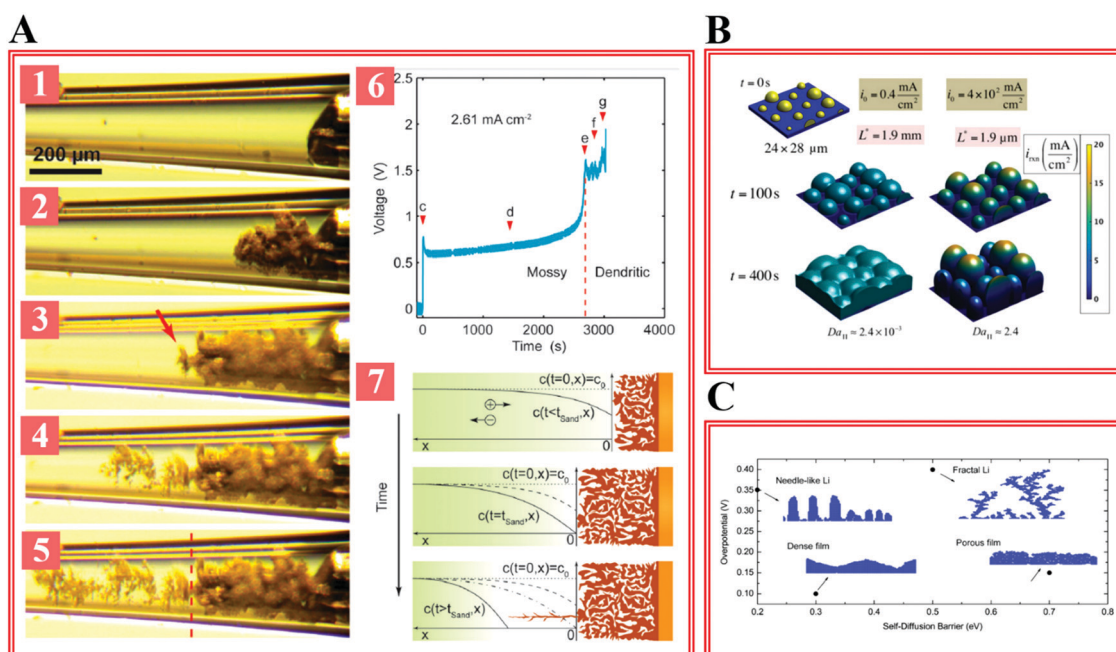


**Fig. 10** Influence of mass transport in Li electrodeposition. (A) Effect of  $\text{Li}^+$  ion transport in the liquid electrolyte. Reprinted with permission from ref. 84. Copyright (2016) The Royal Society of Chemistry. (B) Effect of competition between  $\text{Li}^+$  ion transport flux and chemical reaction rate. Reprinted with permission from ref. 111. Copyright (2017) Materials Research Society. (C) Effect of self-diffusion of Li atoms. Reprinted with permission from ref. 120. Copyright (2018) American Chemical Society.

flux to the mass migration flux:  $D_{a,II} \propto J_0/N_i$ , where  $J_0$  is the exchange current density of the electrode,  $N_i$  is the ionic flux due to diffusion and other transport processes in the electrolyte. As noted earlier, for current densities above  $J_{lim}$ , ion transport is diffusion limited and  $D_{a,II} \propto J_0/J_{lim} \propto J_0/\kappa$ , where we've made use of the relationship between  $J_{lim}$  and the ambipolar diffusivity  $D$  presented earlier, and the Nernst–Einstein expression relating  $D$  and  $\kappa$ . Likewise, at low or moderate overpotentials ( $V < 8RT/F$ ) (*i.e.* no electroconvection) and where a supporting electrolyte is used to eliminate the migration term,  $D_{a,II} \propto J_0/\kappa$ . Electrodeposition studies for Zn indicate that under conditions where  $D_{a,II} \ll 1$  uniform deposition is observed.<sup>52</sup> The finding is consistent with results from linear stability analysis of metal electrodeposition at a planar electrode,<sup>110</sup> which shows the morphological instabilities formed under conditions where the interfacial reaction is sluggish (*i.e.*  $D_{a,II} \ll 1$ ) are more broadly distributed in size, but grow more slowly than when  $D_{a,II} > 1$ . Computer simulations of Li electrodeposition performed by Enrique *et al.* confirms this finding and show that the Li deposition morphology is smoother on substrates with slow reaction kinetics, low exchange current density and in electrolytes with high ionic conductivity (Fig. 10B).<sup>111</sup> These findings can be understood in a straightforward physical manner. If the cation reaction flux is significantly smaller than its diffusion flux ( $J_0 < \kappa$ ), the deposition is always in a reaction kinetics limited region, which suppresses the uncontrollable propagation of a non-uniform interface. Therefore, high ionic conductivity is desirable in designing the electrolyte for Li metal anodes, especially in fast charging batteries.<sup>112</sup>

A non-uniform Li ad-atom distribution may not lead to non-uniform electrodeposition if the surface mobility of adatoms is high. The linear-stability analysis of Tikekar *et al.*,<sup>110</sup> indicates that a dimensionless group termed the Langmuir–Dukhin number ( $L_d \propto D_s/D$ ), which compares the rate of lateral transport at the electrode surface with that in the electrolyte bulk can be used to assess the influence of surface mobility. We note that the proportionality constant depends on the ad atom surface coverage and the inter-electrode distance, meaning that both chemical factors and geometrical factors may come into play in setting the actual value of  $L_d$ . The stability analysis shows, however, that while  $L_d > 10$  produces completely uniform electrodeposition, even  $L_d$  values as low as  $10^{-3}$  substantially reduces the non-planar growth rate of the most unstable modes. As noted earlier, a recent analysis of nucleation and early-stage growth of Li electrodeposits suggest that  $L_d$  may be as low as  $10^{-7}$ ,<sup>113</sup> in common carbonate electrolyte blends (*e.g.* diethylene carbonate (DEC)/ethylene carbonate (EC): 1 M LiPF<sub>6</sub>), perhaps explaining the notorious difficulty in achieving fine control of Li electrodeposition morphology in such electrolytes. External factors including mechanical stress,<sup>114</sup> surface tension,<sup>115</sup> temperature,<sup>116</sup> *etc.* that increase  $D_s$  would obviously increase the likelihood of achieving more uniform Li deposition.

The high  $D_s$  values for Mg in liquid electrolytes has been used to rationalize its tendency to form compact electrodeposits under certain conditions.<sup>117,118</sup> Davidson *et al.* theoretically analyzed Mg electrodeposition morphology based on a Damkohler

number  $D_a = \text{reaction rate/surface diffusion rate}$ .<sup>119</sup> The authors report that Mg forms film-like deposit when the surface diffusion is fast. Hao *et al.* also simulated the dependence of Li deposition morphology on this  $D_a$  under conditions where surface diffusion is rate limiting, and identified different regimes in terms of Li morphology<sup>120</sup> (Fig. 10C). Dense Li deposit films are predicted under conditions where the diffusion barrier and overpotential are both low. Jackle *et al.* performed DFT calculation to understand the atomic processes responsible for the much lower  $D_s$  values for Li and Na, compared to Mg.<sup>121</sup> The authors found that BCC metals such as Li and Na have a stronger homoepitaxy adsorption energy than Mg because BCC Li and Na are less close packed, and HCP Mg is closest packed. The authors further concluded that the Mg is much faster.<sup>122</sup> More fundamentally, the Ehrlich–Schwoebel barrier is used to describe difference between the barrier of an adatom to descend from an island *versus* undergo terrace diffusion. A smaller Ehrlich–Schwoebel barrier indicates a stronger tendency to grow in a layer by layer manner. For Li(100) and (110), the two most stable facets of Li,<sup>123</sup> the Ehrlich–Schwoebel barrier is 0.25 and 0.15 eV, respectively. In stark contrast, that value for Mg(0001) is “vanishing small”, *i.e.* very close to zero, again consistent with the observed tendency of Mg to form more compact electrodeposits. Joint-Density functional calculations indicate that these differences are exacerbated by the poorly conductive inorganic interphases formed on the Li electrode due to reduction of electrolyte components,<sup>124,125</sup> underscoring the need for better interphase control. We note also the recent study by Kim *et al.*,<sup>126</sup> which shows that high ad atom mobility in the SEI is not always beneficial for achieving fine control of Li electrodeposition. These authors combined experiments and DFT calculations to show that on surfaces where the energetics favor weak binding and clustering of Li ad atoms, a high ad atom surface mobility actually leads to more clustering and a greater propensity for Li to deposit in localized, non-planar morphologies.

### 2.3 The solid electrolyte interphase

The discussion in the last section revealed how rheological and surface transport characteristics of a material layer in direct contact with a Li metal electrode might be used to facilitate uniform electrodeposition by suppressing electroconvection or favoring surface rearrangement of already reduced Li ions. In reality, the combination of the lowest reduction potential ( $-3.04$  V *vs.* SHE) and among the highest chemical reactivity means that the material layer in physical contact with the Li anode rarely, if ever, shares the same chemistry as the electrolyte bulk—this is true whether the bulk electrolyte is a liquid or solid-state material, and especially in the presence of trace amount of water.<sup>127</sup> The presence of this solid–electrolyte interphase (SEI) layer on Li is considered the most differentiating factor involved in Li plating/stripping, compared with classical systems, *e.g.* Cu, Sn, Ag, *etc.* It is also the most cited reason for why the latter metals typically electrodeposit in non-planar morphologies only at  $J > J_{lim}$  (galvanostatic) or  $V > 8RT/F$  (potentiostatic), whereas reactive, electropositive metals such as Li and Na may exhibit these morphologies at essentially any current density or overpotential.

Knowledge of the composition, structure, transport properties, mechanics, and time-dependent evolution of the SEI are obviously key for understanding the role the SEI plays in Li electrodeposition, as well as for designing minimal artificial solid electrolyte interphases (ASEI) for Li compatible with long-term morphological and chemical stability. Over the past 40 years, sporadic efforts have been devoted to understanding the SEI at the battery anode.<sup>128–134</sup> The environmental sensitivity of Li means that even the surface chemistry of the native metal is complicated. Added to this is the fact that cycling of a Li anode in any electrolyte lead to substantial volume changes, which may lead to a reshuffling of interfacial constituents. Finally, X-ray and electron beam damage of organic polymer components of the SEI prevent its interrogation by the most powerful physical and electron spectroscopic methods. Until recently, these challenges were insurmountable and most early illustrations of the SEI on the Li anode were deduced from mosaic models first introduced by Peled.<sup>128</sup> As illustrated in Fig. 11A, the popular picture of the SEI on Li is of a multi-component, compartmentalized surface film that is relatively enriched in inorganic species in the inner part (closest to the Li metal electrode) and has a higher content of organic, polymeric species in the outer part close to the liquid electrolyte is derived from such models. How this SEI configuration varies with

electrolyte composition? How its composition and transport properties vary from place to place on the electrode or with distance normal to the electrode surface? How the mix of components change during cycling of the battery anode? And, how any of the hypothetical interfacial components regulate the Li electrodeposition morphology are all open questions that provide fertile opportunities for both fundamental and applications focused research. These effects are nonetheless often speculated about in the literature, typically based on what are arguably incomplete information collected from different sources, *e.g.* FTIR, XPS, SEM, XRD, AFM, *etc.* The search for complete answers then remains a central requirement for rapid advances towards practical Li metal batteries.

One generic perspective is that structural heterogeneity of a mosaic SEI leads to heterogeneous physical, transport and mechanical properties, which promote preferential deposition of Li through regions where gradations in thickness, composition, or mechanical integrity (*e.g.* cracks) facilitates faster Li<sup>+</sup> transport (Fig. 11B).<sup>83,134</sup> This explanation is reasonable but does not take into account the detailed composition and structure of SEI and is not able to explain with satisfactory detail the many shapes of Li electrodeposits reported in the literature. Unravelling this puzzle and using knowledge developed in the process to rationally design SEI that promotes

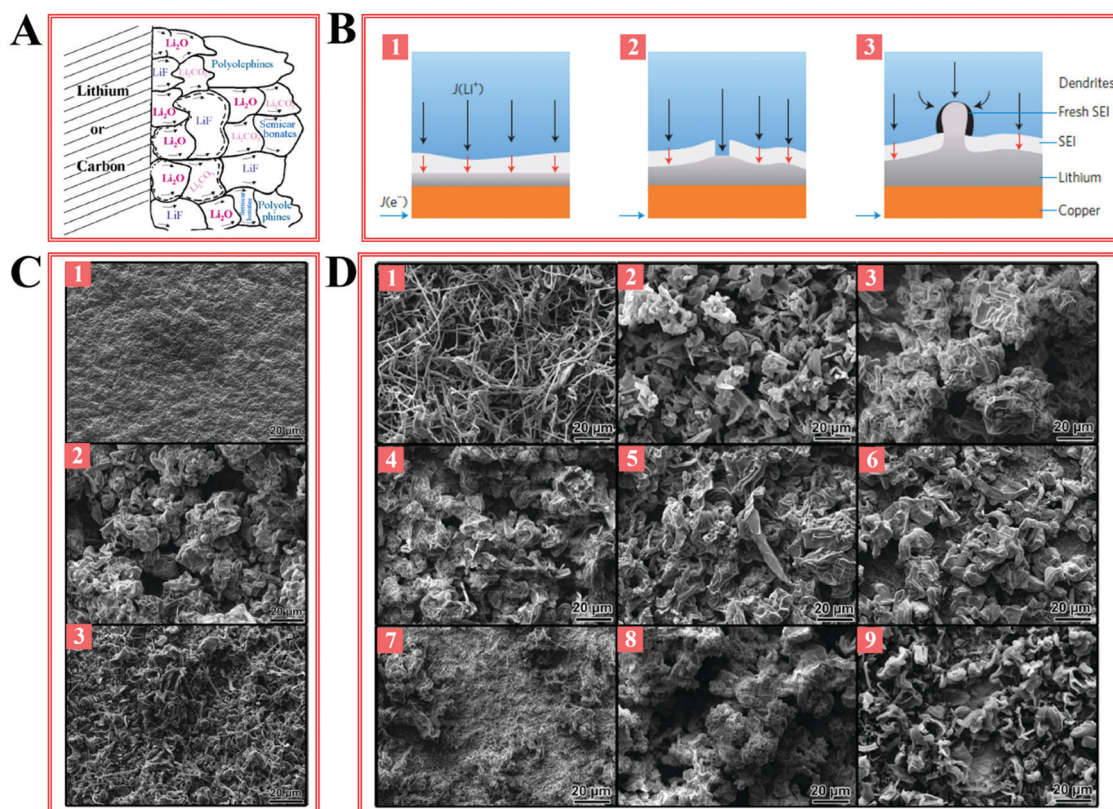


**Fig. 11** Influence of solid–electrolyte interphase on Li electrodeposition. (A) Illustration showing the composition and structure of SEI. Reprinted with permission from ref. 129. Copyright (2017) IOP Publishing. (B) Influence of SEI heterogeneity on Li electrodeposition morphology. Reprinted with permission from ref. 134. Copyright (2014) Springer Nature. (C) Influence of organic solvent. Li deposition morphology in 1 M LiPF<sub>6</sub> in (1) VC, (2) FEC and (3) VEC. Reprinted with permission from ref. 142. Copyright (2013) IOP Publishing. (D) Influence of salt. Li deposition morphology in PC + (1) LiBOB, (2) LiPF<sub>6</sub>, (3) LiAsF<sub>6</sub>, (4) LiTFSI, (5) LiI, (6) LiDFOB, (7) LiBF<sub>4</sub>, (8) LiCF<sub>3</sub>SO<sub>3</sub> and (9) LiClO<sub>4</sub>. Reprinted with permission from ref. 142. Copyright (2013) IOP Publishing.

regular, compact Li electrodeposition emerges as the central challenge in developing practical Li metal batteries.

We first consider efforts to understand and control the native Li surface. Even before exposure to an electrolyte, the as-received Li foils are expectedly covered with native surface films.<sup>132</sup> The native surface film is formed *via* the reaction between Li metal and gas components in the environment, *e.g.* O<sub>2</sub>, H<sub>2</sub>O, CO<sub>2</sub>. The native surface film thus mainly consists of Li<sub>2</sub>CO<sub>3</sub>, LiOH, Li<sub>2</sub>O. Environmental TEM was employed to study the reaction of Li with O<sub>2</sub>, N<sub>2</sub> and H<sub>2</sub>O.<sup>135</sup> In dry N<sub>2</sub> and O<sub>2</sub> (99.9999 vol%), the authors observed the formation of stable, uniform interphase, whereas the presence of trace amount of water vapor is disruptive—the interphase is corroded, becoming nonuniform and porous. The original inorganic components with uneven distribution is able to cause the nonuniform, mossy growth of Li.<sup>130,131</sup> Shiraishi *et al.* reported the unfavorable native surface film can be modified by immersion of the Li foil in a  $1 \times 10^{-3}$  mol L<sup>-1</sup> HF-propylene carbonate solution.<sup>132</sup> The HF modification can turn the surface species into LiF that has a smaller volume per mole, resulting in a thinner surface film. The authors report that spherical Li deposits are observed on HF-modified Li foil, and the HF-modified Li yields a higher plating/stripping efficiency in Li||Li symmetric cell studies.

The SEI formed on the Li electrode inside a battery is then a combination of chemistries native to the Li foil, products of chemical reactions between Li and electrolyte components, and the most stable products of the electrochemical reduction reactions electrolyte components in the battery cell undergo

at the working potential of the Li anode. Since the publication of the SEI model in 1979 by Peled,<sup>128</sup> a large volume of effort has been given to elucidating its composition. Aurbach's review provides a comprehensive introduction to this earlier literature.<sup>133</sup> Among more modern studies, we draw specific attention to very recent works that take advantage of advances in electron microscopy to carry out spatially resolved electron spectroscopy in tandem with morphological analysis to characterize the interphases formed on Li in conditions designed to replicate the native environment inside a battery cell.<sup>59,62</sup> Zachman *et al.* developed a cryo-FIB/STEM method that allows the morphological and chemical constituents of the SEI on Li anodes cycled in a 1 M LiPF<sub>6</sub>-EC/DMC electrolyte to be studied in detail.<sup>136</sup> An important aspect of the study is that the authors employ a plunge-freezing protocol that allows the SEI to be preserved in its native solvent environment and which avoids damage to more fragile constituents of the interphase in the typical electrode removal and solvent washing steps used in EM analysis of the Li electrode. The authors reported that Li electrodeposited in two distinct non-planar morphologies, which they termed type I and type II dendrites, in comparable proportions. The SEI formed on Li is different for the two morphologies and sensitive to the electrolyte composition. The type I dendrites exhibited relatively low curvature, while type II dendrites are highly tortuous and extend to distances many micro-meters in length. Chemical analysis using EELS revealed that the type I dendrites are surrounded by a SEI that extends to distances of (300–500) nm, *i.e.* much, much larger than previously thought, and contains gas bubbles. In comparison to

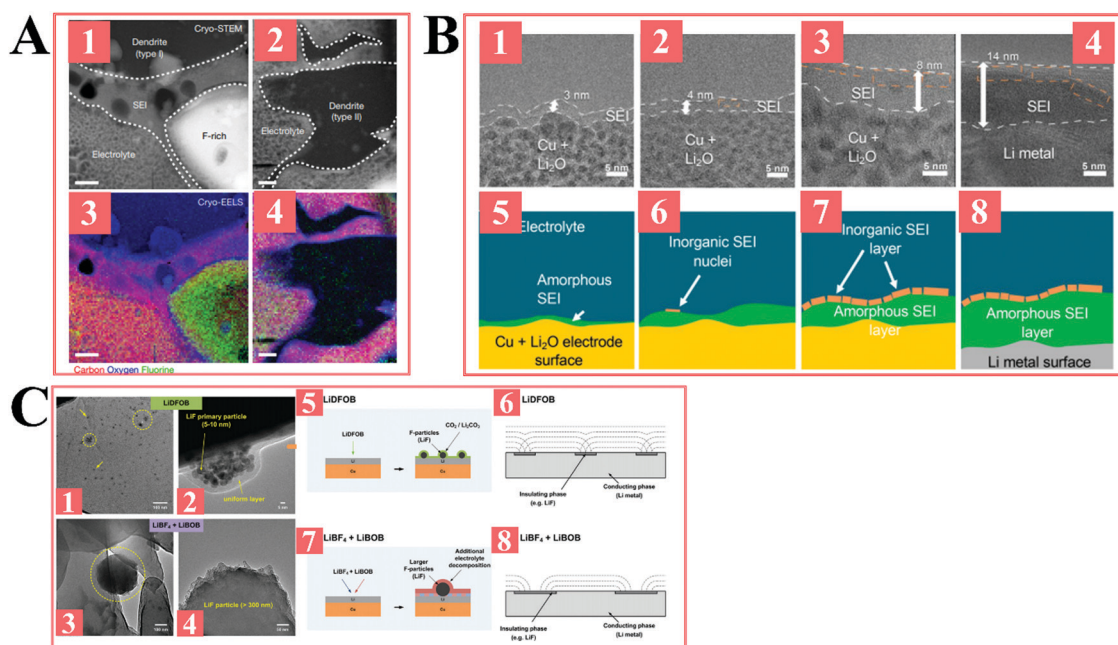


**Fig. 12** Structure and composition of solid–electrolyte interphase revealed by advanced cryo-electron microscopy. (A) Cryo-HAADF, EELS-STEM mapping of the Li dendrites in 1 M LiPF<sub>6</sub> EC/DMC. Reprinted with permission from ref. 136. Copyright (2018) Springer Nature. (B) Cryo-TEM study of the lithiation of CuO wires. Reprinted with permission from ref. 138. Copyright (2019) American Chemical Society. (C) TEM characterization of the SEI formed in 1.2 M LiDFOB in EC-DMC and in 0.6 M LiBF<sub>4</sub> + 0.6 M LiBOB in EC/DMC. Reprinted with permission from ref. 141. Copyright (2018) The Royal Society of Chemistry.

the electrolyte bulk, the type I SEI also exhibited an increased concentration of oxygen and lithium (Fig. 12A-1 and A-3), and was abutted by large ( $\mu\text{m}$  scale) nearly spherical structures containing oxygen, carbon, and lithium, as well as elevated levels of fluorine. In contrast, the SEI on the type II dendrite is thin ( $\sim 20$  nm), and enriched in Li and O, relative to the electrolyte bulk (Fig. 12A-2 and A-4). EELS analysis of the interior of the type I and II dendrites indicate that whereas the type I material is primarily metallic lithium, the type II dendrites are essentially pure LiH with small fragments of metallic Li near their tips, suggesting formation by an extrusion/root-growth process. Replacing the electrolyte with a 2 M  $\text{LiPF}_6$ -fluoroethylene carbonate (FEC, see molecular structure in Table 2) fully fluorinated electrolyte, the type I dendrites predominated. Li *et al.* also used a cryo-STEM approach to characterize the SEI formed on Li deposited directly onto a Cu TEM grid in a 1 M  $\text{LiPF}_6$ -EC-diethylcarbonate (DEC) electrolyte.<sup>65</sup> Prior to cryo-STEM analysis, the Li deposits were washed with 1,3-dioxalane in a procedure designed to remove the electrolyte salt. The authors reported that a mosaic SEI approximately 20 nm thick and composed of an amorphous

organic material with small ( $\sim 3$  nm) domains of crystalline lithium oxide and lithium carbonate forms on the Li deposits. Upon addition of FEC (10 volume%) to the electrolyte, the authors observed a complete transformation of the SEI to a layered structure composed of an inner amorphous polymer film on the Li deposit and an outer crystalline lithium oxide layer, but no evidence of LiF salt commonly thought to be a key side product of FEC polymerization.<sup>137</sup> Rapid local Li dissolution is observed beneath crystalline regions in mosaic SEI; while uniform, radial dissolution of Li is observed under multi-layered SEI.

In a related work, Huang *et al.* used cryo-TEM to investigate the SEI evolution during the lithiation on CuO nanowire<sup>138</sup> since the Cu foil used in Li||Cu half cells are covered with an oxidation layer. At a potential around 1.0 V vs.  $\text{Li}^+/\text{Li}$ , CuO is transformed to  $\text{Cu}/\text{Li}_2\text{O}$  via a conversion reaction. Fig. 12B describes the morphological evolution under TEM from 1.0 V (B-1, 5), 0.5 V (B-2, 6), 0.0 V (B-3, 7) to below 0 V (B-4, 8). Initially, the SEI is thin (3 nm), amorphous and carbon-, oxygen-enriched. As the potential decreases, the SEI thickens to 14 nm, with an inorganic layer ( $\sim 4$  nm) containing small crystallites covering the outer surface. The results show that the SEI grows throughout the whole lithiation process. The growth of the amorphous layer can proceed under the inorganic layer. This contradicts the common wisdom that SEI growth is suppressed once the substrate surface is passivated. A similar study by Hou *et al.*,<sup>139</sup> observed continuous growth of both the inorganic and the organic layers simultaneously. They attribute the continuous growth to the diffusion of radical species from electrode surface to the SEI-electrolyte interface, as previously suggested by first-principles calculations.<sup>140</sup>

To understand the role played by the electrolyte salt in setting the SEI chemistry, Jung *et al.* investigated the effect of salt on Li deposition morphology using *ex situ* TEM (Fig. 12C).<sup>141</sup> The authors found that the SEI forms in  $\text{LiDFOB-EC/EMC}$  consists of uniformly distributed nanostructured LiF particles (5–10 nm). In contrast, in an  $\text{LiBF}_4 + \text{LiBOB-EC/DMC}$  electrolyte, the SEI contains coarse LiF particles as large as 300 nm, while no LiF is observed in  $\text{LiPF}_6$ . Authors observed significantly higher Li reversibility in the former electrolyte ( $>95\%$  vs.  $\sim 60\%$ ), suggesting that the small, uniform LiF structures in the SEI are beneficial. The authors contend that, LiF can be considered as an inactive area for Li plating, due to its electrical insulating nature and relatively low  $\text{Li}^+$  diffusivity compared with other SEI components. An analogous, but more comprehensive study by Ding *et al.*<sup>142</sup> shed light on the effect of the electrolyte solvent (Fig. 11C) and salt (Fig. 11D) on SEI composition and on Li deposition morphology. Cyclic carbonates, *e.g.* VC, FEC, and VEC were observed to have beneficial effects on the formation of uniform SEI due to the possible polymerization reaction at the Li anode. Surprisingly, the authors report that Li electrodeposits in the most polymerization-prone of the electrolytes (VC) is completely uniform and non-dendritic (Fig. 11C-1). The authors ascribed their observation to the a SEI composed of a VC-derived surface film that possibly consist of polymeric/oligomeric species.<sup>143</sup> XPS analysis shows that the SEI formed on Li in the VC

Table 2 Abbreviations of the molecules used in the electrolyte for Li metal anode

EC	
DMC	
DEC	
FEC	
VC	
PC	
DME	$\text{CH}_3\text{OCH}_3$
DOL	
LiDFOB	$\text{LiBF}_2(\text{C}_2\text{O}_4)$
LiBOB	$\text{LiB}(\text{C}_2\text{O}_4)_2$
LiTFSI	
LiFSI	
LiBETI	

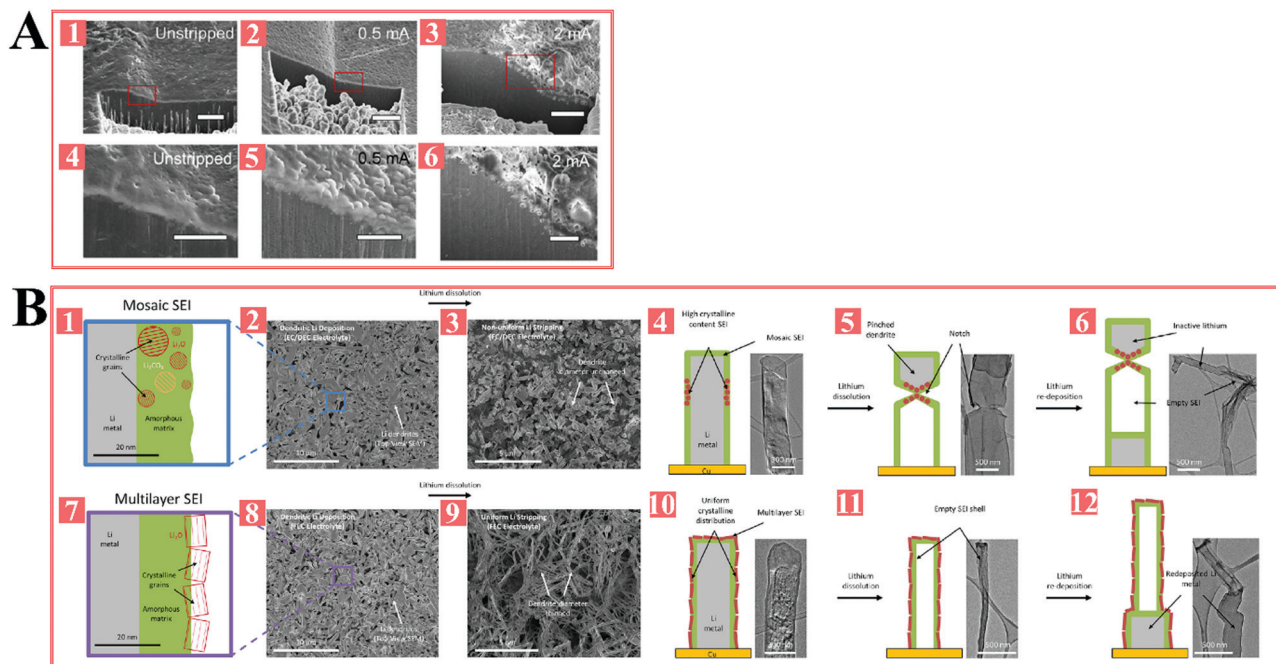


Fig. 13 Stripping process of Li revealed by advanced electron microscopy. (A) SEM study of the stripping process of Li electrodeposits. Reprinted with permission from ref. 145. Copyright (2018) National Academy of Sciences. (B) Cryogenic electron microscopy study of Li stripping in 1 M LiPF<sub>6</sub> w/and/o FEC additive. Reprinted with permission from ref. 146. Copyright (2018) Elsevier.

electrolyte has an increased C–O band intensity, consistent with the formation of polymeric species. Ota *et al.* carried out gel permeation chromatography to characterize the molecular weight of the SEI.<sup>143</sup> They found that the weight average molecular weight  $M_w$  of electrolytes containing 50% EC/50% DMC, 49% EC/40% DMC/2% VC and 100% VC are, respectively, 1900 g mol<sup>-1</sup>, 2400 g mol<sup>-1</sup> and 6700 g mol<sup>-1</sup>, confirming the presence of more VC leads to higher molecular weight polymers. In a FEC electrolyte (Fig. 11C-2), the Li deposits basically show similar features to those from cyclic EC, PC. The Li deposits in VEC however show need-like dendritic morphology. Ding *et al.* also visualized Li electrodeposits from PC containing different Li salts to study the effect of salts on SEI and on deposition morphology (Fig. 11D).<sup>142</sup> The morphology obtained with LiBOB is highly fibrous, while the others are mainly mossy. XPS results show that Li<sub>2</sub>CO<sub>3</sub> is the prominent inorganic species in the SEI of LiBOB, LiDFOB, LiAsF<sub>6</sub>, and LiCF<sub>3</sub>SO<sub>3</sub>, while considerable amount of Li<sub>2</sub>O is found in the SEI of LiClO<sub>4</sub> and Li<sub>2</sub>O. For LiPF<sub>6</sub>, LiBF<sub>4</sub> and LiTFSI salts, LiF is the main component of the SEI.

The topography of the SEI is also of interest since parasitic reactions occur on the interface between Li and the electrolyte. A smaller surface area indicates slower parasitic chemical reaction rate. Lee *et al.* examined the topography of Li metal deposits by cryo-FIB.<sup>144</sup> Based on the SEM of the cross section, they reconstructed the distribution of Li metal and voids in 3D space. Interestingly, they found that concentrated ether-based electrolytes can render smaller Li-electrolyte interface area. It implies that the parasitic surface reactions can be suppressed, owing to the small interface area. The SEI has been shown to

have a strong influence on the stripping morphology of Li. Shi *et al.* studied the morphological change of SEI during Li stripping.<sup>145</sup> They performed SEM observation of the fresh cross section of Li cut by FIB. The results show that, nano-voids are generated at the Li–SEI interface upon stripping (Fig. 13A). The fast generation and accumulation of the voids at high current densities can lead to crack formation in the SEI layer that initiates pitting. In a study by Li *et al.*, two types of SEI, *i.e.* multilayered in FEC containing electrolyte and mosaic in baseline electrolyte, are identified and are shown able to generate different Li stripping morphology, respectively, as revealed by TEM (Fig. 13B).<sup>146</sup> Rapid local Li dissolution is observed beneath crystalline regions in mosaic SEI; while uniform, radial dissolution of Li is observed under multilayered SEI.

A conclusion from all of these studies is that the SEI formed in fluorinated electrolytes are fundamentally different in their ability to facilitate more uniform Li deposition and to improve reversibility of the Li anode. Lu *et al.* showed that addition of LiF salt to aprotic carbonate liquid electrolytes reduced the interfacial impedance, produced more uniform electrodeposition Li,<sup>147,148</sup> and improved anode reversibility in Li plate-strip cycling experiments.<sup>149</sup> Both behaviors have been rationalized using Joint Density Functional calculations, which show that the energy barrier for Li adatom transport on a crystalline LiF interphase is substantially lower than one composed of lithium carbonate or lithium oxides found in the SEI on Li formed in typical carbonates.<sup>124,125</sup> The important role FEC plays in enabling finer control of Li electrodeposition and higher reversibility of electrodeposits formed in carbonate media may also be rationalized

in this context as a easily-reduced carrier for LiF and polymerizable VC.<sup>142,150</sup> We note, however, that the use of FEC as an electrolyte additive predates its current popularity in electrochemical cells based on Li metal anodes.<sup>151,152</sup> Specifically, FEC was initially employed as an additive in Li-ion batteries, and showed beneficial effects on the SEI formed on the anode, *e.g.* graphite,<sup>153</sup> Si.<sup>154</sup>

Brown *et al.* used TEM to characterize the Li deposits from electrolytes with different FEC contents (0%, 10% and 100%).<sup>155</sup> They found that the SEI formed in the 100% FEC electrolyte is nanostructured LiF with a smooth coating of Li<sub>2</sub>CO<sub>3</sub>. Simulations of the density of states and of the electrostatic potential show that the LiF–Li interface has a higher energy barrier for electron tunneling into the SEI.<sup>156</sup> This means that Li electrodeposition can only occur at the Li surface, suppressing the direct reduction of Li in the SEI *via* electron tunneling effect. The presence of Li<sub>2</sub>CO<sub>3</sub> in the SEI reportedly can reduce interfacial resistance.<sup>157</sup> In contrast, the SEI formed in EC/DMC with 0% FEC is oxygen enriched, and no fluorine peak is observed in EDS. A similar beneficial effect of FEC is reported for Na metal electrodeposition. Rodriguez *et al.* studied Na deposition in electrolyte with or without FEC component.<sup>158</sup> They performed time of flight secondary ion-mass spectroscopy to probe the composition of SEI. The results show that the SEI in FEC-containing electrolyte has a higher NaF content and a lower PO<sup>−</sup> content. This implies that the presence of NaF can prevent the continuous reduction of PF<sub>6</sub><sup>−</sup> anion on Na surface.

The Li<sup>+</sup> flux towards the electrode is directly limited by Li<sup>+</sup> transport across the SEI. Once formed, the Li<sup>+</sup> ion transport properties and mechanics of the SEI are therefore important determinants of its effectiveness in regulating Li electrodeposition. Lu *et al.* used time-of-flight secondary ion mass spectroscopy to quantify the Li<sup>+</sup> cation and the BF<sub>4</sub><sup>−</sup> anion transport within the SEI formed in 1 M LiClO<sub>4</sub>–EC/DEC electrolyte.<sup>159</sup> They found that there is a porous structure of a thickness around 5 nm on the outer layer of SEI. Beneath the porous layer is a dense layer mainly composed of Li<sub>2</sub>O and Li<sub>2</sub>CO<sub>3</sub>. The presence of BF<sub>4</sub><sup>−</sup> anion is limited to the porous layer, meaning that the dense layer poorly conducts BF<sub>4</sub><sup>−</sup>. In contrast, <sup>6</sup>Li<sup>+</sup> tracer was detected in the dense layer, implying that the dense layer conducts Li<sup>+</sup> possible *via* interstitials or vacancies. Maraschky *et al.* developed a model to explain the onset of dendritic Li growth from a perspective of Li<sup>+</sup> transport across the SEI (Fig. 14).<sup>160</sup> They defined  $\tau_{\text{onset}}$  as the point at which dendritic

growth occurs. When  $t < \tau_{\text{onset}}$ , the thickness of SEI increases, which leading to an increasingly serious Li<sup>+</sup> depletion. When  $t = \tau_{\text{onset}}$ , the thickness of SEI reaches  $nFD_{\text{SEI}}SC_0i^{-1}$ , and the concentration of Li<sup>+</sup> at the Li–SEI interface drops to zero. Afterwards ( $t > \tau_{\text{onset}}$ ), the interface is fundamentally unstable. Li dendrites preferentially grow from the sites where the SEI is thin or ruptured. This prediction is consistent with the experimental results reported by Chen *et al.*<sup>161</sup> Li deposition morphologies in a series of DOL/DME-based electrolytes with different LiNO<sub>3</sub>:LiTFSI salt molar ratios were evaluated (0:10, 2:8, 4:6, 6:4 and 8:2). The Li deposits gradually change from a wire-like morphology to a more spherical shape. This evolution in growth morphology is consistent with expectations for the increasing Li<sup>+</sup> diffusivity in the SEI achieved by varying the electrolyte salt composition.

The presence of some unexpected species in the SEI can induce Li dendritic growth. Soft X-ray spectroscopy results show that the dissolved species from the cathode, *e.g.* Mn<sup>2+</sup>, is present in the anode SEI.<sup>162,163</sup> The Mn<sup>2+</sup> presumably can be reduced into electron conducting Mn<sup>0</sup> particles embedded in the SEI. The presence of the electron conducting Mn<sup>0</sup> particles promotes the disruption of SEI and the dendritic Li growth into the SEI. There are also reports claiming that SEI is not necessary for the wire-like growth of Li. Steiger *et al.* studied the morphologies of Li deposited *via* physical vapor deposition method and liquid electrochemical deposition method, respectively.<sup>164</sup> According to SEM characterization, the authors claim that the PVD Li and the electrodeposited Li have strong resemblance in morphology, and that this resemblance indicates the underlying mechanisms dominating Li deposition morphologies in the two methods could be the same. The wire-like growth of other metals including Cu and Si during PVD is also reported in the literature, where the phenomenon interpreted as a result of surface dewetting of electrodeposits.<sup>165</sup> On this basis, the authors further attributed the needle growth of Li to the presence of defect sites on the surface. The highly mobile Li atoms diffuse towards and accumulate around defects in the form of needles. The authors suggest strategies that enhance the crystallinity of Li be implemented to prevent the surface diffusion. In addition to needle-like Li, it is shown that “bush” growth is only present in electrochemical deposition, implying that it is a phenomenon controlled by SEI. We however notice that as revealed in a study by Gireaud *et al.*, pulsed laser deposited Li on stainless steel exhibits a granular and

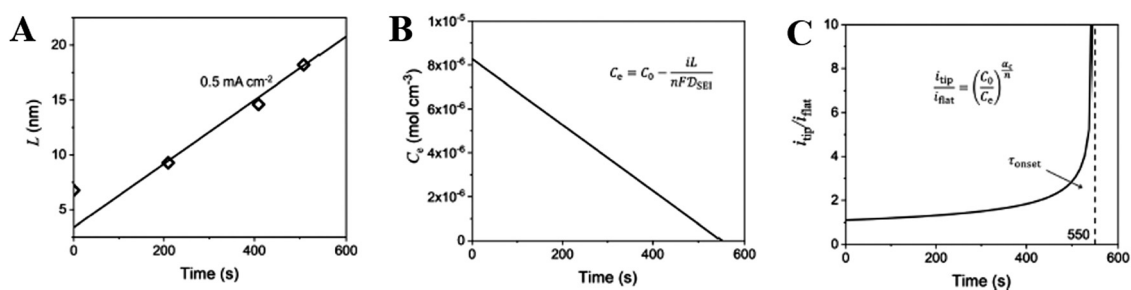


Fig. 14 Model prediction of Li dendrite initiation due to mass transport limit in SEI. (A) the thickness of SEI *versus* time. (B) The concentration of Li<sup>+</sup> at the Li surface *versus* time. (C) The relative magnitude of current densities on dendrite tip and on flat electrode. Reprinted with permission from ref. 160. Copyright (2018) IOP Publishing.

relatively homogeneous morphology, and no whiskers or needle-like deposits are observed.<sup>166</sup> This suggests the wire-like Li morphology obtained *via* PVD mentioned by Steiger *et al.* does not sufficiently prove the wire-like Li morphology in liquid electrolyte is independent of SEI.<sup>164</sup>

It is clear that the cryo-electron microscopy has made possible a more comprehensive understanding of the composition and structure of the SEI with atomic scale resolution. Many aspects of the new findings, including the composition of the inorganic and organic species and their relative position with respect to the electrode are of course not entirely unexpected based on knowledge of reduction potentials of the components used in the various electrolytes, fast decay of the electric field produced by any charged surface in a salty liquid electrolyte, and thermodynamic stabilities of the products of the electrode reduction reactions.<sup>167</sup> However the factors responsible for the apparent compartmentalization of the respective products and for the scale of the compartments, including the large size of the SEI are to date largely unknown. The study by Zachman *et al.*,<sup>136</sup> for example, reveals large void spaces in the SEI which the authors tentatively attribute to ethylene gas produced by reduction of ethylene carbonate. Huang *et al.*<sup>168</sup> recently combined cryo-STEM and Differential Electrochemical Mass Spectrometry (DEMS) to interrogate the SEI and gas composition in the head space of a composite carbon-black anode designed to mimic the electrode in a lithium ion battery. These authors reported that substantial amounts of ethylene gas is produced during cycling of the carbon anode and that an originally thin SEI can grow to hundreds of nanometers during cycling. It is possible that the expansion and movement of lower-density gas pockets created at the negative electrode is responsible for pushing material away from the metal electrolyte interface and for providing the driving force for compartmentalization. It is also known that once polymerization of electrolyte components is initiated, particularly by anionic centers, the reaction can propagate over distances that are set by a competition between the timescale for active center diffusion and termination.<sup>169</sup> To the extent that the compartments in a mosaic or layering model are formed by electrode reduction products held together by an *in situ* formed organic polymer, it is possible to achieve essentially any SEI thickness—limited only by the inter-electrode spacing. As a final note, we reference the recent operando optical visualization studies of Deng *et al.*,<sup>48</sup> particularly the supporting videos, which show how aggressively orphaned fragments of dendritic sodium electrodes migrate to fill the inter-electrode space to highlight that there are other mechanisms available in a battery that may aid mass transport over large distances. In addition to providing answers to these fundamental questions, new studies able to answer any of the following questions are considered crucial for progress: (i) does Li deposit beneath the SEI formed in the previous plating/stripping cycle? This question is important because if in each cycle, a certain amount of Li needs to be irreversibly lost owing to the SEI forming reactions, there then exists a fundamental limit on the reversibility of Li. Furthermore, the accumulation of the SEI “shell” after Li stripping can form a thick inactive layer and block the mass

transport pathway. Considering that SEI is formed on the individual Li wires, it is less probable that new Li can grow along the SEI “shell”. (ii) Does Li<sup>+</sup> transport across the SEI in plating/stripping, or does Li preferentially grows/dissolves along the crack sites? In the former case, the transport parameters of the SEI emerge as crucial aspect in understanding Li deposition morphology. The measurements of transport parameters of SEI still remain inconclusive, in part due to the heterogeneous, complicated nature of the SEI. In the latter case (*i.e.* Li preferentially grows at crack sites), the mechanical properties of SEI act as the determining factor in deposition morphology. (iii) How do ions transport across and within the SEI? On the one hand, the high cation diffusion energy in the inorganic crystals (*e.g.* 0.7–2.0 eV for LiF) suggests that the ion transport through a bulk inorganic crystal is very slow ( $10^{-7}$ – $10^{-13}$  S cm<sup>-1</sup>).<sup>170</sup> On the other, we’ve already pointed to JDFT analysis and experiments that conclusively show that surface diffusion barriers for Li adatoms are lower on LiF than on other inorganic components reported thus far in the SEI. (iv) What is the desirable SEI composition and structure? The preponderance of recent studies indicate that fluorinated electrolyte components lead to SEI that are enriched in LiF and fluorinated organic species that enable finer control of electrodeposition morphology and reversibility. However, contrary to the idealistic substrates modeled with the JDFT analysis,<sup>125</sup> the LiF component is typically distributed in localized pockets in the SEI and is always accompanied by lithium oxide and carbonates, meaning that the large enhancements in mobility anticipated from theory may only be possible in interphases that are precisely fabricated using processes such as magnetron sputtering.<sup>148</sup> Nonetheless, we note that JDFT as well as a limited set of published results,<sup>171</sup> indicate that brominated analogs of popular fluorinated electrolyte additives could be superior components in an SEI. Careful studies analogous to those for fluorinated electrolyte additives would not only provide a more rigorous assessment of these findings but will also add to the chemistry toolbox for designing SEI for the Li metal anode.

#### 2.4 Influence of external factors

A rarely discussed but differentiating aspect of rechargeable batteries is that they are closed electrochemical reactors. This means that with the exception of the electrode formation step, exchange of matter created inside a battery with the surroundings or *vice versa* is unavailable as a tool to remove undesired species formed in the cell or to introduce required components (*e.g.* the Li metal anode or fluorinated electrolyte additives) that may be exhausted over the hundreds or thousands of cycles of operation. While the concept of batteries with refreshable anodes has been explored,<sup>172</sup> battery designs that allow the Li metal anode or other cell components to be easily refreshed are to our knowledge unexplored. Temperature, mechanical stress, magnetic torques, and gravitational forces are on the other hand well known in other engineering contexts for their ability to transport energy and momentum across physical boundaries—in both directions. In this section we review the existing literature

with the aim of identifying underlying principles that could be leveraged to achieve fine control of electrodeposition processes at the Li metal anode.

Early reports show that temperature can have a profound effect on electrodeposition of metals. For example, at elevated temperature Zn has been reported to form larger electrodeposits<sup>173</sup> and the brightness/reflectivity of Sn electrodeposited films has been reported to increase with temperature.<sup>174</sup> In theory, Li<sup>+</sup> transport in a bulk electrolyte and at interphases would be enhanced as temperature increases, but these potential benefits must be balanced against the faster kinetics of parasitic reactions in the closed cell, forming a thicker SEI and consuming active components in the closed cell. It is then unsurprising that literature reports reveal that thermal influences on lithium metal anode uniformity are multifaceted and complex.

Ishikawa *et al.* studied the electrochemical performance of Li metal anodes at sub-ambient temperatures (−20, −10, 0 °C) conditions in carbonate electrolytes.<sup>6,175,176</sup> The main observation is that a low-temperature precycling condition can enhance the Li cyclability in the subsequent cycles at room temperature. The authors suggested that compact SEI formed at low temperature remains stable during the cycling. Park *et al.* investigated the resistance and sand's time at low temperatures.<sup>177</sup> The internal resistance is negatively correlated to temperature, while the sand's time is increases as the temperature decreases. As concluded by the authors, the high resistance at low temperature retards the dendrite growth. Love *et al.* used *in situ* optical microscopy to the growth of Li dendrites at −10, 5 and 20 °C.<sup>178</sup> As shown in Fig. 15A-1, the Li deposition morphology is temperature dependent—the low temperature of −20 °C favors mushroom-like morphology, while Li deposits are needle like at 5 and 20 °C. Li shows a higher propensity for battery short at sub-ambient temperatures.<sup>179</sup> The short-circuit time is the shortest at 5 °C, and longest at 20 °C. An empirical equation is given to describe the relation between temperature and short circuit time.

$$t_{sc} = t_i f(T) + \frac{l}{v_d f(i, T, \text{morphology})} + \text{morphology} f(T), \text{ where}$$

$t_{sc}$  is short-circuit time,  $t_i$  is dendrite initiation time,  $v_d$  is the dendrite growth rate,  $l$  is the interelectrode distance,  $i$  is the applied current. Love further discussed the interaction between Li dendrites and polymer separators at low temperatures. The polymer separator becomes brittle below the glass transition temperature, as evidence by the disappearance of the plastic deformation regime. Owing to the different Li deposition morphologies and separator properties at different temperatures, three types of interactions are identified, *i.e.* brittle fracture, puncture and mixed penetration of separator (Fig. 15A-2).<sup>180</sup>

Mogi *et al.* used *in situ* AFM to probe the Li deposition on a nickel substrate at elevated temperatures in propylene carbonate.<sup>181,182</sup> The Li plating/stripping coulombic efficiency is higher than that at room temperature. The AFM observation shows that the surface film of Li deposition at 80 °C is smoother. The authors examined the role of this smooth surface film by performing a Li deposition/dissolution cycle at 80 °C, followed by subsequent Li deposition at room temperature.

The Li surface morphology turns out to be rough. The authors hypothesized that the self-reparability of the surface film at elevated temperature should be accounted for. It is also pointed out the faster surface diffusion rate of Li atoms at elevated temperature is one plausible reason.

Recent studies investigated the temperature-dependent Li nucleation and growth behaviors.<sup>183–185</sup> They showed that at elevated temperatures, *e.g.* 60 °C, Li exhibits larger nucleation size and lower number density, leading to a more compact morphology (Fig. 15B). The main interpretation of this temperature dependence is that mass transport is significantly faster at elevated temperatures. In the liquid phase, Li<sup>+</sup> ion diffusivities are strongly dependent on temperature:<sup>183,186</sup>  $1.05 \times 10^{-5}$  @ 60 °C,  $3.40 \times 10^{-6}$  @ 20 °C and  $6.1 \times 10^{-7}$  @ −20 °C. Likewise, the Li-ion transport through the SEI is also facilitated as suggested by  $R_{ct}$  measured by EIS. XPS analysis reveals that formation of LiF on Li surface is facilitated, which stabilizes the Li metal surface and provides a fast Li<sup>+</sup> ion transport across the SEI. In contrast, the temperature dependence is much less obvious in a carbonate electrolyte, which still lacks an interpretation. Annealing is also common phenomenon observed in many materials at elevated temperatures, during which unnecessary microstructures can be smoothed out forming a flatter surface. Aryanfar *et al.* performed coarse-grain – Monte Carlo simulations of annealing processes for Li dendrites.<sup>187</sup> The surface diffusion and the bulk diffusion activation energy barriers are 10.1 kcal mol<sup>−1</sup> and 2.5 kcal mol<sup>−1</sup>, respectively. Due to the small difference between the two, it is highly plausible that both mechanisms occur simultaneously. The Li deposition morphology was evaluated using normalized dendrite length  $\bar{\lambda}(T, t) = \frac{1}{L} \sum_{i=1}^n \lambda_i p_i$ ,

where  $L$  is the interelectrode distance. The simulation predicts that heating enhances bulk and surface diffusion of Li and annealing at 55 °C reduces representative dendrite length by 36%. In particular, the mobility of Li atoms may play an important role above the onset temperature of surface reconstruction  $T_{SR} = 294$  K.<sup>188</sup> It is consistent with a report by Li *et al.*,<sup>116</sup> where the authors describe the healing behavior of Li dendrites induced by local self-heating in Li metal cells cycled at 9 mA cm<sup>−2</sup>.<sup>189</sup>

The composition and structure of SEI is shown to be dependent on temperature. Wang *et al.* observed similar behaviors for Li metal anodes at elevated temperature.<sup>190</sup> Cryo-TEM was utilized to further reveal the origin of the improvement in Li reversibility (97.6% for 300 cycles, 97.4% for 75 cycles, 96.1% for 30 cycles and 65.4% for 2 cycles at 60, 20, 0 and −20 °C, respectively). As shown in Fig. 15C, the authors observed distinct SEI at 60 °C—it is thicker (35 nm *vs.* 20 nm at 20 °C) and has a crystalline Li<sub>2</sub>O layer which is absent in the SEI formed at 20 °C. It is hypothesized that the greater thickness and the existence of crystalline Li<sub>2</sub>O can stabilize the SEI layer that effectively passivates the Li metal. Another cryo-TEM study by Thenuwara *et al.* showed the SEI is thinner at subambient temperature, *i.e.* −40 °C, and is mainly composed of nanoscale LiF (<10 nm), as opposed to the Li<sub>2</sub>O and Li<sub>2</sub>CO<sub>3</sub> observed in the SEI formed at room temperature. However, extremely low plating/stripping CE around was observed at −40 °C.

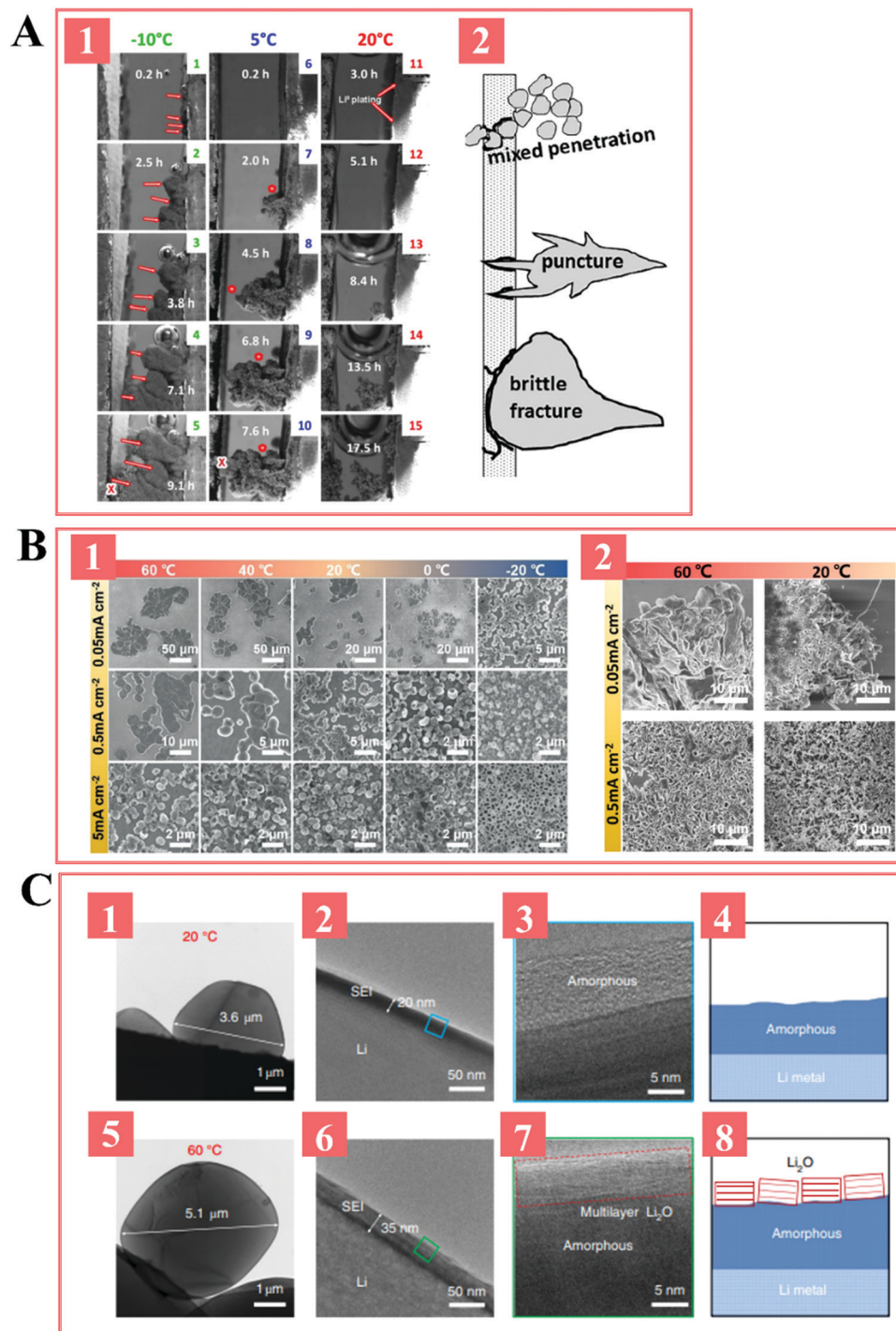


**Fig. 15** Influence of temperature on Li electrodeposition. (A) Li deposition at sub-ambient temperatures. Reprinted with permission from ref. 178 and 180. Copyright (2015) IOP Publishing. Copyright (2016) American Society of Mechanical Engineers. (B) Li deposition at elevated temperatures. Reprinted with permission from ref. 183. Copyright (2019) John Wiley and Sons. (C) Cryo-TEM characterization of the SEI formed at elevated temperature. Reprinted with permission from ref. 190. Copyright (2019) Springer Nature.

Literature reports showing that the cycle life of lithium metal cells is improved at elevated temperature are encouraging because they allay obvious concerns about offsetting contributions from faster parasitic reaction kinetics. We note nonetheless that although the cycle lifetime is reported to be significantly prolonged at elevated temperature, the increase in Li plating

stripping coulombic efficiency is not significant, in spite of the flattening of Li deposition morphology. As noted in the introduction section of the review, a near unity coulombic efficiency is a requirement for stable cycling of the lithium metal anode in cells with low N:P. We believe this paradoxical result requires more fundamental studies (*e.g.* using DEMS and cryo-STEM interrogation) of

kinetics of degradation reactions and further experimentation in Li cells with more limited amounts of Li (*i.e.* lower N:P) to understand the sources of irreversible Li capacity at elevated temperatures?<sup>184</sup> In addition, due to the low melting point of Li and presence of significant compressive mechanical forces introduced during cell assembly, the Li deposits can undergo creep deformations and flow at elevated temperatures,<sup>191</sup> as will be discussed in the next section. Since the Li electrodeposition for SEM characterization was performed in coin cell whose internal pressure is large, is the flattening behavior mainly due to the mechanical deformation?

Stress and strain associated with internal volume change or external forces are another key set of factors that must be understood to facilitate fine control of electrodeposition processes.<sup>192,193</sup> The detrimental effects of stress on intercalation electrodes generated during battery cycling are well received: (1) electrode materials deform and ultimately pulverize. The pulverization damages the electron transport pathway, causing the formation of “orphaned” material and the increase in impedance; (2) stress-induced cracks in SEI continuously expose fresh, unpassivated surface to the electrolyte. The fresh surface reacts with the electrolyte, which results in irreversible material loss and low charge-discharge coulombic efficiency.

The influence of stress and strain on Li electrodeposition are coupled to intrinsic (*e.g.* the volume change during Li plating/stripping) as well as external factors (the effect of mechanical pressure on the kinetics of the metal reduction reaction).<sup>194,195</sup> These effects may be either beneficial or problematic depending on the underlying mechanics of the electrode components. For example, the fatigue deformation created by periodic shrinkage and swelling of the underlying Li anode can cause weaker, mossy deposit fragments to break away from the electrode mass to become electronically isolated—and therefore electrochemically inaccessible. The solid Li fragments created between the anode current collector and the separator/SSE that are originally in direct contact is able to deform and then penetrate the separator/SSE, especially at cavity sites,<sup>196</sup> physically bridging the anode and the cathode, which gives rise to dangerous battery short. In contrast, theoretical analysis<sup>83,194,195,197,198</sup> and a growing body of experiment<sup>199–202</sup> show that electrolyte mechanics may play a role in regulating Li electrodeposition either through control of the electrode kinetics or by driving ion transport away from relatively compressed regions in an electrolyte near dendrites to counter the effect of electric field line concentration which promotes transport to the dendrites. Therefore, it is fundamentally important to understand the mechanical properties of Li metal deposits and to clarify how stress-strain behavior in an electrochemical cell influences Li deposition.

Bulk mechanical properties of Li as a representative BCC metal have been reported extensively in a metallurgical context. Reported values are nonetheless characterized by large variations, *e.g.* elastic modulus values from 1.84 to 7.8 GPa and yield stress values from 0.48 to 1.10 MPa.<sup>203,204</sup> The accurate measurement of Li's mechanical properties is challenging, primarily owing to its propensity for reacting with oxygen, moisture and other components in the open environment.

This means that Li should be handled throughout the sample preparation and the mechanical test within a protective gas, *e.g.* high purity Ar. Some tests reported were not performed under inert gas protection,<sup>205–207</sup> which could yield data that are less genuine. Recently, a few papers report on the mechanical measurements of Li metal bulk mechanical properties carried out in Ar-filled glovebox. Herbert *et al.* performed a systematic investigation based on nanoindentation tests into the mechanical behaviors of vapor deposited polycrystalline Li film, including its elastic modulus<sup>208</sup> and the transition to plastic flow mechanisms.<sup>209,210</sup> The measured elastic moduli are between 9.8 GPa ± 11.9% and 8.2 GPa ± 14.5% for different film thicknesses. From a microscopic point of view, DFT calculations show that BCC Li is unusually soft and can hardly resist plastic deformation mainly through dislocation migration, owing to the small energy barriers.<sup>211</sup>

Creep can occur in Li metal anode operated at room temperature. Li metal has a low melting temperature of 453 K, relative to other metals (Al: 933 K, Mg: 923 K, Zn: 692 K). At room temperature, the homologous temperature of Li  $T_H = 0.66$ . Additionally, the self diffusion activation energy  $Q$  of bulk Li is low (12–13 kcal mol<sup>-1</sup>).<sup>212</sup> In particular, local temperature gradient is expected to enlarge the influence of creep plastic flow. A recent report by LePage *et al.* describes the strain rate dependent properties of Li and its implication for Li plating/stripping.<sup>191</sup> The authors conclude that power-law creep is the dominant deformation mechanism of Li during plating/stripping, following  $\dot{\epsilon} = A\sigma^m \exp\left(\frac{-Q_c}{RT}\right)$ , where  $A$  is a material-specific constant,  $m$  is the power-law creep exponent,  $Q_c$  is the activation energy for dislocation climb.

More broadly, it is known that the mechanical properties of solids are strongly dependent on size and specific morphology induced by deformation, *e.g.* the Hall-Petch relationship,<sup>213</sup> work-hardening,<sup>214</sup> *etc.* The behaviors at small scales or in dendritic/mossy morphology can be very different than those of bulk Li. Xu *et al.* performed uniaxial compression experiment on Li micropillars with diameters ranging from 1.39 μm to 9.45 μm, and an obvious size effect was observed.<sup>203</sup> The yield stress increases from 15 MPa at 9.45 μm to 105 MPa at 1.39 μm (Fig. 16A).

The Li obtained *via* electrodeposition is more complicated in microstructure, which indicates mechanical properties of electrodeposited Li can be different with bulk Li or Li pillar. Wang *et al.* studied the mechanical behavior of electrodeposited mossy Li using flat punch indentation (Fig. 16B).<sup>215</sup> The Young's modulus of mossy Li is 1.6–2.6 GPa, depending on the indentation condition, which is smaller than the bulk modulus (~7.8 GPa) measured by the same method. The much smaller modulus of mossy Li is attributable to its porous nature. Interestingly, the creep depth of mossy Li is much smaller than that of bulk Li and is barely influenced by punch stress. Dislocation starvation and the presence of inorganic species in the SEI are suggested as two possible factors contributing to the enhanced creep resistance of electrodeposited mossy Li.

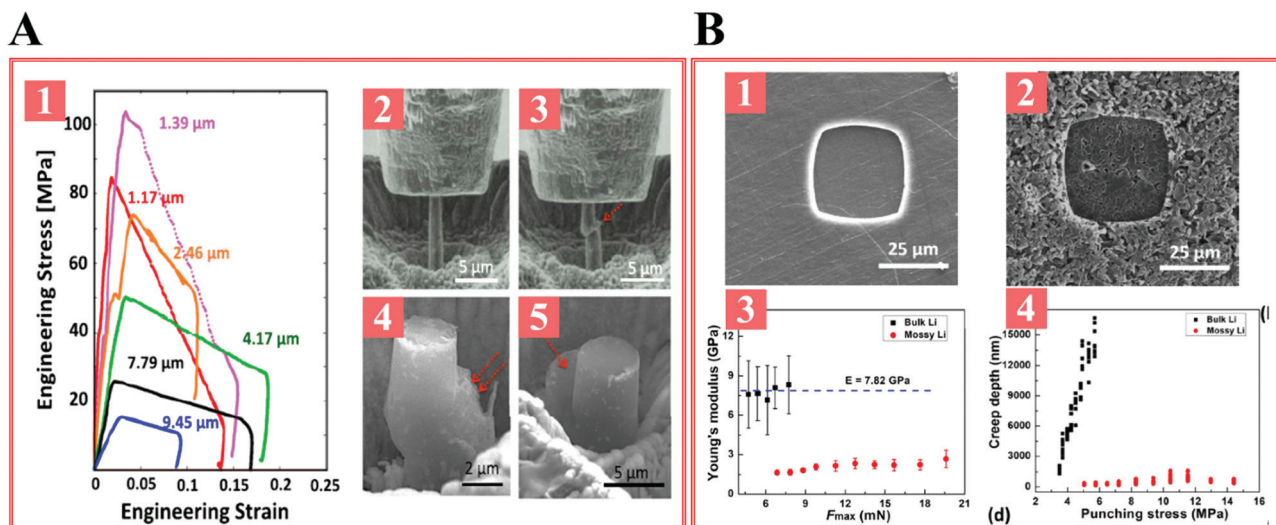


Fig. 16 Mechanical properties of micro-sized Li metal. (A) Compression test of Li micropillars. Reprinted with permission from ref. 203. Copyright (2017) National Academy of Sciences. (B) Indentation test of bulk lithium and electrodeposited mossy Li. Reprinted with permission from ref. 215. Copyright (2019) AIP Publishing.

**Mechanical properties of SEI.** The solid–electrolyte interphase is in direct mechanical contact with Li electrodeposits. The mechanical properties of SEI are therefore important and can govern Li deposition morphology. The SEI formed on Li-ion anodes, *e.g.* MnO, <sup>216</sup> HOPG and Si, <sup>217</sup> have been investigated in a few early studies. The SEI in Li-ion anodes are relevant because the electrochemical potential of these anodes in battery cycling is close to  $\phi_{\text{Li}^+/\text{Li}}$ . As a result, the SEI formed *via* electrolyte reduction is comparable to the one on Li metal anode. Zhang *et al.* measured the elastic modulus of the SEI by AFM indentation. <sup>216</sup> As the tip presses into the sample surface, the AFM records the force (stress) and the indentation depth (strain). The SEI initially exhibits elasticity as evidenced by a linear stress–strain relation, followed by a plastic yield. Statistics show that the Young's modulus has very broad distributions from  $10^1$  to  $10^4$  MPa for the sample discharged to 0.1 V, from  $10^0$  to  $10^4$  MPa for the sample discharged to 0.01 V. The very broad distributions suggest the heterogeneous nature of the SEI. As shown in Fig. 17, the theoretical moduli of possible SEI components have a large difference among each other. <sup>218</sup> The inorganic components' moduli are significantly higher than the organic ones. Yoon *et al.* recently report a novel method to measure the modulus of SEI. <sup>219</sup> A thin layer of Li is vapor deposited on free PDMS substrate, which was later placed in contact with the electrolyte. The electrolyte *in situ* reacts with Li, generating the SEI and a buckled surface pattern of the PDMS film owing to the compressive stress state of the SEI. The topography of the buckled surface was probed by AFM. The SEI modulus can be calculated according to the wavelength of the buckled structure by the so-called strain-induced elastic buckling instability for mechanical measurements. <sup>220</sup> The measurements yield a relatively narrow distribution of modulus values within 1.0 GPa to 2.5 GPa, independent of SEI thickness.

Stress has been already discussed as a factor governing the morphology of Li deposits, but stress is a tensorial quantity and

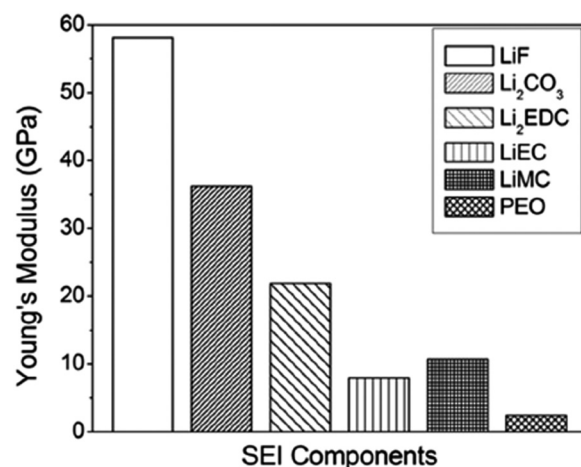


Fig. 17 Theoretical Young's moduli of SEI components. Reprinted with permission from ref. 218. Copyright (2015) Elsevier.

the directions of imposed forces and precise surfaces upon which they act can become complicated in an electrochemical cell. It has been shown for example that, in a prestressed lithium cell, the stress acting on lithium electrode can change from tensile to compressive after metal deposition. <sup>221</sup> In addition to prestress generated in cell assembling (Fig. 18A-1), the Li deposition itself gives rise to a local stress field (Fig. 18A-2). <sup>222</sup> Early studies based on continuum-scale models predict that surface tension resist the formation of high surface area dendritic electrodeposits. <sup>223,224</sup> Monroe *et al.* compared the contribution of surface tension and mechanical stress associated with the growth of Li metal into a PEO separator, and concluded that the mechanical stress is the dominant factor. <sup>194</sup> However, subsequent studies by Tikekar *et al.* showed that if the effect of pressure gradients at a rough electrode on ion transport are properly taken into account, surface tension

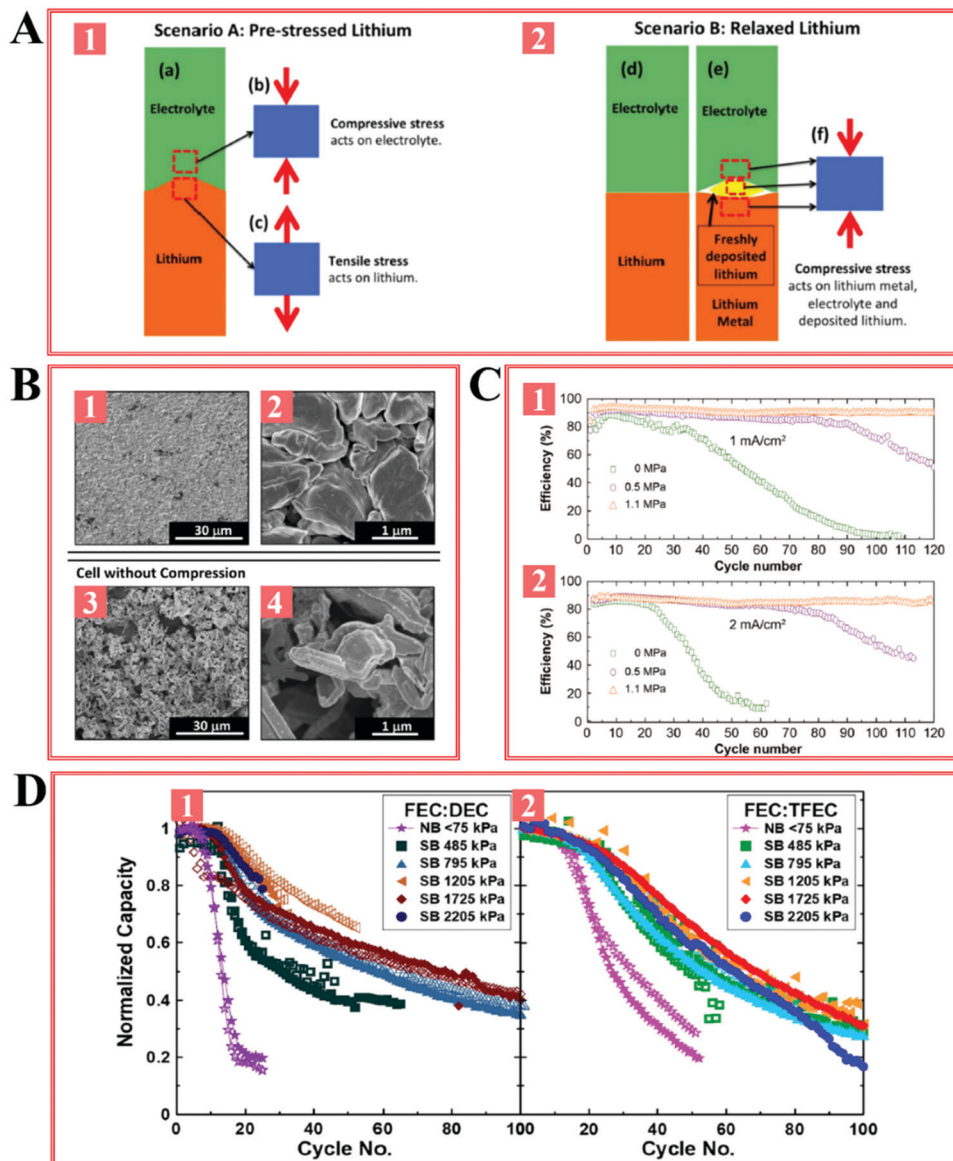


Fig. 18 Influence of mechanical pressure on Li electrodeposition. (A) Model describing the stress state of Li electrodeposit. Reprinted with permission from ref. 221. Copyright (2016) IOP Publishing. (B) Li deposition morphology w/and w/o compression. Reprinted with permission from ref. 228. Copyright (2017) American Chemical Society. (C) Li plating/stripping efficiency w/and w/o compression. Reprinted with permission from ref. 229. Copyright (2018) Elsevier. (D) Capacity retention of anode-free Li metal batteries under different pressure conditions. Reprinted with permission from ref. 230. Copyright (2019) IOP Publishing.

becomes a formidable force in flattening Li electrodeposits on small length scales.<sup>80,83,195</sup> The stabilizing effect of surface tension is also predicted to be much larger in electrolytes, such as single-ion conductors, in which a large fraction of the anions are immobilized.<sup>195</sup>

There are therefore multiple consequences of placing a high modulus electrolyte in direct contact with a Li metal electrode: (a) reducing the reduction reaction rate and hence the exchange current density to the deposit dendrite tip. (b) Driving pressure driven ion transport away from the tips, which produces a more uniform ion flux at the electrode. (c) Creating plastic deformation of Li that, could serve to smooth the electrodeposit morphology.<sup>225</sup> Barai *et al.* produced phase maps (Fig. 19) describing the predicted Li morphology with varying current density and modulus for only a

subset of the three effects.<sup>225,226</sup> A key finding nonetheless is that when the ratio of the imposed current density to the limiting current is low, polymer electrolytes with moduli in the MPa range can facilitate more uniform electrodeposition of Li. Natsiavas *et al.* formulated a model to describe the effect of prestress on the Li<sup>+</sup> transport across the a solid electrolyte and within the Li–electrolyte interface.<sup>227</sup> The pressure can alter chemical potential and lead to pressure assisted diffusion. The model predicts that a modest applied stress (1 MPa) is able to reduce surface roughening of Li electrode.

The effects of imposed stresses on Li deposition morphology have been reported to be both obvious and large, as experimentally observed using various microscopies.<sup>228,229</sup> The Li deposition morphology achieved under compression (1.1 MPa) is significantly

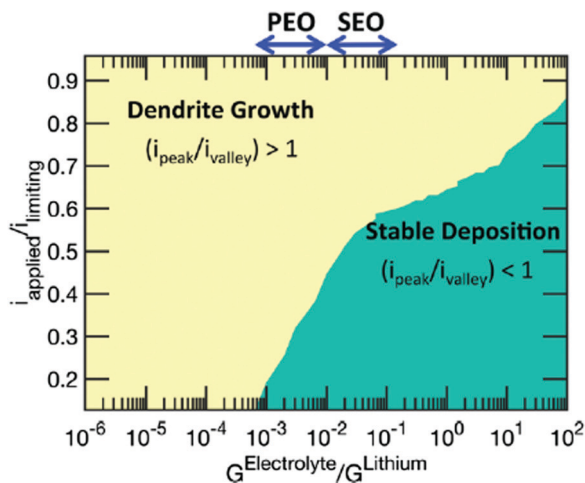


Fig. 19 Phase map showing the effect of current and electrolyte modulus on Li morphology. Reprinted with permission from ref. 225. Copyright (2017) the Owner Societies.

flatter than the Li formed in a pressure-free environment as suggested by the greater diameter of the whiskers under pressure, though it still shows a porous nature (Fig. 18B). Computer simulation suggests that a  $>20$  MPa stack pressure could be able to suppress the formation of void volume during Li plating.<sup>198</sup> He *et al.* directly visualized the growth of Li whisker in the presence of constraint under *in situ* TEM.<sup>66</sup> The authors identified four scenarios—buckling, kinking, yielding and transition from axial growth to lateral growth. This provides direct support that aggressive Li growth can be retarded by stress. Yin *et al.* observed a strong dependence of Li plating/stripping CE on the magnitude of pressure applied, *i.e.* a 5% increase in CE value and a five-fold longer cycle life (Fig. 18C).<sup>229</sup> Louli *et al.* measured the capacity retention of anode-free Li metal under various pressure conditions (0.075–2.2 MPa), and found that 1.2 MPa is optimal for battery operation (Fig. 18D).<sup>230</sup>

Other factors including application of magnetic, gravitational, and buoyancy forces have been reported to influence electro-deposition of metals. The effect of magnetic field on the operation of electrochemical cells has, for example, been of interest for decades.<sup>231,232</sup> And, magnetic fields have been reported to alter electro-deposition morphology of metals, *e.g.* Zn<sup>233,234</sup> and Cu.<sup>235</sup> The effect is understood in terms of the effect of the coupling between the magnetic field  $\mathbf{B}$  and the ionic current to create a Lorentz force,  $\mathbf{F}_L = \mathbf{J} \times \mathbf{B}$ , which creates a convective flux in liquid electrolytes that enhances mass transport. Because the direction of ion migration in an electrochemical cell is generally normal to the electrode, an extra flux with non-zero component in the direction of the electrode surface normal is only possible if  $\mathbf{J}$  deviates from the electrode normal, as occurs near a dendritic deposit. From the definition of the vector cross-product, the Lorentz force normalizes the distribution of cations arriving at the electrode surface. However, since the effect relies on curvature of ionic path-lines induced by non-planarity at the electrode surface it typically requires high magnetic fields to be effective during the early stages of non-planar, dendritic deposition. Recent studies report the influence of magnetic field on Li metal

electrodeposition morphology and find that under certain conditions, Li deposit morphologies are made more planar (Fig. 20A).<sup>236,237</sup> A possible complication in fully ascribing these observations to the induced Lorentz force is that if, as is typically the case for Li, electro-deposition is not limited by mass transport in the electrolyte bulk, but rather by ion transport in and through the SEI, an enhancement of the bulk ion flux alone would seem insufficient to produce the extent of electrodeposit flattening observed in the experiments.

It is known that density gradients in fluids can drive a natural convective flow as a result of the existing buoyancy force.<sup>238</sup> In an electrolyte, such density gradients can couple with electric field lines to produce an unstable electroconvective flow<sup>239</sup> analogous to the classical Rayleigh–Bernard instability produced by temperature gradients in a fluid. The net effect is to create regions near an electrode with increased cation flux produced by downwelling of the heavier ions. If the gravitational and electric fields are antiparallel this classical effect is typically small, if they are parallel, however it is conventionally thought to destabilize ion transport to an electrode producing non-uniform electro-deposition. The effect of gravitational forces on electro-deposition morphology has been demonstrated by Fukunaka *et al.* using Cu electrodes.<sup>240</sup> The authors observed the size of Cu deposits formed at  $10^{-4}$  G is significantly larger than under normal gravity. They interpret their findings in terms of the lowering of the surface cation concentration and number density of electrodeposit nuclei produced by suppressed natural convection in a weak gravitational field. Nishikawa *et al.* visualized a similar Cu electro-deposition process in diffusion-controlled regime by optical microscopy (Fig. 20B).<sup>241</sup> After 8 s deposition at  $2.5 \text{ A cm}^{-2}$ , the Cu pattern obtained under microgravity condition is more uniform, suggesting that the buoyancy induced convective flow does have a significant influence on electro-deposition morphology. Although no analogous effects have been reported for the effect of gravity on Li electro-deposition, it is plausible that similar beneficial effects of low gravity deposition are possible for Li, particularly in a diffusion-limited regime where strong gravitational influences on hydrodynamic stability are predicted by theory.<sup>242</sup>

Gassing is a common phenomenon associated with electrolyte reduction reactions that accompany electro-deposition of metals. The formation of bubbles near the electrode surface is conventionally thought to produce porous, irregular electro-deposition films.<sup>243</sup> *In situ* phase contrast radiology observation shows that the bubbles attached to electrode surface can template Zn electro-deposition. Zn grows laterally on the surface of the bubbles until they are fully covered (Fig. 20C).<sup>244</sup> In Li metal electro-deposition, gases, including  $\text{H}_2$ ,  $\text{C}_2\text{H}_4$  and  $\text{CO}_2$ , are generated during the formation of SEI.<sup>33,245</sup> Zhu *et al.* visualized the interaction between newly-formed bubbles and Li electro-deposits.<sup>246</sup> The bubbles impose a mechanical force on Li deposits and partially fragment the Li. This would also seem to exacerbate formation of dead Li owing to the breakage from the larger deposit or from the substrate. Finally, owing to the low electrochemical potential, Li metal is chemically reactive with nearly all species that can accept electrons. Lin *et al.* investigated the corrosion of Li deposits, which is in essence governed by a galvanic process between Li and the conductive

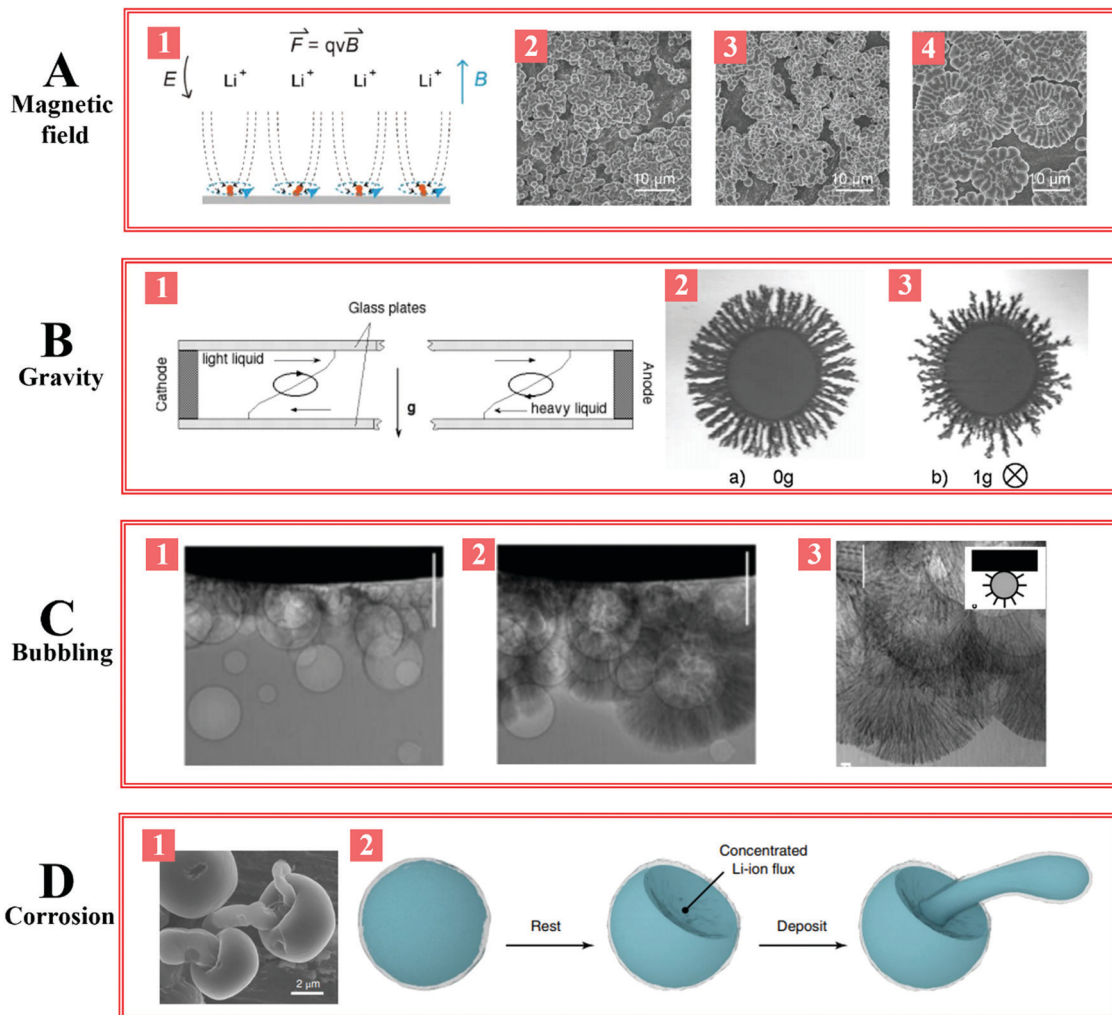


Fig. 20 Influence of other external factors on Li electrodeposition. (A) Effect of magnetic field. Lorentz force is used to suppress the dendritic growth of Li metal. Reprinted with permission from ref. 237. Copyright (2019) John Wiley and Sons. (B) Effect of gravity. Electrodeposition morphology of copper in microgravity conditions and in normal gravity conditions. Reprinted with permission from ref. 241. Copyright (2013) Elsevier. (C) Effect of bubbling. Accumulation of Zn metal deposits on hydrogen bubbles. Reprinted with permission from ref. 244. Copyright (2002) Springer Nature. (D) Effect of chemical corrosion. Illustration showing the morphology evolution of Li electrodeposits caused by chemical reaction. Reprinted with permission from ref. 247. Copyright (2019) Springer Nature.

current collector (Fig. 20D).<sup>247</sup> The authors reported that over-time nearly spherical Li electrodeposits on a Cu current collector can undergo a shape change—from spherical to concave, leading to heterogeneity of the SEI on Li non-uniform Li electrodeposition by the processes already discussed in the review. This observation is of particular importance as it suggests that no matter how uniform the initial Li electrodeposit morphology on the current collector, the deposit topography will over time roughen as a result of galvanic corrosion.

### 3. Towards practical strategies for achieving fine control of Li electrodeposition

#### 3.1 Electrolytes and interphases

In this section we review recent, purpose-driven research aimed at designing electrolytes, interphases, and electrode architectures able

to address fundamental barriers discussed in the previous sections of the review. We do not review the already substantial literature focused on synthesis and design of liquid,<sup>248</sup> including ionic liquids<sup>249,250</sup> & eutectics,<sup>251</sup> solid-state ceramic<sup>252</sup> & polymers,<sup>253,254</sup> and polymer-inorganic hybrid<sup>255,256</sup> electrolytes. An in-depth discussion of the design of solid-state electrolyte can be found in a recent Review.<sup>257</sup> This literature rightly focuses on how intrinsic characteristics, such as molecular structure, chemical bonding, and molecular packing influence crystallinity, ion-pair dissociation, ion transport, mechanical properties and thermal stability of electrolyte solvents. Thus, while it is understood that facile room-temperature ion transport, wide temperature and voltage operating windows and low flammability are the traditional design variables for all electrolytes, we use the discussion about interphases in Section 2.3 to organize the emerging literature focused on electrolyte design rules unique to the lithium metal anode. In so doing we take the traditional requirements as a given and consider the role electrolytes serve as vehicles for

enabling interphase designs able to facilitate fine control of Li electrodeposition and high reversibility of the Li metal anode. The search for practical solutions would be incomplete, however, without consideration of recent progress to overcome the substantial challenges associated with developing electrolyte designs—solid-state, functional ionic liquids, polymers—able to enable safe operation of batteries that utilize a Li metal anode, particularly under abuse conditions. We therefore draw the reader's attention to two comprehensive recent reviews that address this subject,<sup>28,257</sup> to supplement the perspectives reached in this section of the review.

**3.1.1 Designing liquid electrolytes for Li anodes.** We stated previously that the most differentiating aspects of the electrochemistry of battery cells that utilize the Li anode are that interphases formed spontaneously on the metal play a large role in the reversibility of the anode. Because interphases in any electrolyte (liquid or solid) are formed by both chemical and electrochemical reduction reactions between Li and electrolyte components (solvents, salt, additives), understanding how the various components undergo or limit such reactions is an important precondition for good electrolyte design for the Li metal anode. The working mechanism of SEI has been discussed in a handful of excellent reviews.<sup>129,258–260</sup> Briefly, the electrochemical reduction of electrolyte/additives form the SEI in the vicinity of the electrode material surface, which kinetically prevents further electrolyte reduction and selectively allows lithium ions to pass without causing solvent co-intercalation. Chemical reaction between the electrolyte and lithium may also occur spontaneously upon contact, evidenced by the increasing impedance with the resting time.<sup>261</sup> Electrochemical processes may catalyze these reactions or produce new ones which may lead to a too thick SEI on lithium metal to conduct ions in the electrolyte bulk, causing utilization of the anode to degrade overtime.<sup>262</sup> Additionally, unlike the better known graphite anode in LIBs, for which the highly reducing electrode surface can be passivated by the SEI for hundreds of charge–discharge cycles, volume change coupled with the uneven lithium electrodeposition discussed earlier causes the SEI to crack and reform repeatedly, depleting components in the cell (solvent, salt, additives) as well as the Li anode.<sup>263</sup> The strict N:P requirements delineated in the introduction obviously cannot be met under such conditions.

In a typical electrolyte (*e.g.* 1 M LiPF<sub>6</sub>–EC/DMC) there is approximately 6.7 M EC and 5.3 M DMC, meaning that the electrolyte solvent constitutes by far the more numerous species in the fluid bulk. It is then unsurprising that the starting point for the vast majority of studies begins with selecting the electrolyte solvent. In this regard, linear and cyclic ethers and their alkyl carbonate esters created by reaction of the ethers with carbon dioxide are among the most common choices for a variety of reasons.<sup>20,83,262–265</sup> First, they are able to coordinate with and solvate Li<sup>+</sup> ions by virtue of classical (*e.g.* high dielectric constant) and non-classical (*e.g.* ability to share electrons on an ester or ether oxygen with Li<sup>+</sup>), which ensures that they provide large numbers of mobile charge carriers in solution than would be anticipated from their dielectric constant alone.

Second, they readily form mixtures with each other, which makes it possible to formulate a wide range of electrolyte compositions with few starting components, including electrolytes with low viscosities at room temperature. Finally, they can oligomerize/polymerize at the reducing potentials at the Li anode to produce polymer by ring-opening and/or anionic mechanisms.<sup>83,133,263,266,267</sup>

The most straightforward and scalable approach to tune the SEI of lithium metal is therefore by blending effective additives into the electrolyte, which preferentially interact with the lithium anode surface prior to battery cycling. For instance, vinylene carbonate (VC) and fluoroethylene carbonate (FEC) are two additives widely used in typical carbonate-based electrolytes (*e.g.* 1.0 M LiPF<sub>6</sub>/LiTFSI/LiFSI in EC:DMC, EMC or DEC) as reported in literature.<sup>143,151,268,269</sup> Their working mechanism is similar to that on a graphite anode, which involves undergoing reduction prior to the dominating solvents and forming a robust, stable and ion-conductive oligomer/polymer film. Depending upon the constituents, the formed polymer layers may either coat the anode to protect it (*e.g.* FEC and VC)<sup>65,143,146</sup> or otherwise may serve as binders to other components of the SEI together. The quality of SEI may therefore vary significantly with electrolyte components and thus careful design is non-trivial. A well-known example is the minor difference between ethylene carbonate (EC) and propylene carbonate (PC) result in completely distinct anode stability characteristics.<sup>270,271</sup> In most carbonate esters, the reactions proceed continuously and tailored strategies including addition of sacrificial, easily reduced organic species<sup>147,149,151,272</sup> are required to stop runaway of the interface impedance and to limit loss of active materials.

A trace amount of additives may change the properties of SEI fundamentally and thus provide stability. Studies have shown that doping DOL/DME based electrolyte with <<1% LiNO<sub>3</sub> benefit lithium electrodeposition in Li/S cells, which can work synergistically with other additives such as Li<sub>2</sub>S.<sup>273,274</sup> Effective additives include gaseous species, ionic liquids, surfactants, aromatic compounds, alkali metal salts, *etc.* While these additives cover a broad range of material categories, they share some common features that offer insights for the future design of SEI additives. It is obvious SEI forming additives are required to possess a high HOMO and low LUMO compared with other components in the electrolyte to ensure full formation.<sup>259</sup> Preferentially as-formed SEI films should be homogeneous and chemically stable against lithium metal at a large time scale. A balance of inorganic/organic composition of such films is equally critical, as low-crystallite organic portion provides elasticity and solvent compatibility, whereas the inorganic parts contribute to the ionic conductivity.<sup>262</sup> It is worth noting that SEI forming additives are self-sacrificial in nature, and thus will deplete gradually by forming new SEI on freshly deposited Li as cycling continues.<sup>275</sup> Thus, it is still of risk to use SEI forming additives alone to stabilize lithium metal anode, especially when a significant amount of battery cycles is needed. Most SEI additives are added in the electrolyte and become effective by undergoing electrochemical reduction during the formation cycle and following few operation cycles. Occasionally, additives that are beneficial to lithium

electrodeposition may not be most favorable to full cell, either from the perspective of economy or cathode compatibility.<sup>147</sup> Thus, pretreatment of lithium metal with these chemicals prior to the cell assembly is proposed as an option. A number of chemicals in either liquid or gas form, including ionic liquids, boric acid,  $\text{GeCl}_4$ ,  $\text{SiCl}_4$ , frenon, *etc.* have been applied to lithium surface to promote the spontaneous reaction to form stabilizing SEI.<sup>276–279</sup> The pretreatment of lithium metal avoids undesired side reactions of additives in the electrochemical cell and lowers the cost of electrolyte. However, the Li pretreatment brings challenges to the manufacturing due to the high reactivity lithium. Thus, continuous and safe production processes are urgently required for this promising lithium protection strategy.

Another class of electrolyte additives contribute to improving SEI indirectly, as they do not participate in chemical or electrochemical decomposition, but enrich in SEI to regulate or decelerate SEI re-forming by harnessing uneven lithium plating. In other words, these additives work physically on the Li metal surface to prevent lithium dendrite growth. Electric repulsing has been applied to smoothen lithium electrodeposition.<sup>280</sup> By carefully adding alkali metal ions such as cesium that possess a lower reduction potential than lithium ions, a positively charged SEI can be realized which homogenizes the lithium electrodeposition. While theoretically the mechanism only works in a narrow alkali ion concentration, further studies reveal that additives such as  $\text{KNO}_3$  benefit the cycling of Li-NCM cells.<sup>281</sup> As already noted, Lithium binary halide salts (*e.g.*  $\text{LiF}$ ,  $\text{LiBr}$ ) represent another category of physical SEI additives which regulate the surface diffusion energy of lithium ions.<sup>282</sup> By promoting fast surface ion mobility, such salt additives are thought to promote long term stable lithium plating/stripping.<sup>171</sup> More exotic yet efficient additives have also been reported, such as insoluble nanodiamond being co-deposited on the lithium surface.<sup>283</sup> First principle calculation indicates the nanodiamonds also present a low diffusion energy barrier for lithium ion and thus contribute to stable lithium electrodeposition. Even the salt composition used in an electrolyte can be formulated for enhancing properties of the SEI.  $\text{LiPF}_6$ ,  $\text{LiBF}_4$ ,  $\text{LiBETI}$ ,  $\text{LiTFSI}$ , *etc.*<sup>284,285</sup> are among the most popular lithium salts used for maintaining high ionic conductivity in the electrolyte bulk, while salts like  $\text{LiNO}_3$ ,  $\text{LiTf}$ ,  $\text{LiDFOB}$  and  $\text{LiBOB}$  known to undergo facile reduction reaction at the lithium anode are used as SEI formers.<sup>273,286</sup> The oxidative window of electrolytes can also rely on the nature of salts in a lithium metal battery. For example, salts like  $\text{LiTFSI}$ ,  $\text{LiTf}$  are known to cause Aluminum corrosion, thus preventing the high voltage operation using cathodes like  $\text{LiNMC}$  or  $\text{NCA}$ . On contrary, salts like  $\text{LiPF}_6$  or  $\text{LiBF}_4$  are effective in operating window as high as 5.1 V *vs.*  $\text{Li/Li}^+$ . Recently, it has been found that  $\text{LiPF}_6$  salt additive as low as 0.05 M is effective in suppressing Al corrosion by formation of a thin film of  $\text{AlF}_3$  layer.<sup>287</sup> Thus, several combinations of salts in the electrolyte have been regarded as effective in suppressing different aspects battery instabilities (like lithium metal deposition and cathode potential). Previously, Zheng *et al.*<sup>288</sup> showed that combining 0.6 M  $\text{LiTFSI}$ , 0.4 M  $\text{LiBOB}$  along with 0.05 M  $\text{LiPF}_6$  is effective in enabling stable cycling of  $\text{Li}||\text{NMC}$  battery for over 500 cycles with a retention of 97.1% capacity. Recent work by Weber *et al.*<sup>289</sup> utilized

a solvent combination of  $\text{FEC}:\text{DEC}$  (1:1) and studied the effect of  $\text{LiPF}_6$ ,  $\text{LiDFOB}$  and  $\text{LiBF}_4$  salts. They found that the combination of 0.6 M  $\text{LiDFOB}$  and 0.6 M  $\text{LiBF}_4$  is most effective in stabilizing the lithium metal deposition and operation of high voltage NMC cathode. In fact, they were able to cycle an anode-free battery ( $\text{Cu}||\text{NMC}$ ) for 90 cycles with 80% retention.

It is understood however that the electrolyte solvent used in a lithium battery must only be capable of forming good interphases at the reducing potentials at the anode, but must also be stable at the oxidizing potentials at the cathode. Interestingly, many studies have shown the dilemma of choosing the right solvent that can simultaneously form a stable SEI on the lithium metal and at the same time withstand high electrochemical potentials of the cathode. For example, ether-based electrolytes have been reported to form a polymeric SEI on the metal anode that is robust and ion conducting. However, the ether electrolytes typically breakdown at a voltage of 3.81 *vs.*  $\text{Li/Li}^+$ , thus they cannot serve as the solvent for high voltage batteries. On the contrary, carbonate-based electrolytes show high oxidative stability at least up to 4.2 V, however they are poor SEI formers on the lithium anode. Hence, there has been a significant attempt at designing new or combining known solvents that can effectively address the issues of both electrodes. For example, Yang *et al.*<sup>290</sup> recently showed that liquified gas electrolyte comprising of fluoromethane (FM) can be mixed with tetrahydrofuran (THF) that has the desirable solvation structure and transport properties. This electrolyte is shown to have high lithium transference number of 0.79 and shows dramatic improvement in the coulombic efficiency of over 99% at even high current densities. Furthermore, the rate performance is well maintained in a wide range of temperature from 20 °C to  $-60$  °C.

A novel approach that shows promise for addressing electrolyte stability at both electrodes and at the same time reducing electrolyte volatility for improved battery safety is to increase the concentration of salt to achieve molarities comparable to those of the solvent.<sup>291</sup> In so doing, simple liquid electrolytes can be transformed to systems that resemble room temperature ionic liquids, but with higher room temperature cation mobilities and higher cation transference numbers. Interestingly, it was been observed that raising the concentration to very high values (example 7 M), the lithium transference number increases to up to 0.74, while the conductivity doesn't significantly change. Because the counterion concentration in such super-concentrated electrolytes is as high as that of the solvent, anions that are more stable at the anode potentials than the base carbonate ester or ether liquids can impart enhanced resistance to chemical degradation at the lithium anode, improving overall anode reversibility. Qian *et al.*<sup>264</sup> systematically varied the salt concentration of  $\text{LiFSI}$  in DME solvent from 1 M up to 4 M and showed that electrolyte can enable stable cycling of  $\text{Li}||\text{Li}$  symmetric cells even at high rate of 10  $\text{mA cm}^{-2}$  for more than 6000 cycles (Fig. 21a). Consequently, Qian *et al.*<sup>21</sup> demonstrated that the high salt electrolyte (4 M  $\text{LiFSI}$  in DME) is effective in cycling of a  $\text{Cu}||\text{LiFePO}_4$  anode-less cell even at a high rate of 2  $\text{mA cm}^{-2}$  for 100 cycles with discharge capacity retention of about  $\sim 55\%$ .

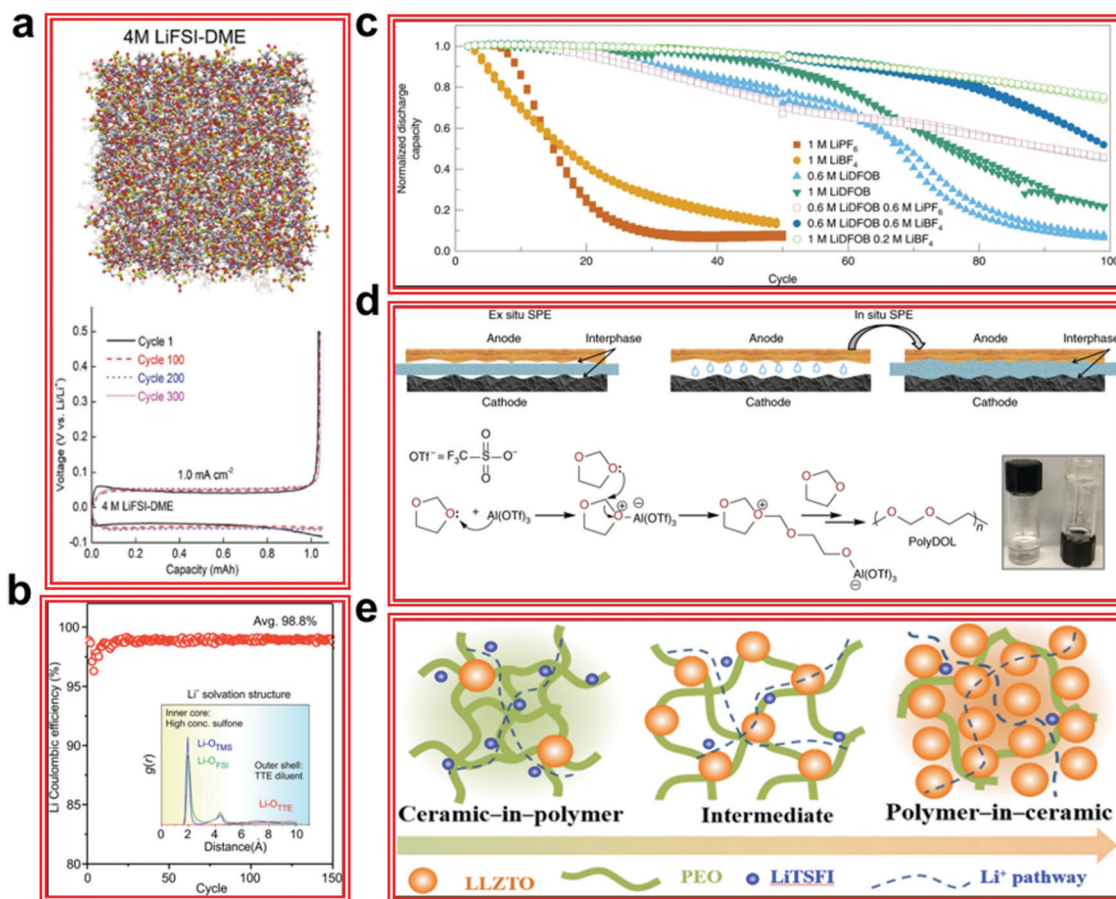


**Fig. 21** Electrolyte innovations for stabilized Li metal anode. (A) Superconcentrated electrolytes based on 4 M LiFSI in DME stabilizes deposition of lithium by solvent–salt coordination. Reprinted with permission from ref. 264. Copyright (2015) Springer Nature. (B) Localized high concentration electrolytes are successful in maintaining low viscosity while improving the local concentration of salts and thereby the performance. Reprinted with permission from ref. 300. Copyright (2018) Elsevier. (C) Fine tuning of the salt and solvent chemistry and ratio can lead to very stable performance of lithium metal battery in an anode free configuration with high voltage operation.<sup>315</sup> Copyright (2018) Springer Nature. (D) Using an *in situ* polymerization method, it is possible to improve the interfacial conductivity of solid polymer electrolytes. Reprinted with permission from ref. 316. Copyright (2019) Springer Nature. (E) Increasing the ceramic content in the composite electrolyte it is possible to maintain the particle–particle contact for transport while retaining flexibility due to polymers. Reprinted with permission from ref. 322. Copyright (2018) Elsevier.

The fundamental reason for the extended stability of liquid electrolytes with high concentrations of soluble salt is now known to be two-fold: (1) the solvent molecules in the electrolyte is highly solvated by the salt components, thus the side reactions of the solvent and corrosion effects are significantly mitigated; (2) the interfacial layer (SEI) is derived primarily from the salt components rather than the solvent, which is known to be more robust, flexible and conducting. The concept of super-concentrated electrolytes has been extended to even reactive solvents like propylene carbonate (PC),<sup>292,293</sup> dimethyl sulfoxide (DMSO)<sup>294</sup> and acetonitrile (AN).<sup>295</sup> For example, it is known that PC co-intercalates with lithium into graphite anode in lithium ion batteries, however, Jeong *et al.*<sup>292,296</sup> showed that concentrated PC electrolytes based on LiBETI (lithium bis(perfluoroethylsulfonyl) imide) salts up to 2.72 M can result in significant intercalation of lithium into graphite. They found that the high concentration electrolyte forms an ultra-thin SEI layer (~8 nm) that prevents the co-intercalation of PC solvent molecules and also suppresses the breakdown or consumption of the electrolyte. Furthermore, high salt concentration in the electrolyte also

enables the use of solvent components which are traditionally known to corrode the lithium metal or breakdown at high potentials. Suo *et al.*<sup>152</sup> reported that at a high concentration of 7 M LiFSI in pure FEC solvent can result in a predominantly fluorinated SEI that improves the coulombic efficiency of lithium metal battery cycling to 99.64% and excellent compatibility with a 5 V LiNiMnO cathode. Other reports have shown that previously corrosive solvents like triethyl phosphate (TEP) and trimethyl phosphate (TMP) can also be utilized with a high salt-to-solvent ratio.<sup>297,298</sup> These phosphate-based solvents are excellent fire-retardants that prevent thermal runaway in batteries.

Typical electrolytes comprise of a polar solvent and lithium salts; however, several recent studies have explored a third component as a non-solvent in the electrolyte. Typically, salts used in electrolytes are insoluble in this non-solvent, while the solvent pairs are chemically miscible. In such a scenario, it is found that the salt is concentrated in the solvent phase even when the overall salt solution is dilute (~1 or 2 M), thus known as local-high concentration electrolytes (LHCE) (Fig. 21b).

The main advantage of such a combination over the super-concentrated electrolytes is the low viscosity and cost. Previously Chen *et al.*<sup>299</sup> has shown that using 1.2 M LiFSI in a mixture of DMC (good solvent) and BTFE (poor solvent) in a 1 : 2 molar ratio can enable dendrite-free cycling with high coulombic efficiency of 99.5% and capacity retention of over 80% after 700 cycles in a Li||NMC cell. Ren *et al.*<sup>300</sup> further showed that the LHC electrolytes based on fluorinated ethers (1,1,2,2-tetrafluoroethyl-2,2,3,3-tetrafluoropropyl ether) can even outperform high concentration electrolytes in terms of coulombic efficiency and capacity retention. Similarly, tris(2,2,2-trifluoroethyl)orthoformate (TFEO) based fluorinated non-solvating components are also shown to be effective and the mechanism for the stabilization is regarded to be similar to that of high concentration electrolytes, specifically a fluorine-rich SEI and highly solvated solvent molecules.<sup>301</sup>

**3.1.2 Polymeric electrolytes.** An immediate benefit of covalently connecting individual molecular ethers or carbonate esters end-to-end is to create macromolecules with the same chemical characteristics, but substantially lower volatility and chemical activity.<sup>302,303</sup> Additionally, by cross-linking these molecules to form polymer networks, electrolytes with vastly improved mechanical characteristics and reduced propensity to leak can be constructed. Whether used as stand-alone materials or as frameworks in conventional liquid electrolytes provide multiple functionalities that can be leveraged to stabilizing electrodeposition of metallic lithium in a battery. Previous stability analysis by Tikekar *et al.*<sup>80</sup> revealed that electrolytes with high modulus and lithium transference number electrolytes are effective in suppressing dendrites. Researchers, in the past have utilized various polymeric matrices based on PMMA,<sup>304</sup> siloxane,<sup>305</sup> or aramid fibers<sup>306</sup> to enhance the electrolyte modulus. Balsara and co-workers demonstrated that using PS-PEO block copolymers as solid-state electrolyte that comprise of PEO based conducting pathways and mechanical strength provider in form of PS.<sup>307</sup> Similarly, Khurana *et al.*<sup>200</sup> showed one of the highest short-circuit time using a crosslinked structure of PE-PEO. Similar works using commercial nanoporous anodized Al<sub>2</sub>O<sub>3</sub>,<sup>201</sup> cross-linked silica nanoparticles<sup>308</sup> and aligned nanoporous polyimide filled with PEO polymer<sup>309</sup> are also known to be effective in enabling stable cycling of metal anodes. Perhaps, a commonality shared across these nanostructured polymer electrolytes is the tortuosity and nanopores which are formed either by self-assembly or by mechanical processing. In a previous mechanistic study, it has been shown that designing polymer electrolytes having nanopores below 100 nm results in restriction of lithium nucleation size below a critical limit that restricts its dendritic growth.<sup>202</sup> Polymer electrolytes are also effective in tuning the ion transport properties to enable stable electrodeposition. For example, it has been previously shown that commercial polymer Nafion that has sulfonic acid side groups possess high lithium transference number, while having the ion conductivity of 10<sup>-5</sup> S cm<sup>-1</sup>.<sup>310</sup> Similarly, various forms of UV-crosslinked<sup>311</sup> and block-copolymer PEO electrolytes<sup>312</sup> are known to maintain high transference number while having moderate ion conductivity for battery operation because of anionic side chains incorporated in the backbone. Interestingly, most polymer electrolytes

reported in the literature comprise of polyethylene oxide (PEO) as the primary component. However, it is known that ether-based electrolytes are ineffective in withstanding high potential at the cathode that restricts their usage in a high voltage lithium metal battery. Several recent works have shown that using additives in these ether-based electrolytes can enhance the oxidative stability. Particularly, boro-oxalate based additives (LiBOB, LiDFOB) are known to stabilize both oligomeric and high molecular weight ethers at these high potentials, thus enabling stable cycling of Li||NMC batteries (Fig. 21c).<sup>313,314</sup> Recent works have shown that these borate salts breakdown at high potentials to form supra-molecular aggregates having anionic backbones that prevent the decomposition of the ethers.<sup>315</sup> Owing to the tunability and processability of polymers, it is possible to enable fast interfacial ion transport even in all-solid state electrolytes. For example, Zhao *et al.*<sup>316</sup> previously showed that a cationic aluminum additive in DOL based liquid electrolytes can result in ring-opening polymerization inside the electrochemical cell, thus forming *in situ* solid electrolytes that possess good conformity with both electrodes; thus, it is possible to cycle such battery even in ambient conditions (Fig. 21d).

**3.1.3 Ceramic electrolytes.** The critical benefit of using all solid-state batteries is the enhanced safety because of the absence of any flammable or volatile components (typically liquid or oligomeric electrolytes). Additionally, the solid electrolytes are mechanically tough to resist dendrite growth during lithium deposition and at the same time the side reactions between the electrode and electrolyte is greatly suppressed in solid state. Previously, Li *et al.*<sup>317</sup> has shown that microbatteries in Li||NMC configuration is effective in stable cycling for more than 10 000 cycles without loss of capacity using LiPON based solid electrolytes. However, several challenges limit the scalability of the solid-state electrolytes, including, (1) high interfacial resistance due to the irregularities and contact issues between the electrolyte and solid electrolytes, (2) dendrite growth due to the poor conductivity in these solid electrolytes that leads to ion polarization even at relatively low currents, (3) poor processability because of the brittle and fragile nature of the inorganic solids, (4) incompatible with high voltage cathodes due to the low oxidative stability of the solid electrolytes. To mitigate the issues of the interfacial conductivity, Han *et al.*<sup>318</sup> previously, designed an artificial interface on the garnet solid electrolyte (LLCZN) based on ALD deposited aluminum oxide. This allowed the surface wetting of lithium metal enabling smooth ion transport, which reduced the interfacial resistance from as high as 1710 Ω cm<sup>2</sup> to 1 Ω cm<sup>2</sup>. Furthermore, researchers have evaluated the concept of forming bi-layer structures, where the solid-state electrolyte is protected by a buffer polymer layer that prevents the breakdown of the ceramic components and ensures charge transport. For example, Wang *et al.*<sup>319</sup> used high molecular weight PEO as interlayer for the Li<sub>1.5</sub>Al<sub>0.5</sub>Ge<sub>1.5</sub>(PO<sub>4</sub>)<sub>3</sub> ceramic electrolyte that resulted in successful operation of a lithium metal battery with LiMn<sub>0.8</sub>Fe<sub>0.2</sub>PO<sub>4</sub> cathode. Gao *et al.*<sup>320</sup> and Chinnam *et al.*<sup>321</sup> developed surface modification techniques using *in situ* polymerization and silanization, respectively to achieve low resistance for ion transport at the interface. A common feature shared across all these polymer interfaces is the

creation of SEI layer derived from the polymer itself, thus they suffer from the same issues as polymer electrolytes.

A promising area of research in solid electrolytes is utilizing composites comprising of polymers and inorganic particles as blend. In this configuration, the polymer can provide the flexibility, processability and good interfacial contact, while the inorganic solids can enhance the ion conductivity and provide mechanical strength to prevent dendrite growth. Chen *et al.*<sup>322</sup> introduced the idea of using polymer-in-ceramic rather than ceramic-in-polymer, such that there is good contact between the ceramic surfaces (Fig. 21e). They were able to achieve high conductivity of  $10^{-4}$  S cm<sup>-1</sup> at 55 °C and a low impedance for lithium plating and stripping using a 'hot-press processing method. Furthermore, they were able to achieve stable cycling of Li||LiFePO<sub>4</sub> in solid state configuration that retained over 90% capacity for at least 100 cycles. Some of the other composites reported in the literature include Li<sub>6.4</sub>La<sub>3</sub>Zr<sub>1.4</sub>Ta<sub>0.6</sub>O<sub>12</sub>/PEO/succinonitrile blend,<sup>322</sup> PVdF/Li<sub>1.3</sub>Al<sub>0.3</sub>Ti<sub>1.7</sub>(PO<sub>4</sub>)<sub>3</sub>,<sup>323</sup> Li<sub>7</sub>P<sub>3</sub>S<sub>11</sub>-PEO-LiClO<sub>4</sub>,<sup>324</sup> among others. In a systematic study using solid-state NMR for a LLZO-PEO system,<sup>325</sup> it is observed that the ion conduction is much faster through the conducting ceramic in comparison to that in the polymer phase. However, the requirement for the conduction along the ceramic particles is presence of a continuous channel by surface to surface contact. They also found that the interfacial conduction between the ceramic and PEO is limited and only happens by Li ion migrating from ceramic to polymer by creating vacancy. Due to the mismatch of mobility, ion concentration and the solvation structure, there is a formation of space-charge layer. Several researchers have aimed to mitigate the issues of transport pathway by designing aligning the particles or nanowires along the electric field, while ensuring good surface contact between the ceramics.<sup>326,327</sup>

### 3.2 Building artificial solid electrolyte interphases

The SEI formed on a cycled Li metal anode is far more complicated in its topography than the analogous SEI formed on graphite,<sup>328</sup> the chemical make-up of the interphases formed in ethers and carbonate esters are quite similar with organic species, dominantly CH<sub>3</sub>COOLi, CH<sub>3</sub>CH<sub>2</sub>COOLi, and inorganic components including LiF, Li<sub>2</sub>CO<sub>3</sub>, Li<sub>2</sub>O *etc.* coexisting with lithium salts. Considering that the Li<sup>+</sup> insertion potential at the graphite anode is only approximately 200 mV above the potential at which Li electrodeposition occurs at the Li metal anode, these similarities are unsurprising because all components in the typical electrolytes discussed in the previous section are reduced at these potentials. It is then the relative thermodynamic stability of the reduction products that determine the composition of the SEI and their abundance is determined by their relative molar ratio in the electrolyte bulk.<sup>167</sup> These similarities unfortunately disappear when one compares the electrochemical stability of the respective SEI as determined from measurements of their respective Coulombic efficiency—the capacity ratio of the predetermined lithium plating capacity over the lithium stripping capacity over extensive cycling. For example, whereas CE values exceeding 99.99% are possible with the graphite anode, until recently it was rare to measure CE values

exceeding 95% in ether-based and 90% in carbonate-based electrolytes.

Additionally, while ether and ester based electrolytes have been found to be able to form a compact, smooth SEI on lithium surface, and thus a high CE and stability,<sup>264,329</sup> they are readily oxidized at 4 V class cathodes. Carbonates electrolytes are more practical at these higher voltages as demonstrated in LIB history but judging from the CE values are not intrinsically compatible with lithium metal.<sup>330</sup> This situation has motivated interest in so-called artificial SEIs formed either outside the battery cell or created inside the cell using purpose defined electrolyte additives.

Ideally, a successful artificial SEI (ASEI) for the Li metal anode must have following attributes (Fig. 22). (1) LM-SEI should be able to effectively regulate ion transport by allowing lithium ion to pass but limit the access of solvents to the reactive lithium surface; (2) should be mechanically robust to maintain its intactness and suppress the uneven dendrite growth; (3) can lower the charge-transfer resistance and lithium nucleation energy barrier, and maintain the fast kinetics throughout the extensive cycling; (4) ensure coherent contact between lithium metal and bulk electrolyte, which is particularly critical in solid electrolyte systems; (5) need to be manufacturing feasible and scalable in a safe manner. Compared with SEI formed naturally, artificial SEI is structurally controllable, compositionally tunable, and can generate unique hierarchy and functions. Inspired by theoretical and experimental investigation described in Section 2.3, a range of materials including polymers/oligomers, bulk and thin ceramics, inert or active metals, carbonaceous materials, and their hybrids have been prepared as artificial Li metal SEI with various structures. Efforts to seek for ideal SEI lead to the investigation on a wide range of available materials ranging from organic molecules, polymer/oligomer, ceramic, metal/semiconductors, carbonaceous materials, and their composites. In the following section, designed interphase will be discussed in categories based on the material classes, covering their distinct features, properties and preparation approaches.

**3.2.1 Polymeric and oligomeric interphases.** A polymer/oligomer artificial SEI on lithium metal is considered particular promising. The backbone of the polymer and its side groups can be engineered to fulfill a number of purposes simultaneously, offering following benefits:<sup>83,253,331</sup> (1) Polymer SEI can give high conductivity and high local Li transference number due to its compatibility with solvents and coordination with ions. (2) Polymers can be easily designed to be elastic and resilient (*e.g. via* covalent cross-linking) to accommodate the volume expansion induced by lithium electrodeposition or to be self-healing (*e.g. via* ionic or hydrogen bonding to repair a broken SEI). (3) A number of polymer backbone chemistries are thermodynamically (*e.g.* polyethers) or kinetically (*e.g.* through chemical cross-linking or dense surface grafting) or stable against lithium. (4) The coating procedure of polymeric SEI is readily scalable and provide good adhesion between the lithium and polymer. A number of other intrinsic properties of polymer coating can significantly affect the lithium electrodeposition behavior as well.<sup>332</sup> Dielectric constants,

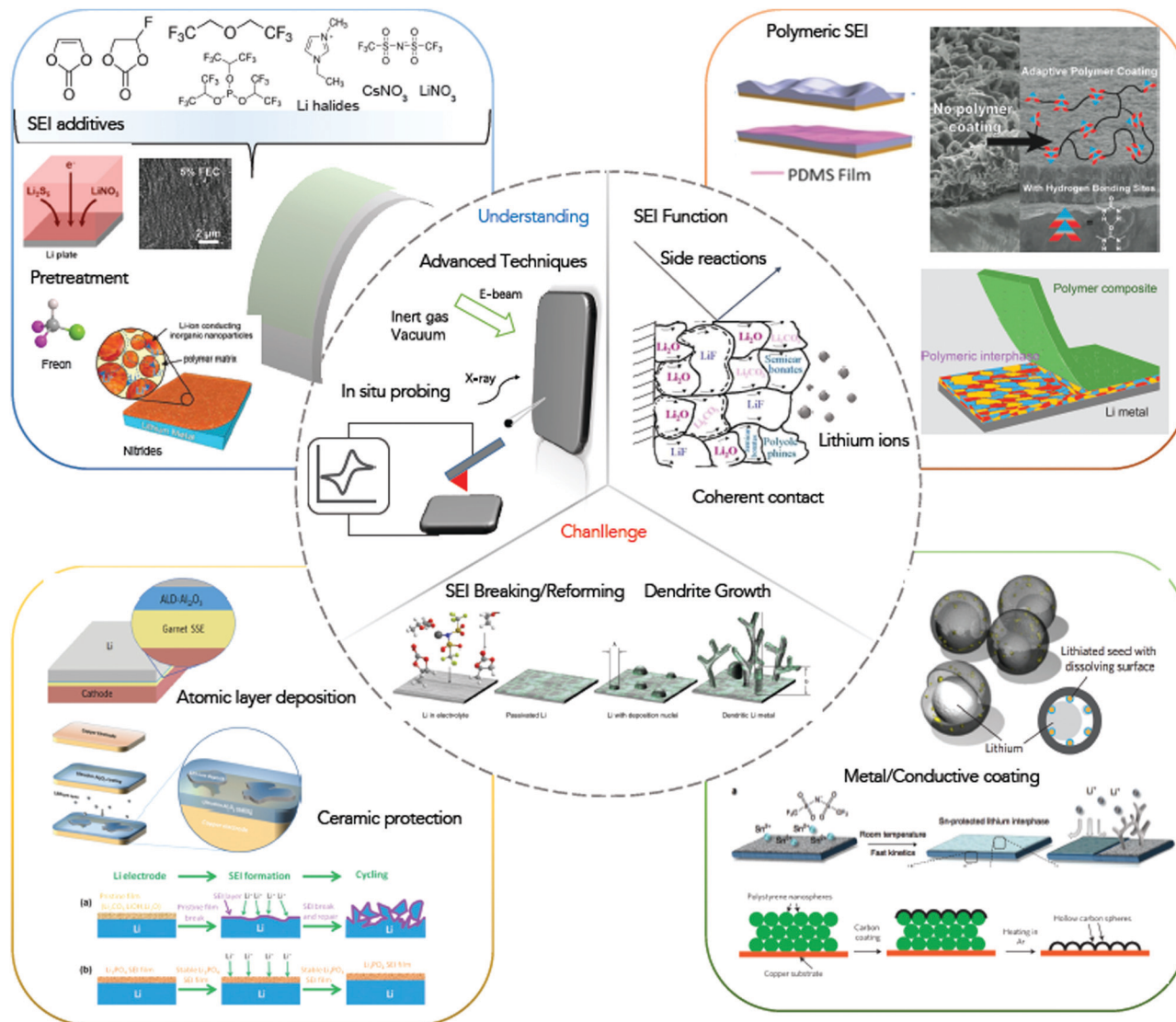


Fig. 22 Design principles of artificial solid electrolyte interphase. The diagram illustrates current challenges associated with alkali metal anodes and potential approaches to overcome them that are based on fundamental understanding. Some representative works are shown in this figure which includes but not limited to electrolyte innovation, surface/interphase treatment, and structural control. Reprinted with permission from ref. 22, 151, 273, 278, 280, 318, 344, 345, 352, 353, 358, 438 and 439. Copyright (2018) American Chemical Society. Copyright (2017) John Wiley and Sons. Copyright (2015) Springer Nature. Copyright (2017) American Chemical Society. Copyright (2013) American Chemical Society. Copyright (2017) Springer Nature. Copyright (2017) John Wiley and Sons. Copyright (2017) American Chemical Society. Copyright (2017) John Wiley and Sons. Copyright (2016) Springer Nature. Copyright (2019) Springer Nature. Copyright (2014) Springer Nature.

interfacial energy, coating thickness, *etc.* can contribute to the exchange currents and nucleation energy of lithium electrodeposits and further the battery stability.

One strategy to develop polymer artificial SEI may be inspired by the application of PEO based solid state electrolyte, which renders reasonable conductivity at room temperature and has good compatibility with lithium.<sup>333,334</sup> An artificially coated PEO on Cu has demonstrated the potential to suppress dendrite growth and provided ~100% CE for over 200 cycles. The design represents one step towards the 'holy grail' of the 'anode-free' LMB which essentially all lithium is stored in the cathode after cell assembly.<sup>335</sup> It is challenging to coat PEO directly on lithium. However, the calendar process reported by

Kim *et al.* for transferring Langmuir Blodgett films deposited on Cu foil to Li provides a potential solution that is also scalable.<sup>336–338</sup> The disadvantage of PEO based material is the poor high voltage stability, that so far the success can only be achieved when using low voltage cathodes such as  $\text{LiFePO}_4$ . Using it as an artificial SEI may solve the issue as it will only contact anode, but a separate design of the electrolyte facing the cathode is needed to satisfy the compatibility.

Another important category artificial polymer SEI are based on fluorinated polymers, which exhibit excellent high voltage stability up to 5 V. For example, PVDF has been widely as the cathode binder due to its excellent chemical and electrochemical stability owing to rich electron-withdrawing F atoms on the

backbone. With slight modification to add flexible segments, PVDF derivative, PVDF–HFP shows the potential to be used as the artificial SEI.<sup>339,340</sup> Nafion is a charged fluorinated polymer originally developed as ion exchange membranes for fuel cells. The unique ionic feature and the fluoro-rich backbone allow it to serve as a promising artificial SEI to stabilize lithium metal. Upon lithiation, Nafion provides high lithium transference number since anions are immobilized on polymer. This, together with its chemistry benefits and reasonable mechanical strength, have been proven to suppress dendrite growth and enable LMBs with long cycle life.<sup>103,341,342</sup> Based on the mechanism similar to Nafion, a number of polyelectrolytes are also investigated as artificial interphase to improve lithium electrodeposition. Utilizing the layer-by-layer assembly technique, either positively or negatively charged polymers such as PAH/PHH can be coated on lithium with precisely controllable thickness.<sup>343</sup> The charged polymeric SEI is also expected to be effective on blocking undesirable species, such as high order polysulfide, either by trapping or electrostatic repulsion.

High elasticity polymer coatings based on hydrophobic polymers such as PDMS represents a family of attractive polymer artificial SEI due to their ability to passivate the Li electrode and well-known design rules (*e.g.* cross-linker molecular weight and density), for accommodating to the volume expansion. Similar function can be achieved with crosslinked polymer, in which the elasticity originates from tunable crosslinker/polymer segment ratio.<sup>344</sup> More exotic material such as polly dolley has been applied as a soft, self-healing coating on lithium metal, which underscores the effectiveness of using high elasticity polymer SEI to protect lithium metal anode.<sup>345</sup>

**3.2.3 Ceramic and polymer–ceramic hybrid interphases.** As discussed previously, dendrite growth and undesirable side reactions work in tandem that deteriorate the stability of lithium metal. Applying ceramic artificial SEI has been considered as a promising strategy to address both issues due to its high modulus and chemical inertness.<sup>262</sup> Compared with polymer, ceramics SEI are typically of orders of magnetite higher Young's modulus and typically are not wetted by aprotic organic electrolytes commonly used in Li metal batteries.<sup>218</sup> The characteristics of ceramic SEI offer them advantages as mentioned but also bring downsides that need careful address. The brittleness of ceramic can trigger fracture if a significant amount of lithium is deposited beneath. Special coating approaches are generally needed to create a pinhole-free ceramic SEI which inevitably increase the cost and manufacturing difficulty.

A well-known example of applying ceramic SEI is to coat a thin, compact layer of Al<sub>2</sub>O<sub>3</sub> on Li *via* atomic layer deposition (ALD).<sup>346–348</sup> The process provides the possibility to control the thickness of Al<sub>2</sub>O<sub>3</sub> at sub-20 nm length scale, which is essential to achieve reasonable interfacial conductivity. The naturally insulating Al<sub>2</sub>O<sub>3</sub> can be lithiated upon the first few cycles and form a lithium ion conducting SEI, which exhibits the ability to suppress dendrite growth effectively. Since the film formed by ALD is homogeneous, it offers stability of lithium under ambient environment. The concept of deposition or sputtering can in principle be applied to other oxide or nitride materials

with a wide range of modulus and dielectric constants to construct optimal ceramic SEI.<sup>22,43</sup> It is worth noting that the exact working mechanism of a thin ceramic interphase is still under investigation, especially elucidating whether it can maintain the structural integrity under large volume expansion during the lithium electrodeposition.

While a pinhole-free ceramic SEI is intuitively necessary, it is difficult to achieve such precision with ceramic particles alone. Either spin coating Al<sub>2</sub>O<sub>3</sub> particles<sup>349</sup> or the approach method reported by Lu *et al.*<sup>250,350</sup> and Agarwal *et al.*<sup>351</sup> in which ionic-liquid or polymer grafted nanoparticles dispersed to an electrolyte migrate and deposit on the Li anode inside an electrochemical cell form a hybrid particle based interphase. As shown by Agarwal *et al.*, deliberate introduction of polydispersity by employing inorganic particles with different sizes is advantageous both for filling gaps and possibly for manipulating the length scale over which the electric field at the electrode decays into the fluid bulk. To further improve the mechanical robustness of the ASEI, ceramic/polymer composite can also be applied outside the battery cell using the solvent casting or the LB scooping approach to create the interphase on a water compatible metal, followed by drying and mechanical transfer to Li.<sup>336,352</sup> As a step to improve the conductivity of ceramic SEI, lithium ion conducting ceramics are investigated as well inspired by the solid-state electrolyte field. By selecting ceramic SSE that are stable against lithium, a thin layer of ceramic SSE can be coated on lithium that both serves as the dendrite inhibitor and ionic conductor.<sup>353–355</sup>

**3.2.4 Metallic and electronically conductive ASEI.** Metallic artificial SEI is not common but recently receives more attentions as they show promising performance to enable lithium metal anode. Typical approach to create metallic SEI is by ion exchange reaction, utilizing the high reactivity of lithium metal. For example, Sn, In, Zn, Al salts can readily react with lithium surface to form an alloy interphase. One benefit of metallic SEI comes from lowered interfacial resistance, originating from the structured interphase with a larger surface area than the planar lithium, as well as the high electric conductivity of the lithium alloy. For example, LiSn and LiIn can be created by a facile approach of reacting Sn/In salt in aprotic solvents and cast on lithium metal.<sup>272,356</sup> *Via* spontaneous ion-exchange reactions, a layer of lithium alloy particles can be coated homogeneously on the lithium surface. Such protected lithium anodes exhibit an order of magnitude higher exchange current and cycling stability in both symmetric and full cells with substantially extended cycling stability. The alloy interphase also provides an additional mechanism to store lithium ions. Similarly, LiAs, LiZn, LiBi were also found to improve the stability of lithium electrodeposition.<sup>357</sup> Metallic interphases are also able to tune the nucleation energy barrier for lithium deposition, as reported in recent literatures.<sup>358</sup> The authors show that depending on the metal chemistry, the deposition overpotential for Li can be manipulated over a surprisingly wide range. The discovery is interpreted in terms of relative facility with which Li nucleates on/in the metallic SEI, but may also reflect more fundamental chemical effects.<sup>359</sup> Complementary measurements of the Li exchange current density would be helpful in clarifying the underlying mechanisms.

A metallic SEI for Li fabricated using metals that do not themselves form a SEI is also of interest because such SEI provide opportunities for exploiting the epitaxy concepts discussed earlier in the review in the context of Zn and Al electrodes,<sup>15</sup> for directing electrodeposition of Li such that specific crystal facets (*e.g.* with low reactivity to the electrolyte or with enhanced tendency to grow in the plane of the electrode, as opposed to normal to the electrode).

### 3.3 Designing Li electrodes for achieving high reversibility

**3.3.1 Architectural designs for Li metal anodes.** The metallic Li anode technically has infinite volume changes as the anode itself is at hostless configuration, and it is well known that Li metal anodes undergo severe volume expansion which ranges from 2 to 5 folds after several charge/discharge cycles due to accumulation of passivation layers composed of dead Li.<sup>301</sup> These unregulated volume changes arise from inhomogeneous SEI layers at the anode/electrolyte interface which agitates Li transport between the electrodes during the battery cycling. Also, the magnitudes of the volume changes heavily depend on cycling parameters, especially on high charge current densities.<sup>301,360</sup> Recently, there are an increasing amount of works reported on 3D scaffolds/quasi-hosts for Li metal anodes to address the problems. Utilizing 3D architectural designs for the Li metal anodes provides quasi-hosting and facilitated local current distributions for Li migrations to be stably tolerated at high charge/discharge current densities. The designs ultimately help to regulate reversible Li migration and SEI preservation for Li metal anode as the 3D scaffolds provide physicochemical and mechanical support.<sup>361–363</sup> The application of 3D matrix in regulating Li growth is not limited to battery systems using liquid electrolytes. For example, a porous Li-ion conduction matrix can suppress the formation of Li dendrites at  $0.5 \text{ mA cm}^{-2}$  in solid-state electrolytes.<sup>364</sup> Coating the ion-conducting porous solid matrix with an electron conducting carbon layer, which results in an electron/ion dual conducting framework, can further enhance the performance at an elevated current density of  $1 \text{ mA cm}^{-2}$ .<sup>365</sup> The electron–ion dual conducting framework can also be fabricated by partially dealloying the Li–Mg alloy anode on a garnet type electrolyte.<sup>366,367</sup> As we will show later, analogous designing rules based on transport considerations apply to the development of Li anode framework in liquid electrolytes. The ion transport in a liquid electrolyte occurs *via* the flowable liquid phase that spans throughout the electrochemical cell, whereas the electron transport through the uncontrolled, porous electrodeposits is fragile. As a result, the Li metal framework in liquid electrolytes is made of electron conducting materials, *e.g.* metals or carbons.

**3.3.2 Hosting Li in metallic frameworks.** A growing body of work nonetheless indicates that structural and chemical modification of the Cu current collectors for the lithium metal anodes can have dramatic effects on the anode reversibility and cycle life. Mao and co-workers reported the atomic scale design of FCC Cu(100) current collector surface lattice for improving the binding interactions with the elemental Li which has BCC crystal structure with the (110) lattice planes.<sup>368</sup> The electrodeposition

of a metal on a dissimilar metal substrate is first encountered by underpotential deposition that occurs above the equilibrium potentials of forming one to two monolayers of Li, given that the interaction of Li to the substrate is stronger than that of the Li to Li interaction. Therefore, the crystal structure of the underpotential deposits is often determined by the crystal structure of the substrate surface. A corresponding crystallographic orientation of overpotential deposits also known as a bulk deposit of Li is then determined by the orientation of the underpotential deposits. To understand the interaction between the Cu current collector and Li based on their surface lattices, it is reported that the Cu(100) face is most suitable for obtaining lattice coincidence with the Li(110) face which is a most highly packed structure for the bulk Li.<sup>65,122</sup> This result is explained by performing the density functional theory (DFT) calculations based on the binding energies as a function of the number of Li monolayers on the specified Cu surfaces as well as nucleation overpotential analysis. The DFT results revealed that the electrodeposits of Li(110), both under/overpotential Li deposits, is observed for the Cu(100) whereas neither of Cu(111) nor (110) is preferred compared to Cu(100) due to a lower binding energy of Li on Cu(111) and Cu(110), and a smaller nucleation overpotential of Li is observed for the Cu(100) compare to that of Cu(111) which corresponds to the pristine Cu current collector. Thus, tuning the crystallographic surface of Cu current collector to Cu(100) enables achieving stable Li electrodeposition by facilitating the formation of the underpotential deposits of Li(110) which guides the bulk Li to grow in  $\langle 110 \rangle$  direction.<sup>368</sup>

The micro-compartmented Cu current collector arrays designed by Yang and co-workers allow direct lateral growth of Li dendrites that is in parallel to a separator, and this lateral growth of Li dendrites induced by the lateral electric field in compartmented micro holes helps to suppress internal short-circuit induced by Li dendrites that pierce through the separator by growing in perpendicular direction to the separator from a planar surface.<sup>369</sup> Unlike other common approaches that suppress and inhibit Li dendrite growth during the courses of Li migrations, the lateral growth of Li dendrite in the micro-compartmented spaces helps to retard internal short circuit which improves the battery safety in a cell level. The geometric size of the micro-patterned 3D Cu is set to yield an electroactive area ratio of  $\sim 1.06$  in which the planar Cu has the electroactive area ratio of 1. This electroactive area tells that the micro-patterned 3D Cu has the relatively same active area that is comparable to typical Cu current collector. The theoretical capacity of the micro-patterned Cu is approximately  $4.1 \text{ mA h cm}^{-2}$  with the electroactive ratio of 1.06 and a thickness of  $45 \text{ }\mu\text{m}$ ; however, there is additional weight and thickness that is introduced from the upper PI layer. The theoretical thickness of a planar Li foil with the capacity of  $4.1 \text{ mA h cm}^{-2}$  is  $19.88 \text{ }\mu\text{m}$ , and conventional Cu current collector has a thickness of  $8 \text{ }\mu\text{m}$ , resulting in total thickness of  $\sim 28 \text{ }\mu\text{m}$ . Despite the increased volume and weight of the micro-patterned 3D Cu, the simulation analysis reveals a 60% reduction in the Li dendrite protruding stress towards the separator. This approach helps to suppress Li dendrite proliferation towards the separator that retards electrode short

circuit and also improves the electrochemical performance of the Li metal; however, the overall energy density of the cell is reduced by introducing the thick micro-patterned 3D Cu in the anode. Moreover, 3D Cu current collectors with Cu micropillars that are slightly covered by ZnO *via* ALD process is investigated by Dasgupta and co-workers.<sup>370</sup> The Cu micropillars are designed in a way that the pillar distance is optimized with a fixed tortuosity of 1 by a finite elemental and experimental analysis. It is found that the geometrical factors, mainly the pillar diameters and pillar distances, affect Li electrodeposition in which too small sized pillars,  $<0.2\ \mu\text{m}$  in pillar diameter, induce Li to be deposited at the top of the pillar at which the current density is highest and too large sized pillars,  $>10\ \mu\text{m}$  in pillar diameter, induce Li to be deposited preferentially at the wall of pillars. Therefore, geometrical factors of the pillars are optimized and engineered at a fixed total pore volume such that the Li is preferentially deposited at the voids among the pillars. The  $2\ \mu\text{m}$  pillars with the  $5\ \mu\text{m}$  pillar spacing turned out to be the optimized values. The finite elemental analysis on the pillars shows that minimal strains are applied within the pressure of the cell as this value lies within the elastic limits of Cu. Thus, the pillars do not experience permanent deformation from the pressure in the cell. However, the highly localized strains from the tip of the pillars deform the separator that is in contact with the pillars. This would yield reduced local porosity of electrolyte exposure at the top surface of the pillars that reduces a local ionic flux, resulting in hindrance of Li electrodeposition. The suppressed electrodeposition and growth of Li at the tip of the pillars are beneficial to the cell system as the possibility of the internal short circuit of the cell is alleviated. The work is further conducted to apply ultrathin  $50\ \text{nm}$  ZnO on the  $2\ \mu\text{m}$  Cu micro pillars *via* ALD process that facilitates Li migration. This dual optimization of geometrical and physicochemical factors allows creating advanced Cu current collectors that improve the safety of the LiM batteries.

Cu current collector with a combination of macropores and nanopores have been reported by Yu and co-workers for Li metal anodes.<sup>371</sup> This macro/nanoporous Cu structure, which has the thickness of  $20\ \mu\text{m}$ , is obtained by the physical dealloying  $\text{Cu}_{30}\text{Zn}_{70}$  followed by chemical oxidation and thermal reduction. The purpose of the macropores in the Cu current collector is to provide physical cages/quasi-hosts for Li that lead to uniform Li nucleation and hinder the growth of Li dendrites. The dimensions for the macropores and the nanopores of the Cu current collector are  $0.5\ \mu\text{m}$  to  $3.5\ \mu\text{m}$  and  $200\ \text{nm}$ , respectively. The macropores are argued to serve as the “cages” for Li during the battery charging process in which they help to tolerate the volume changes, whereas the nanopores facilitate the local current density along with the Cu/electrolyte interface that widely distributes the access for Li to be electrodeposited. A heterogeneous distribution of pore sizes in the Cu current collector should improve the structure’s ability to alleviate volume changes during the cell cycling. Chen and co-workers explore such processes using electrochemical deposition process of Cu to modify the conventional Cu current collector.<sup>372</sup> The resultant 3D surface structure of Cu obtained was found to be comprised of interconnected  $50\ \text{nm}$  Cu nanoparticles with the porosity of 76%. This nanoporous structure appears to be

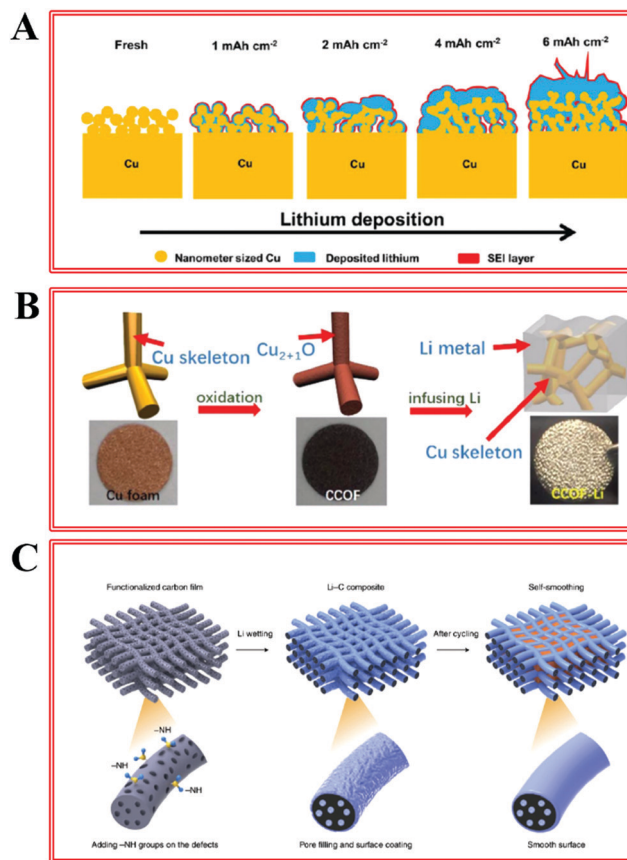


Fig. 23 Design of 3D architectures for Li metal anode. (A) Illustration for Li electrodeposition at nanoporous Cu current collector. Reprinted with permission from ref. 372. Copyright (2019) Elsevier. (B) Illustration for fabrication and structure of thermally infused Li on cuprite coated Cu foam. Reprinted with permission from ref. 373. Copyright (2019) Elsevier. (C) Illustration of fabrication steps for amine functionalized self-smoothing mesoporous carbon fibers. Reprinted with permission from ref. 382. Copyright (2019) Springer Nature.

highly effective in limiting Li dendrite formation as illustrated in Fig. 23A. Relatively smooth Li electrodeposits are achieved for the Li capacity and charging density of 2 to 6 mA h cm<sup>-2</sup> and 4 to 12 mA cm<sup>-2</sup>, respectively.

Metallic foams of Cu, Ni, and Ti have recently resurfaced as fundamental tools for regulating Li electrodeposition. These materials have been reported to be particularly advantageous when they are modified by chemical treatment. For instance, cuprite ( $\text{Cu}_2\text{O}$ ) coated Cu foams (Fig. 23B)<sup>373</sup> have been synthesized to prestore Li and shown to enhance lateral growth of Li during the cell charging process. The 3D structure of Cu skeleton helps to distribute the charges that improve electrochemical reversibility of Li deposition/dissolution process, and the cuprite coating, which has high interactions with Li, on the Cu 3D skeleton further improves stable nucleation of Li and allows thermal infusion of molten Li. The Cu foam has the thickness of  $50\ \mu\text{m}$  with the cuprite coating layer thickness of  $110\ \text{nm}$ . Despite the thickness of the cuprite coated 3D Cu exceeds the conventional Cu current collector, the reversibility of the Li metal electrode improved by a factor of almost two. Cu

nanowires synthesized at the surface of 3D Cu foam have also been explored as substrates capable of improve hosting of Li in Cu *via* a thermal infusion mechanism.<sup>374</sup> The high surface energy and the capillary forces of Cu nanowires at the surface of 3D Cu facilitate interactions with Li such that the infusion of molten Li is in complete occupation of the voids in the 3D Cu foam. Interestingly, it is found that the exterior surface of the Cu nanowire coated Cu foam exhibits Cu–Li alloy crystallites due to the thermal infusion of Li that causes the reaction between Cu and Li. Throughout the surface nanoengineering, interaction of Cu with Li is largely improved, and the reversibility of the Li migration is extended even at high current densities. Zhou and co-workers have introduced 3D CoO nanofiber coated Ni foam framework for anode in a similar manner for modifying 3D Cu skeletons.<sup>375</sup> Despite a heavier weight of Ni than Cu, the interaction of Li with Ni is stronger than that of with Cu. Thus, molten Li can be thermally diffuse throughout the Ni skeletons, and the modification of the 3D Ni network surfaces with CoO nanofibers further enhances the thermal diffusion rate that the molten Li is infused fully to the 3D Ni within 5 seconds. Furthermore, the CoO nanowire coated 3D Ni with Li composite is able to tolerate a high current density of  $6 \text{ mA cm}^{-2}$  and also applicable to elemental sulfur and  $\text{Ni}_{0.8}\text{Co}_{0.15}\text{Al}_{0.05}\text{O}_2$  cathodes. The advantage of having Ni and CuO double layer structure as Li quasi-host is that the growth of Li triggers “bottom-up” Li deposition pathway and also distributes the local current densities along with the double layer surfaces, which improves reversibility of Li migration. More sophisticated modification has been done on 3D Ti mesh with dual layers of carbon and CuO nanolayers by Wang and co-workers.<sup>376</sup> The 3D Ti mesh with the pore size of  $100 \mu\text{m}$  is chosen in this study due to its good electrical conductivity, chemical inertness, high strength, and high toughness to withstand the internal stress exerted from the volume changes of Li metal. The mesh is further modified with CuO nanoflowers on top of carbon/Ti substrate that can distribute local current densities and uniform electric fields for allowing stable Li migration process for Li metal. The resulting outcome is that the reversibility of Li migration is improved by an order of magnitude by comparing the performance with planar Cu current collector. So the nanoengineering the surface of metallic 3D current collectors improve the reversibility of Li plating/dissolution cycles which yields prolonged cycle life of LiM batteries. Halogenide modified 3D Cu foam is also done by Wan and co-workers. The CuBr- and Br-doped graphene-like film modified Cu foam current collector<sup>377</sup> provides synergistic effect as the Br doped sites on graphene helps to regulate uniform Li ion flux and nucleation as well as the reaction between CuBr and Li generates LiBr to induce pancake-like nucleation seeds that stabilize the Li growth. This chemical modification followed by the 3D network yields 10 folds improvement on reversibility of Li migration even at high current density and capacity. Therefore, these diverse ways to modify the metallic 3D current collectors brings many solutions to overcome with volume changes and low reversibility for Li metals.

The coupling the degrees of the Li interaction with the current collectors and 3D network structures can also resolve the low reversibility of Li migrations as well as low safety issues for Li metals. Zhang and co-workers developed a deposition-regulating strategy by creating electrochemical interaction gradient of Li with the 3D Ni current collector to induce preferential deposition and growth of Li at the bottom surface of the anode that is the away side of the separator.<sup>378</sup> In order to prevent internal short-circuit, it is crucial to control the electro-deposition of Li at the anode/separator interface, which is termed as the top-growth mode. In often cases for conducting metallic anodes, the top growth of Li is preferred as the top surface facing the separator side is most exposed to electric field gradients. Thus, creating electrical passivation layer at the anode/separator interface would reduce this phenomenon; however, the interaction of Li must be strong for an underneath the passivation layer to facilitate stable Li migration. 3D Ni foam has been modified in a way that the interaction of Li with the deposition substrate is strongest from the distance away from the anode/separator interface. This gradient is achieved in 3D structure by coating highly yet stably interacting metal of Au with Li at the bottom of the 3D Ni foam and by coating electrically insulating  $\text{Al}_2\text{O}_3$  ceramic layer at the top of the 3D Ni foam. These modifications help the 3D Ni foam to tune the nucleation thermodynamics that allow Li to preferentially be coated at the bottom of the 3D Ni, and also the interconnected pores of the 3D Ni foam facilitates Li ion transport by conductive 3D networks that allow high reversibility of Li migration at high current density of  $10 \text{ mA cm}^{-2}$  and even at low temperature  $-15 \text{ }^\circ\text{C}$ . Instead of tuning the Li reactivity of 3D metallic surfaces, Yang and co-workers developed conductive-dielectric gradient network composed of melamine sponge and Ni nanolayer that induce “bottom-up” electrodeposition of Li and “top-down” dissolution of Li during the Li migration process for Li metals.<sup>379</sup> The electrically conductive Ni layers at the bottom of the dielectric melamine sponge help to preferentially nucleate Li at the bottom first. Also, the thickness of Ni layers is thickest at the bottom and gradually reduces to the center of the melamine sponge so that the Li can grow upward during the electrodeposition process. The dielectric portion of the melamine sponge helps to stabilize the Li ion flux and distribution by containing highly polar amine group that can adsorb  $\text{Li}^+$ . Supported by these features, the 3D network of the conductive–dielectric sponge guides to uniform and dendrite-free Li regulation that enhances the reversibility of the Li migration. In a similar fashion, Guo and co-workers have fabricated lithiophobic (Cu)–lithiophilic (Zn or Sn) 3D composite for Li metal.<sup>380</sup>

Cu foam and  $\text{Zn/Cu}_{0.7}\text{Zn}_{0.3}/\text{Cu}$  foam current collectors are compared for Li deposition and growth processes. As the Cu has low reactivity of Li, Cu is regarded as the lithiophobic phase where the conductive 3D network created by the Cu foam helps to distribute electric fields for Li deposition. The lithiophilic phase of  $\text{Zn/Cu}_{0.7}\text{Zn}_{0.3}$  helps to reduce nucleation overpotential of Li substantially the suppresses the Li dendrite growth. Furthermore, Ni foam that is decorated with  $\text{Li}_3\text{N}$  *via* plasma

nitriding and thermal infusion of Li process is introduced by Sun and co-workers.<sup>381</sup> High specific surface area and uniform coverage of Ni<sub>x</sub>N ( $x = 3$  or  $4$ ) for 3D Ni foam are first derived by the plasma process. Due to high surface area and lithiphilicity of Ni<sub>x</sub>N, thermal infusion of molten Li chemically reacts with the plasma nitriding 3D Ni foam to generate Li<sub>3</sub>N and Ni, which are lithiphilic. By combining the 3D Ni network and the nitride layer, stable Li migration is achieved especially due to the homogeneous nucleation offered by Li<sub>3</sub>N which has high binding energy and conductivity of Li. All of these architecturing and tuning the surface interactions with Li stabilize Li migration for high energy Li metal to achieve highly reversibility at relatively high charging current densities.

**3.3.3 Hosting Li in carbon frameworks.** Because of their conceptual similarity to the ionic hosting strategy perfected in the graphite anode in Li-ion batteries, a potentially important but insufficiently used criterion for evaluating the practical benefits of these approaches is how the overall specific capacity of the hosted Li anode compares to that of the graphite anode used in LiBs. In this regard, a perhaps obvious and quite serious drawback of utilizing metals as non-planar hosts for Li is therefore the decrease of the energy density of the cell due to heavyweight carried by Cu, Ni, and Ti. Despite 3D metallic current collectors provide facilitated Li ion flux distributions and reversible Li migration, there is a great energy reduction cost by adapting these heavyweight current collectors. It is, however, preferable to develop Li quasi-host materials that are carbon mainly due to their lightweight. As Li metal obeys electroplating process, it is known that porous carbon structures are beneficial in this respect point of use. Liu and co-workers developed self-smoothing Li metal quasi host that is composed of amine functionalized mesoporous carbon in 3D structure.<sup>382</sup> In Fig. 23C, the amine groups on the defect of the mesoporous carbon fibers trigger facilitated diffusion of molten Li that completely fills the pores of the carbon fibers as wells the interconnected 3D structures. The key to this phenomenon is the amine functionalization of the mesoporous carbon. As the pores or cavities in the carbon interact strongly with Li, the subsequent Li deposition becomes stable and formation a thick Li layer that evenly gets distributed along with the whole architecture of the anode.

Another potentially important approach uses a g-C<sub>3</sub>N<sub>4</sub> interlayer on top of the carbon cloths developed by Kang and co-workers.<sup>383</sup> The interesting result is that Li is electrodeposited in between the carbon cloth and g-C<sub>3</sub>N<sub>4</sub>. The high lithiphilic feature of g-C<sub>3</sub>N<sub>4</sub> promotes facilitated Li ion distribution along with the carbon clothes surfaces, and this regulates stable Li migration to suppress dendritic Li electrodepositions. Zheng *et al.* used bare carbon cloth<sup>44</sup> as a model framework that provides nonplanar, interpenetrated electron transport pathways<sup>384</sup> to interrogate the Li electrodeposition morphology and its correlation with the plating/stripping reversibility. The results show that, embedded in the open space among the carbon fibers, Li maintains its obviously dendritic growth pattern (Fig. 24) in the representative electrolyte, *i.e.* 1 M LiPF<sub>6</sub> in EC/DMC, 1 M LiPF<sub>6</sub> in 10% FEC-EC/DMC and 1 M LiTFSI in

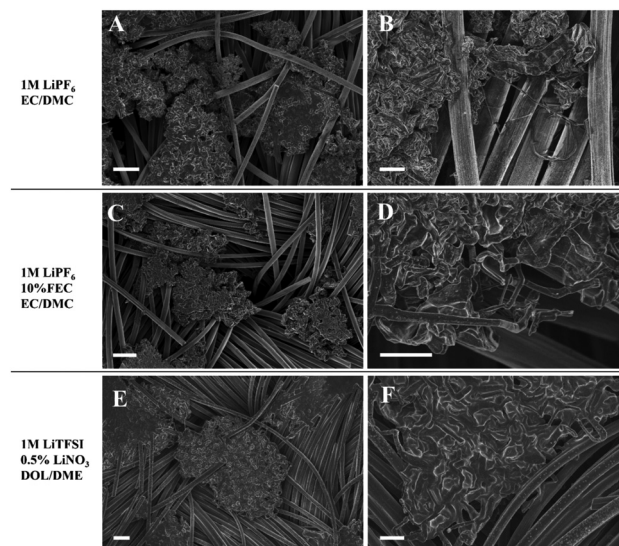


Fig. 24 Li deposition morphology in a non-planar electrode. SEM images of Li deposits in (a and b) 1 M LiPF<sub>6</sub> in EC/DMC, (c and d) 1 M LiPF<sub>6</sub> in 10 w% FEC-EC/DMC and (e and f) 1 M LiTFSI + 0.5% LiNO<sub>3</sub> in DOL/DME. Scale bars: left (a, c and e) 40 μm; right (b, d and f) 10 μm. Reprinted with permission from ref. 44. Copyright (2019) American Chemical Society.

0.5% LiNO<sub>3</sub>. It is surprising that, a high level of Li plating/stripping Coulombic efficiency, *i.e.* >99.4% is achievable with these dendritic Li electrodeposits. The finding underscores the decisive role of robust electron transport in stabilizing Li metal plating/stripping. Once the electron transport length scale is kept below a certain threshold, *e.g.* 5 μm in this case, the irreversibility caused by physical disconnection of the Li deposits can be readily suppressed. We also note that, the remaining ~0.6% Coulombic inefficiency is attributable to the chemical instability, *i.e.* the propensity for undergoing side reactions, which could be mitigated by designing a more chemically stable electrolyte as suggested in Section 3.1.

To close, we note that the additional mass and volume introduced by the host architectures must be scrutinized carefully even in basic research studies to limit the number of ultimately unfruitful directions defined by these studies. This issue can of course be examined quantitatively as is done in Fig. 25. Assuming the Li metal anode has an areal capacity of 3 mA h cm<sup>-2</sup>, which is the conventional areal capacity of Li-ion cathodes: the mass of the Li anode is 1.54 mg cm<sup>-2</sup>, and the thickness is 15 μm, it is possible to estimate the influence of the additional hosting architecture. Fig. 25A for example summarizes the decrease of gravimetric specific capacity promised by the Li metal chemistry as the mass of the architecture increases. Preferably, the mass of the host architecture should be reduced to below 0.2 mg cm<sup>-2</sup> in order to achieve a >3000 mA h g<sup>-1</sup> capacity. As the mass of the host architecture reaches 2 mg cm<sup>-2</sup>, the Li metal chemistry shows no superiority to Sn or metal oxides. Ultimately, any architecture that has an areal mass over 6 mg cm<sup>-2</sup> is hardly competitive with commercial Li-ion anodes. As a rough comparison, the areal mass of a 3D metal foam is around 5–10 mg cm<sup>-2</sup>, depending on the

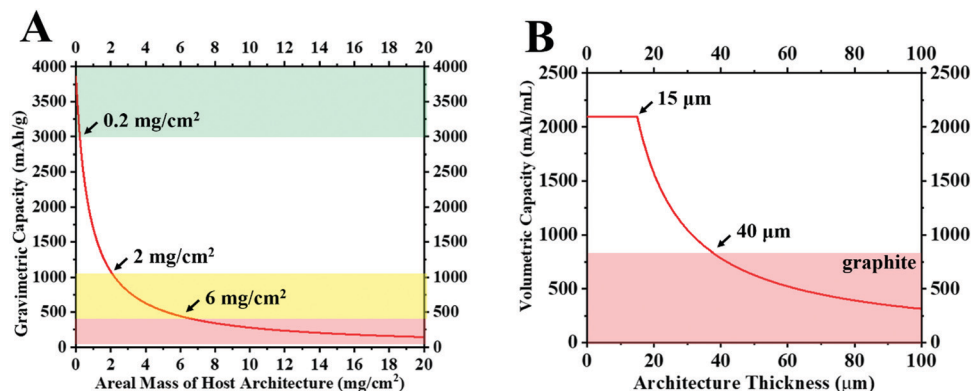


Fig. 25 Overall specific capacity achieved by Li metal anodes with “host” architectures. (A) Dependence of gravimetric specific capacity of Li metal anode on the areal mass of host architecture. (B) Dependence of volumetric capacity of Li metal anode on the thickness of host architecture.

chemistry and the porosity. This additional mass will inevitably diminish the overall gravimetric capacity in a nontrivial manner. Fig. 25B illustrate the variation of volumetric capacity over architecture thickness. To simplify the calculation, it is assumed that the electrode thickness equals to the architecture thickness. An architecture thicker than 15 µm adds extra thickness to the electrode, and therefore reduces the volumetric capacity. The plot suggests that the thickness of the architecture should be limited to below 40 µm, and preferably to 15–20 µm. These analyses based on simplified models render guiding principles for future designs of Li hosting frameworks that aim to demonstrate commercial relevance. It is noteworthy that same rules apply to other approaches for regulating Li metal growth – the additional mass/volume can be, likewise, introduced by electrolyte additive, Li coating, thicker battery separators, *etc.* The tempting high performance of the Li metal chemistry can be significantly compromised and decay to a state inferior even to graphite.

## 4. Perspectives and conclusion

Regulating Li metal plating/stripping as a science question has attracted massive, multidisciplinary research efforts. We witnessed a progressively comprehensive accumulation of knowledge on multiple facets about the fundamental principles governing Li electrodeposition. Nonetheless, we note that the understanding of the physics in Li electrodeposition remains inconclusive. These ambiguities center around two main relations. First, the relation between deposition conditions (*e.g.* electrolyte chemistry, current density, substrate, *etc.* as outlined in Section 2) and the resultant deposition morphology. For example, it is recently revealed by *operando* optical microscopy that the pitting of Li foil in stripping process can create geometric heterogeneities; Li nucleation and growth in the next cycle preferentially occur on the edges of the holes formed in the pitting.<sup>47</sup> This effect of “stripped” landscape on the deposition morphology could be significant, but was largely overlooked previously. Despite of the large body of literature discussing possible factors dominating Li metal electrodeposition morphology, the search for the decisive origin(s) behind the many growth patterns of Li is an ongoing process. The grand question

for Li, in our view, is—what determines the electrodeposition morphology of Li.

In the second place, the relation between Li deposition morphology and the resultant plating/stripping reversibility is unclear. The generic expectation is that a compact, flat Li deposit is able to show unprecedentedly high level of reversibility. However, for example, the plating/stripping CE of columnar Li that has a relatively compact morphology is not satisfactory, *e.g.* ~80%,<sup>385</sup> 98.7%.<sup>386</sup> By contrast, obviously dendritic Li deposits embedded in a nonplanar substrate manifest a >99.4% CE.<sup>44</sup> These observations lead to the second question—how the morphology of Li influences its plating/stripping reversibility.

The first question, *i.e.* the mystery of Li growth patterns, could potentially be fully answered by *in situ* analytical TEM under cryogenic conditions. Together with high resolution imaging, the many functions of an analytical TEM, including electron diffraction, electron energy loss spectroscopy can provide the crystallographic and the chemical information about local Li structures at multiple length scales of interest (nm–µm). Particularly, if the observation is conducted *in situ*, the structural evolution at different stages can be fully captured. This type of observation is made possible by the cryogenic method, which makes sure no artifacts are generated during sample preparation or observation. As a result, investigations utilizing cryo-TEM into Li plating/stripping are generating revealing insights, and are arousing rapidly growing dedication.

To answer the second question, *i.e.* the relation between morphology and reversibility, more standardized evaluation and description of the observed Li morphology under microscope emerges as a prerequisite. In a classical electrodeposition context, “dendritic” structures result from mass transport limit. The misuse of dendrite in calling the irregular Li electrodeposits without a reliable identification of its nature causes much unnecessary confusion. As clearly shown by Bai *et al.*,<sup>84</sup> diffusion-limit-induced Li dendrites are initiated above the limiting current at the Sand’s time; otherwise, the irregular Li is referred to as mossy. It is also noteworthy that the use of “dendrite-free” underwent an exponential escalation: 14, 25, 55, 144, 221 papers were published with “dendrite-free” in their titles, from 2015

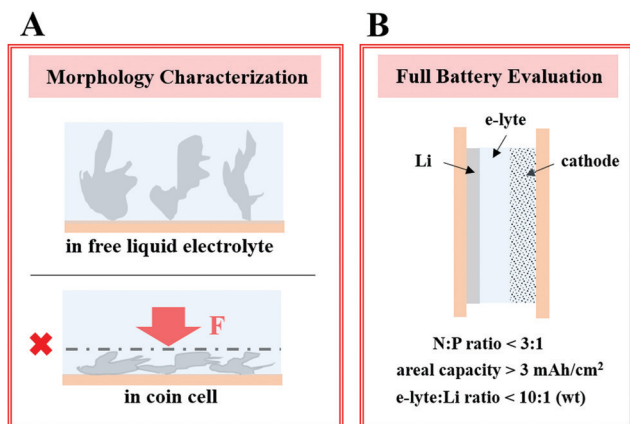


Fig. 26 Rationalized characterization and evaluation of Li metal anode. (A) Illustration showing the influence of pressure in coin cell on Li electrodeposition morphology. (B) Illustration showing the requirements for a meaningful full battery evaluation of Li metal anode.

to 2019, respectively (according to Web of Science database). In most of the papers, the use of “dendrite-free” is justified by SEM micrograph of Li electrodeposition performed in coin cell, where the internal pressure is large. As discussed previously, the presence of pressure can significantly change the Li morphology *via* mechanical forces (Fig. 18B).<sup>228</sup> With this predominant influence from local pressure, other factors' contributions could turn out to be obscured and show negligible effect on the Li morphology. To evaluate the genuine effect of a strategy on Li electrodeposition, it is highly recommended that the electrodeposition be carried out using more classical analytical apparatus to rule out the effect of pressure (Fig. 26A). For example, a very early study on electrokinetics of Li was based on a rotating-disk electrode.<sup>97</sup> The electron microscopy observation at multiple magnifications of the Li deposits obtained under the condition specified above is able to reveal the authentic Li landscape. By coupling the Li morphology with electrochemical plating/stripping efficiency test, this second question can be answered.

Understanding Li electrodeposition relies on responding to the basic science questions, *e.g.* the two discussed above, whereas building commercially viable Li metal anode is an engineering issue. Based on the current knowledge, it is clear that Li deposition is influenced by many factors, physical (mass transport, mechanical forces, *etc.*), chemical (crystal anisotropy, SEI formation, *etc.*) and even technical (substrate surface impurity, *etc.*). From an engineering perspective, concerted effort from multiple strategies is required in maximizing the capability of a certain system. It is recently shown for Na anode, by tuning the “often-neglected” parameters, up to 99.96% plating/stripping efficiency is achieved for over 500 cycles in a commercial electrolyte.<sup>387</sup>

The ultimate target of developing Li metal anodes is to build commercially viable full batteries that outperform Li-ion batteries. Simply using Li metal as the anode will not guarantee the superiority over Li-ion batteries in terms of energy density; instead, multiple technical parameters need to be strictly controlled

(Fig. 26B). Full battery tests without paying specific attention to these parameters could generate superficially excellent cycling performance of little practical interest. To critically assess the performance of Li metal full batteries—First, the amount of Li stored in the anode should be limited (Fig. 2A).<sup>384,388</sup> The full battery experiment where the amount Li is not controlled, *i.e.* the N:P ratio is higher than 3:1, will be of less value in assessing its practicability. It is hence suggested that the N:P ratio be included as a crucial experimental parameter for future full battery evaluation of Li metal anode. Areal capacity is another electrode parameter that directly affects the resulting overall energy density. The relative weight from components including separator, electrode current collector, electrolyte, *etc.*, increases as areal capacity decreases. The state-of-the-art Li-ion electrode has an areal capacity of 3–4 mA h cm<sup>-2</sup>.<sup>389</sup> However, in Li metal full battery tests reported, cathode areal capacities lower than 0.5 mA h cm<sup>-2</sup> (or <3–5 mg cm<sup>-2</sup> loading, depending on cathode chemistry) are often seen. Since the morphology/volume change associated with the Li metal electrode is much smaller in such cases, the cycling performance obtained is less informative in terms of viability of the Li metal anode. Furthermore, the electrolyte to Li mass ratio similarly strongly influences the resulting energy density.<sup>384</sup> However, the continuous consumption of electrolyte due to side reactions leads to battery failure.<sup>390</sup> As a result, excess amount of electrolyte is sometimes added. For example, for coin cell (CR2032) experiments reported recently, 60  $\mu$ L is common value, which weighs around 50 mg cm<sup>-2</sup>; in a Li||LCO battery, assuming an areal capacity of 3 mA h cm<sup>-2</sup> and an N:P ratio of 3:1, the mass of Li anode and the cathode are 3 and 20 mg cm<sup>-2</sup>, respectively. This leads to an unrealistic Li: electrolyte ratio, where electrolyte accounts for the majority of the overall mass. In such cases, the electrolyte consumption issue can not be critically evaluated. If a 350 W h kg<sup>-1</sup> energy density goal is to be achieved, the maximum electrolyte amount per cell capacity is 3 mg mA<sup>-1</sup> h<sup>-1</sup>.<sup>391</sup> Therefore, it is recommended that these three crucial parameters, *i.e.* N:P ratio, areal capacity and electrolyte:Li ratio, be reported in future studies on Li metal full battery performance. Finally, we notice that most Li anode cycling experiments were performed in coin-type cells, while pouch-type cells are more relevant to commercialization. The powdering of Li metal has been reported to be a more prominent issue of pouch-type Li metal batteries than in coin-type cells.<sup>392,393</sup> This indicates that new issues could emerge as one transitions from coin-type cells to pouch-type cells.

In conclusion, Li metal electrodeposition is a topic that is both of considerable application value and of vast scientific interest. The crucial role battery systems are playing in the whole green energy industry stimulates the reviving trend of research about Li metal anode. It is the complicated nature of Li electrodeposition in battery anode that triggered a multi-disciplinary scrutiny, the results of which greatly enrich the fundamental knowledge of electrochemistry, *e.g.* the role of an SEI. It is expected that the puzzles of Li electrodeposition can be resolved in the future by advanced characterization techniques. From the application aspect, the current plateauing trend of Li metal anodes' electrochemical performance at a point that is not

of commercial viability is gradually taking shape, despite of the exponential growth of the usage of “dendrite-free” in the literature. It indicates that transformative breakthroughs are urgently needed. This type of breakthroughs could emerge from the fundamental scientific advancement in understanding Li electrodeposition, creating Li-specific solutions, since Li metal's electrochemical behaviors, possibly owing to its high chemical reactivity and low electrochemical potential as an alkali metal, are distinct from classical metal electrodeposition systems, e.g. Cu and Zn.

## Conflicts of interest

Prof. Lynden A. Archer is a founder and member of the board of directors of NOHMs Technologies. This company develops and commercializes electrolytes for Li-ion and Li-sulfur battery technology. The authors declare no other competing interests.

## Acknowledgements

This work was supported as part of the Center for Mesoscale Transport Properties, an Energy Frontier Research Center supported by the U.S. Department of Energy, Office of Science, Basic Energy Sciences, under award #DE-SC0012673. Support from the Department of Energy Basic Energy Science, Synthesis and Processing Science Program, through award # DE-SC0016082, is also gratefully acknowledged. The authors express their gratitude to Dr Qing Zhao, Prof. Xiangzhong Ren, Shuo Jin and Dr Ruichun Luo for valuable discussions.

## References

- 1 A. Volta, *Philos. Trans. R. Soc. London*, 1800, **90**, 403–431, DOI: 10.1098/rstl.1800.0018.
- 2 G. De Santillana, *Sci. Am.*, 1965, **212**, 82–91.
- 3 E. S. Takeuchi and R. A. Leising, *MRS Bull.*, 2002, **27**, 624–627.
- 4 C. A. Aubin, S. Choudhury, R. Jerch, L. A. Archer, J. H. Pikul and R. F. Shepherd, *Nature*, 2019, **571**, 51–57.
- 5 B. Nykvist and M. Nilsson, *Nat. Clim. Change*, 2015, **5**, 329.
- 6 M. Ishikawa, M. Kanemoto and M. Morita, *J. Power Sources*, 1999, **81**, 217–220.
- 7 S. Shafiee and E. Topal, *Energy Policy*, 2009, **37**, 181–189.
- 8 R. J. Andres, T. A. Boden, F. M. Bréon, P. Ciais, S. Davis, D. Erickson, J. S. Gregg, A. Jacobson, G. Marland and J. Miller, *Biogeosciences*, 2012, **9**, 1845–1871.
- 9 S. Solomon, G.-K. Plattner, R. Knutti and P. Friedlingstein, *Proc. Natl. Acad. Sci. U. S. A.*, 2009, **106**, 1704–1709.
- 10 S. J. Davis, K. Caldeira and H. D. Matthews, *Science*, 2010, **329**, 1330–1333.
- 11 U. S. E. I. Administration, 2019.
- 12 J. Xu, Y. Chen and L. Dai, *Nat. Commun.*, 2015, **6**, 8103.
- 13 Y.-M. Chiang, L. Su, M. S. Pan and Z. Li, *Joule*, 2017, **1**, 212–219.
- 14 O. Schmidt, S. Melchior, A. Hawkes and I. Staffell, *Joule*, 2019, **3**, 81–100.
- 15 J. Zheng, Q. Zhao, T. Tang, J. Yin, C. D. Quilty, G. D. Renderos, X. Liu, Y. Deng, L. Wang, D. C. Bock, C. Jaye, D. Zhang, E. S. Takeuchi, K. J. Takeuchi, A. C. Marschilok and L. A. Archer, *Science*, 2019, **366**, 645–649.
- 16 M.-C. Lin, M. Gong, B. Lu, Y. Wu, D.-Y. Wang, M. Guan, M. Angell, C. Chen, J. Yang and B.-J. Hwang, *Nature*, 2015, **520**, 324.
- 17 M. S. Whittingham, *Science*, 1976, **192**, 1126–1127.
- 18 K. Mizushima, P. C. Jones, P. J. Wiseman and J. B. Goodenough, *Mater. Res. Bull.*, 1980, **15**, 783–789.
- 19 A. Yoshino, *Angew. Chem., Int. Ed.*, 2012, **51**, 5798–5800.
- 20 D. Lin, Y. Liu and Y. Cui, *Nat. Nanotechnol.*, 2017, **12**, 194–206.
- 21 J. Qian, B. D. Adams, J. Zheng, W. Xu, W. A. Henderson, J. Wang, M. E. Bowden, S. Xu, J. Hu and J. G. Zhang, *Adv. Funct. Mater.*, 2016, **26**, 7094–7102.
- 22 Z. Tu, M. J. Zachman, S. Choudhury, K. A. Khan, Q. Zhao, L. F. Kourkoutis and L. A. Archer, *Chem. Mater.*, 2018, **30**, 5655–5662.
- 23 Z. W. Seh, J. Sun, Y. Sun and Y. Cui, *ACS Cent. Sci.*, 2015, **1**, 449–455.
- 24 M. Rosso, C. Brissot, A. Teyssot, M. Dollé, L. Sannier, J.-M. Tarascon, R. Bouchet and S. Lascaud, *Electrochim. Acta*, 2006, **51**, 5334–5340.
- 25 H. Wu, D. Zhuo, D. Kong and Y. Cui, *Nat. Commun.*, 2014, **5**, 1–6.
- 26 B. Wu, J. Lochala, T. Taverne and J. Xiao, *Nano Energy*, 2017, **40**, 34–41.
- 27 A. Gupta, E. Kazayak, N. Craig, J. Christensen, N. P. Dasgupta and J. Sakamoto, *J. Electrochem. Soc.*, 2018, **165**, A2801–A2806.
- 28 K. Liu, Y. Liu, D. Lin, A. Pei and Y. Cui, *Sci. Adv.*, 2018, **4**, eaas9820.
- 29 R. Spotnitz and J. Franklin, *J. Power Sources*, 2003, **113**, 81–100.
- 30 E. P. Roth and C. J. Orendorff, *Electrochem. Soc. Interface*, 2012, **21**, 45–49.
- 31 Q. Wang, P. Ping, X. Zhao, G. Chu, J. Sun and C. Chen, *J. Power Sources*, 2012, **208**, 210–224.
- 32 R. Zhang, X. Shen, X.-B. Cheng and Q. Zhang, *Energy Storage Mater.*, 2019, **23**, 556–565.
- 33 A. Schiele, B. Breitung, T. Hatsukade, B. Z. B. Berkes, P. Hartmann, J. R. Janek and T. Brezesinski, *ACS Energy Lett.*, 2017, **2**, 2228–2233.
- 34 T. Waldmann, B.-I. Hogg and M. Wohlfahrt-Mehrens, *J. Power Sources*, 2018, **384**, 107–124.
- 35 C. Uhlmann, J. Illig, M. Ender, R. Schuster and E. Ivers-Tiffée, *J. Power Sources*, 2015, **279**, 428–438.
- 36 L. E. Downie, L. J. Krause, J. C. Burns, L. D. Jensen, V. L. Chevrier and J. R. Dahn, *J. Electrochem. Soc.*, 2013, **160**, A588–A594.
- 37 D. Ren, H. Hsu, R. Li, X. Feng, D. Guo, X. Han, L. Lu, X. He, S. Gao and J. Hou, *eTransportation*, 2019, **2**, 100034.
- 38 T. Waldmann, M. Kasper and M. Wohlfahrt-Mehrens, *Electrochim. Acta*, 2015, **178**, 525–532.

- 39 R. V. Bugga and M. C. Smart, *ECS Trans.*, 2010, **25**, 241–252.
- 40 C. von Lüders, V. Zinth, S. V. Erhard, P. J. Osswald, M. Hofmann, R. Gilles and A. Jossen, *J. Power Sources*, 2017, **342**, 17–23.
- 41 W. Lu, C. M. López, N. Liu, J. T. Vaughey and A. Jansen, *J. Electrochem. Soc.*, 2012, **159**, A566–A570.
- 42 X.-G. Yang, Y. Leng, G. Zhang, S. Ge and C.-Y. Wang, *J. Power Sources*, 2017, **360**, 28–40.
- 43 S. Xu, K.-H. Chen, N. P. Dasgupta, J. B. Siegel and A. G. Stefanopoulou, *J. Electrochem. Soc.*, 2019, **166**, A3456–A3463.
- 44 J. Zheng, T. Tang, Q. Zhao, X. Liu, Y. Deng and L. A. Archer, *ACS Energy Lett.*, 2019, **4**(6), 1349–1355.
- 45 K.-H. Chen, K. N. Wood, E. Kazyak, W. S. LePage, A. L. Davis, A. J. Sanchez and N. P. Dasgupta, *J. Mater. Chem. A*, 2017, **5**, 11671–11681.
- 46 R. Zhu, C. Liu, J. Feng and Z. Guo, *ECS Trans.*, 2018, **85**, 347–356.
- 47 A. J. Sanchez, E. Kazyak, Y. Chen, K.-H. Chen, E. R. Pattison and N. P. Dasgupta, *ACS Energy Lett.*, 2020, **5**, 994–1004.
- 48 Y. Deng, J. Zheng, A. Warren, J. Yin, S. Choudhury, P. Biswal, D. Zhang and L. A. Archer, *Adv. Energy Mater.*, 2019, **9**, 1901651, DOI: 10.1002/aenm.201901651.
- 49 J.-H. Cheng, A. A. Assegie, C.-J. Huang, M.-H. Lin, A. M. Tripathi, C.-C. Wang, M.-T. Tang, Y.-F. Song, W.-N. Su and B. J. Hwang, *J. Phys. Chem. C*, 2017, **121**, 7761–7766.
- 50 C. Fang, J. Li, M. Zhang, Y. Zhang, F. Yang, J. Z. Lee, M.-H. Lee, J. Alvarado, M. A. Schroeder and Y. Yang, *Nature*, 2019, **572**, 511–515.
- 51 K. S. Nagy, S. Kazemiabnavi, K. Thornton and D. J. Siegel, *ACS Appl. Mater. Interfaces*, 2019, **11**, 7954–7964.
- 52 D. A. Cogswell, *Phys. Rev. E: Stat., Nonlinear, Soft Matter Phys.*, 2015, **92**, 011301.
- 53 R. Glocker and E. Kaupp, *Z. Phys.*, 1924, **24**, 121–139.
- 54 R. Sato, *J. Electrochem. Soc.*, 1959, **106**, 206–211.
- 55 N. A. Pangarov, *J. Electroanal. Chem.*, 1959, **1965**(9), 70–85.
- 56 J. W. Faust Jr, *J. Cryst. Grow.*, 1968, **3**, 433–435.
- 57 J. K. Stark, Y. Ding and P. A. Kohl, *J. Electrochem. Soc.*, 2013, **160**, D337–D342.
- 58 F. Shi, A. Pei, A. Vailionis, J. Xie, B. Liu, J. Zhao, Y. Gong and Y. Cui, *Proc. Natl. Acad. Sci. U. S. A.*, 2017, **114**, 12138–12143.
- 59 X. Wang, Y. Li and Y. S. Meng, *Joule*, 2018, **2**, 2225–2234.
- 60 Z. Zeng, W.-I. Liang, H.-G. Liao, H. L. Xin, Y.-H. Chu and H. Zheng, *Nano Lett.*, 2014, **14**, 1745–1750.
- 61 X. H. Liu, L. Zhong, L. Q. Zhang, A. Kushima, S. X. Mao, J. Li, Z. Z. Ye, J. P. Sullivan and J. Y. Huang, *Appl. Phys. Lett.*, 2011, **98**, 183107.
- 62 M. J. Zachman, J. A. Hachtel, J. C. Idrobo and M. Chi, *Angew. Chem.*, 2020, **132**, 1400–1412.
- 63 X. Wang, M. Zhang, J. Alvarado, S. Wang, M. Sina, B. Lu, J. Bouwer, W. Xu, J. Xiao and J.-G. Zhang, *Nano Lett.*, 2017, **17**, 7606–7612.
- 64 X. Wang, G. Pawar, Y. Li, X. Ren, M. Zhang, B. Lu, A. Banerjee, P. Liu, E. J. Dufek and J.-G. Zhang, arXiv preprint, arXiv:1910.11513, 2019.
- 65 Y. Li, Y. Li, A. Pei, K. Yan, Y. Sun, C.-L. Wu, L.-M. Joubert, R. Chin, A. L. Koh and Y. Yu, *Science*, 2017, **358**, 506–510.
- 66 Y. He, X. Ren, Y. Xu, M. H. Engelhard, X. Li, J. Xiao, J. Liu, J.-G. Zhang, W. Xu and C. Wang, *Nat. Nanotechnol.*, 2019, **14**, 602–609.
- 67 F. Cosandey, D. Su, M. Sina, N. Pereira and G. G. Amatucci, *Micron*, 2012, **43**, 22–29.
- 68 J. K. Zheng, X. Xu, R. Luo, X. Zeng and B. Chen, *J. Alloys Compd.*, 2018, **741**, 656–660.
- 69 J. Zheng, Z. Luo, L. Tan and B. Chen, *Microsc. Microanal.*, 2016, **22**, 1244–1250.
- 70 X. Xu, J. Zheng, Z. Li, R. Luo and B. Chen, *Mater. Sci. Eng., A*, 2017, **691**, 60–70.
- 71 Z. Sun, D. Oka and T. Fukumura, *Cryst. Growth Des.*, 2019, **19**, 7170–7174.
- 72 H. Gao, Q. Sun, M. Lysevych, H. H. Tan, C. Jagadish and J. Zou, *Cryst. Growth Des.*, 2019, **19**, 5314–5319.
- 73 K. Uosaki, S. Ye, H. Naohara, Y. Oda, T. Haba and T. Kondo, *J. Phys. Chem. B*, 1997, **101**, 7566–7572.
- 74 S. Hwang, I. Oh and J. Kwak, *J. Am. Chem. Soc.*, 2001, **123**, 7176–7177.
- 75 L. Viyannalage, R. Vasilic and N. Dimitrov, *J. Phys. Chem. C*, 2007, **111**, 4036–4041.
- 76 X. Xin, K. Ito and Y. Kubo, *ACS Appl. Mater. Interfaces*, 2017, **9**, 25976–25984.
- 77 X. Xin, K. Ito, A. Dutta and Y. Kubo, *Angew. Chem., Int. Ed.*, 2018, **57**, 13206–13210.
- 78 N. Li, K. Zhang, K. Xie, W. Wei, Y. Gao, M. Bai, Y. Gao, Q. Hou, C. Shen and Z. Xia, *Adv. Mater.*, 2019, **9**, 1907079.
- 79 A. J. Bard, L. R. Faulkner, J. Leddy and C. G. Zoski, *Electrochemical methods: fundamentals and applications*, Wiley, New York, 1980.
- 80 M. D. Tikekar, L. A. Archer and D. L. Koch, *J. Electrochem. Soc.*, 2014, **161**, A847–A855.
- 81 S. Wei, Z. Cheng, P. Nath, M. D. Tikekar, G. Li and L. A. Archer, *Sci. Adv.*, 2018, **4**, eaao6243.
- 82 H. J. S. Sand, *London, Edinburgh Dublin Philos. Mag. J. Sci.*, 1901, **1**, 45–79.
- 83 M. D. Tikekar, S. Choudhury, Z. Tu and L. A. Archer, *Nat. Energy*, 2016, **1**, 16114.
- 84 P. Bai, J. Li, F. R. Brushett and M. Z. Bazant, *Energy Environ. Sci.*, 2016, **9**, 3221–3229.
- 85 W. H. Smyrl and J. Newman, *Trans. Faraday Soc.*, 1967, **63**, 207–216.
- 86 I. Rubinstein and L. Shtilman, *J. Chem. Soc., Faraday Trans. 2*, 1979, **75**, 231–246.
- 87 I. Rubinstein and B. Zaltzman, *Phys. Rev. E: Stat. Phys., Plasmas, Fluids, Relat. Interdiscip. Top.*, 2000, **62**, 2238.
- 88 B. Zaltzman and I. Rubinstein, *J. Fluid Mech.*, 2007, **579**, 173–226.
- 89 M. D. Tikekar, G. Li, L. A. Archer and D. L. Koch, *J. Electrochem. Soc.*, 2018, **165**, A3697–A3713.
- 90 C. L. Druzgalski, M. B. Andersen and A. Mani, *Phys. Fluids*, 2013, **25**, 110804.
- 91 J. N. Chazalviel, *Phys. Rev. A: At., Mol., Opt. Phys.*, 1990, **42**, 7355–7367.

- 92 V. Fleury, J. N. Chazalviel and M. Rosso, *Phys. Rev. E: Stat. Phys., Plasmas, Fluids, Relat. Interdiscip. Top.*, 1993, **48**, 1279.
- 93 J. M. Huth, H. L. Swinney, W. D. McCormick, A. Kuhn and F. Argoul, *Phys. Rev. E: Stat. Phys., Plasmas, Fluids, Relat. Interdiscip. Top.*, 1995, **51**, 3444.
- 94 M. Wang, W. J. P. van Enkevort, N.-B. Ming and P. Bennema, *Nature*, 1994, **367**, 438.
- 95 G. Li, L. A. Archer and D. L. Koch, *Phys. Rev. Lett.*, 2019, **122**, 124501.
- 96 A. Warren, D. Zhang, S. Choudhury and L. A. Archer, *Macromolecules*, 2019, **52**(12), 4666–4672.
- 97 N. P. W. Langenhuisen, *J. Electrochem. Soc.*, 1998, **145**, 3094–3099.
- 98 K. Nishikawa, T. Mori, T. Nishida, Y. Fukunaka, M. Rosso and T. Homma, *J. Electrochem. Soc.*, 2010, **157**, A1212–A1217.
- 99 K. Nishikawa, Y. Fukunaka, T. Sakka, Y. H. Ogata and J. R. Selman, *J. Electrochem. Soc.*, 2007, **154**, A943–A948.
- 100 M. Ota, S. Izuo, K. Nishikawa, Y. Fukunaka, E. Kusaka, R. Ishii and J. R. Selman, *J. Electroanal. Chem.*, 2003, **559**, 175–183.
- 101 K. Nishikawa, M. Ota, S. Izuo, Y. Fukunaka, E. Kusaka, R. Ishii and J. R. Selman, *J. Solid State Electrochem.*, 2004, **8**, 174–181.
- 102 S. Choudhury, S. Stalin, D. Vu, A. Warren, Y. Deng, P. Biswal and L. A. Archer, *Nat. Commun.*, 2019, **10**, 1–8.
- 103 Z. Tu, S. Choudhury, M. J. Zachman, S. Wei, K. Zhang, L. F. Kourkoutis and L. A. Archer, *Joule*, 2017, **1**, 394–406.
- 104 T. Nishida, K. Nishikawa, M. Rosso and Y. Fukunaka, *Electrochim. Acta*, 2013, **100**, 333–341.
- 105 K. Nishikawa, H. Naito, M. Kawase and T. Nishida, *ECS Trans.*, 2012, **41**, 3–10.
- 106 K. Nishikawa, T. Mori, T. Nishida, Y. Fukunaka and M. Rosso, *J. Electroanal. Chem.*, 2011, **661**, 84–89.
- 107 J. Steiger, D. Kramer and R. Mönig, *J. Power Sources*, 2014, **261**, 112–119.
- 108 J. Steiger, D. Kramer and R. Mönig, *Electrochim. Acta*, 2014, **136**, 529–536.
- 109 D. Rehnlund, C. Ihrfors, J. Maibach and L. Nyholm, *Mater. Today*, 2018, **21**, 1010–1018.
- 110 M. D. Tikekar, *The effect of ion transport and electrolyte rheology on morphological instabilities in electrodeposition*, PhD thesis, Cornell University, 2017.
- 111 R. A. Enrique, S. DeWitt and K. Thornton, *MRS Commun.*, 2017, **7**, 658–663.
- 112 G. L. Zhu, C. Z. Zhao, J. Q. Huang, C. He, J. Zhang, S. Chen, L. Xu, H. Yuan and Q. Zhang, *Small*, 2019, **15**, 1805389.
- 113 P. Biswal, S. Stalin, A. Kludze, S. Choudhury and L. A. Archer, *Nano Lett.*, 2019, **19**(11), 8191–8200.
- 114 B. Wang, Y. Han, S. Xu, L. Qiu, F. Ding, J. Lou and Y. Lu, *Small*, 2018, **14**, 1704085.
- 115 H. Zheng, Y. Liu, F. Cao, S. Wu, S. Jia, A. Cao, D. Zhao and J. Wang, *Sci. Rep.*, 2013, **3**, 1920.
- 116 L. Li, S. Basu, Y. Wang, Z. Chen, P. Hundekar, B. Wang, J. Shi, Y. Shi, S. Narayanan and N. Koratkar, *Science*, 2018, **359**, 1513–1516.
- 117 D. Aurbach, Y. Cohen and M. Moshkovich, *Electrochem. Solid-State Lett.*, 2001, **4**, A113–A116.
- 118 Q. S. Zhao, Y. N. NuLi, Y. S. Guo, J. Yang and J. L. Wang, *Electrochim. Acta*, 2011, **56**, 6530–6535.
- 119 R. Davidson, A. Verma, D. Santos, F. Hao, C. Fincher, S. Xiang, J. Van Buskirk, K. Xie, M. Pharr and P. P. Mukherjee, *ACS Energy Lett.*, 2018, **4**, 375–376.
- 120 F. Hao, A. Verma and P. P. Mukherjee, *ACS Appl. Mater. Interfaces*, 2018, **10**, 26320–26327.
- 121 M. Jäckle and A. Groß, *J. Chem. Phys.*, 2014, **141**, 174710.
- 122 M. Jäckle, K. Helmbrecht, M. Smits, D. Stottmeister and A. Groß, *Energy Environ. Sci.*, 2018, **11**, 3400–3407.
- 123 D. Gaissmaier, D. Fantauzzi and T. Jacob, *J. Chem. Phys.*, 2019, **150**, 041723.
- 124 Y. Ozhaves, D. Gunceler and T. A. Arias, arXiv preprint, arXiv:1504.05799, 2015.
- 125 S. Choudhury, S. Wei, Y. Ozhaves, D. Gunceler, M. J. Zachman, Z. Tu, J. H. Shin, P. Nath, A. Agrawal and L. F. Kourkoutis, *Nat. Commun.*, 2017, **8**, 898.
- 126 M. S. Kim, S. H. Lee, M.-S. Kim, J.-H. Ryu, K.-R. Lee, L. A. Archer and W. I. Cho, *Sci. Adv.*, 2019, **5**, eaax5587.
- 127 T. Kawamura, S. Okada and J.-I. Yamaki, *J. Power Sources*, 2006, **156**, 547–554.
- 128 E. Peled, *J. Electrochem. Soc.*, 1979, **126**, 2047–2051.
- 129 E. Peled and S. Menkin, *J. Electrochem. Soc.*, 2017, **164**, A1703–A1719.
- 130 S. Shiraishi, K. Kanamura and Z. Takehara, *J. Appl. Electrochem.*, 1995, **25**(6), 584–591.
- 131 T. Fujieda, N. Yamamoto, K. Saito, T. Ishibashi, M. Honjo, S. Koike, N. Wakabayashi and S. Higuchi, *J. Power Sources*, 1994, **52**, 197–200.
- 132 S. Shiraishi, K. Kanamura and Z. I. Takehara, *J. Appl. Electrochem.*, 1999, **29**, 867–879.
- 133 D. Aurbach, *J. Power Sources*, 2000, **89**, 206–218.
- 134 R. Bouchet, *Nat. Nanotechnol.*, 2014, **9**, 572.
- 135 Y. Li, Y. Li, Y. Sun, B. Butz, K. Yan, A. L. Koh, J. Zhao, A. Pei and Y. Cui, *Nano Lett.*, 2017, **17**, 5171–5178.
- 136 M. J. Zachman, Z. Tu, S. Choudhury, L. A. Archer and L. F. Kourkoutis, *Nature*, 2018, **560**, 345–349.
- 137 A. L. Michan, B. S. Parimalam, M. Leskes, R. N. Kerber, T. Yoon, C. P. Grey and B. L. Lucht, *Chem. Mater.*, 2016, **28**, 8149–8159.
- 138 W. Huang, D. T. Boyle, Y. Li, Y. Li, A. Pei, H. Chen and Y. Cui, *ACS Nano*, 2018, **13**, 737–744.
- 139 C. Hou, J. Han, P. Liu, C. Yang, G. Huang, T. Fujita, A. Hirata and M. Chen, *Adv. Energy Mater.*, 2019, **9**, 1902675.
- 140 F. A. Soto, Y. Ma, J. M. Martinez de la Hoz, J. M. Seminario and P. B. Balbuena, *Chem. Mater.*, 2015, **27**, 7990–8000.
- 141 S. Jurng, Z. L. Brown, J. Kim and B. L. Lucht, *Energy Environ. Sci.*, 2018, **11**, 2600–2608.
- 142 F. Ding, W. Xu, X. Chen, J. Zhang, M. H. Engelhard, Y. Zhang, B. R. Johnson, J. V. Crum, T. A. Blake and X. Liu, *J. Electrochem. Soc.*, 2013, **160**, A1894–A1901.
- 143 H. Ota, K. Shima, M. Ue and J.-I. Yamaki, *Electrochim. Acta*, 2004, **49**, 565–572.
- 144 J. Z. Lee, T. A. Wynn, M. A. Schroeder, J. Alvarado, X. Wang, K. Xu and Y. S. Meng, *ACS Energy Lett.*, 2019, **4**, 489–493.

- 145 F. Shi, A. Pei, D. T. Boyle, J. Xie, X. Yu, X. Zhang and Y. Cui, *Proc. Natl. Acad. Sci. U. S. A.*, 2018, **115**, 8529–8534.
- 146 Y. Li, W. Huang, Y. Li, A. Pei, D. T. Boyle and Y. Cui, *Joule*, 2018, **2**, 2167–2177.
- 147 Y. Lu, Z. Tu and L. A. Archer, *Nat. Mater.*, 2014, **13**, 961.
- 148 L. Fan, H. L. Zhuang, L. Gao, Y. Lu and L. A. Archer, *J. Mater. Chem. A*, 2017, **5**, 3483–3492.
- 149 S. Choudhury and L. A. Archer, *Adv. Electron. Mater.*, 2016, **2**, 1500246.
- 150 T. Hou, G. Yang, N. N. Rajput, J. Self, S.-W. Park, J. Nanda and K. A. Persson, *Nano Energy*, 2019, **64**, 103881.
- 151 X. Q. Zhang, X. B. Cheng, X. Chen, C. Yan and Q. Zhang, *Adv. Funct. Mater.*, 2017, **27**, 1605989.
- 152 L. Suo, W. Xue, M. Gobet, S. G. Greenbaum, C. Wang, Y. Chen, W. Yang, Y. Li and J. Li, *Proc. Natl. Acad. Sci. U. S. A.*, 2018, **115**, 1156–1161.
- 153 R. McMillan, H. Sleg, Z. X. Shu and W. Wang, *J. Power Sources*, 1999, **81**, 20–26.
- 154 N.-S. Choi, K. H. Yew, K. Y. Lee, M. Sung, H. Kim and S.-S. Kim, *J. Power Sources*, 2006, **161**, 1254–1259.
- 155 Z. L. Brown, S. Jurng, C. C. Nguyen and B. L. Lucht, *ACS Appl. Energy Mater.*, 2018, **1**, 3057–3062.
- 156 Z. Liu, Y. Qi, Y. X. Lin, L. Chen, P. Lu and L. Q. Chen, *J. Electrochem. Soc.*, 2016, **163**, A592–A598.
- 157 K.-i. Chung, J.-D. Lee, E.-J. Kim, W.-S. Kim, J.-H. Cho and Y.-K. Choi, *Microchem. J.*, 2003, **75**, 71–77.
- 158 R. Rodriguez, K. E. Loeffler, S. S. Nathan, J. K. Sheavly, A. Dolocan, A. Heller and C. B. Mullins, *ACS Energy Lett.*, 2017, **2**, 2051–2057.
- 159 P. Lu and S. J. Harris, *Electrochem. Commun.*, 2011, **13**, 1035–1037.
- 160 A. Maraschky and R. Akolkar, *J. Electrochem. Soc.*, 2018, **165**, D696–D703.
- 161 X.-R. Chen, Y.-X. Yao, C. Yan, R. Zhang, X.-B. Cheng and Q. Zhang, *Angew. Chem.*, 2020, DOI: 10.1002/ange.202000375.
- 162 C. Delacourt, A. Kwong, X. Liu, R. Qiao, W. L. Yang, P. Lu, S. J. Harris and V. Srinivasan, *J. Electrochem. Soc.*, 2013, **160**, A1099–A1107.
- 163 W. Li, U.-H. Kim, A. Dolocan, Y.-K. Sun and A. Manthiram, *ACS Nano*, 2017, **11**, 5853–5863.
- 164 J. Steiger, G. Richter, M. Wenk, D. Kramer and R. Mönig, *Electrochem. Commun.*, 2015, **50**, 11–14.
- 165 M. Schamel, C. Schopf, D. Linsler, S. T. Haag, L. Hofacker, C. Kappel, H. P. Strunk and G. Richter, *Int. J. Mater. Res.*, 2011, **102**, 828–836.
- 166 L. Gireaud, S. Grugeon, S. Laruelle, B. Yrieix and J. M. Tarascon, *Electrochem. Commun.*, 2006, **8**, 1639–1649.
- 167 Y. Zhu, X. He and Y. Mo, *ACS Appl. Mater. Interfaces*, 2015, **7**, 23685–23693.
- 168 W. Huang, P. M. Attia, H. Wang, S. E. Renfrew, N. Jin, S. Das, Z. Zhang, D. T. Boyle, Y. Li and M. Z. Bazant, *Nano Lett.*, 2019, **19**, 5140–5148.
- 169 G. Odian, *Principles of polymerization*, John Wiley & Sons, 2004.
- 170 H. Yildirim, A. Kinaci, M. K. Y. Chan and J. P. Greeley, *ACS Appl. Mater. Interfaces*, 2015, **7**, 18985–18996.
- 171 Y. Lu, Z. Tu, J. Shu and L. A. Archer, *J. Power Sources*, 2015, **279**, 413–418.
- 172 G. Cohn, L. Ma and L. A. Archer, *J. Power Sources*, 2015, **283**, 416–422.
- 173 Z. Liu, S. Z. El Abedin and F. Endres, *Electrochim. Acta*, 2013, **89**, 635–643.
- 174 U. Sahaym, S. L. Miller and M. G. Norton, *Mater. Lett.*, 2010, **64**, 1547–1550.
- 175 M. Ishikawa, Y. Tasaka, N. Yoshimoto and M. Morita, *J. Power Sources*, 2001, **97**, 262–264.
- 176 M. Ishikawa, Y. Takaki, M. Morita and Y. Matsuda, *J. Electrochem. Soc.*, 1997, **144**, L90–L92.
- 177 H. E. Park, C. H. Hong and W. Y. Yoon, *J. Power Sources*, 2008, **178**, 765–768.
- 178 C. T. Love, O. A. Baturina and K. E. Swider-Lyons, *ECS Electrochem. Lett.*, 2015, **4**, A24–A27.
- 179 R. W. Atkinson III, R. Carter and C. T. Love, *Energy Storage Mater.*, 2019, **22**, 18–28.
- 180 C. T. Love, *J. Electrochem. Energy Convers. Storage*, 2016, **13**, 031004.
- 181 R. Mogi, M. Inaba, T. Abe and Z. Ogumi, *J. Power Sources*, 2001, **97**, 265–268.
- 182 R. Mogi, M. Inaba, Y. Iriyama, T. Abe and Z. Ogumi, *J. Electrochem. Soc.*, 2002, **149**, A385–A390.
- 183 K. Yan, J. Wang, S. Zhao, D. Zhou, B. Sun, Y. Cui and G. Wang, *Angew. Chem.*, 2019, **131**(33), 11486–11490.
- 184 Y. Guo, D. Li, R. Xiong and H. Li, *Chem. Commun.*, 2019, **55**, 9773–9776.
- 185 Y. Han, Y. Jie, F. Huang, Y. Chen, Z. Lei, G. Zhang, X. Ren, L. Qin, R. Cao and S. Jiao, *Adv. Funct. Mater.*, 2019, **29**, 1904629.
- 186 H. Lundgren, M. Behm and G. Lindbergh, *J. Electrochem. Soc.*, 2015, **162**, A413–A420.
- 187 A. Aryanfar, T. Cheng, A. J. Colussi, B. V. Merinov, W. A. Goddard III and M. R. Hoffmann, *J. Chem. Phys.*, 2015, **143**, 134701.
- 188 A. Aryanfar, D. J. Brooks, A. J. Colussi, B. V. Merinov, W. A. Goddard III and M. R. Hoffmann, *Phys. Chem. Chem. Phys.*, 2015, **17**, 8000–8005.
- 189 Z. Hong and V. Viswanathan, *ACS Energy Lett.*, 2019, **4**, 1012–1019.
- 190 J. Wang, W. Huang, A. Pei, Y. Li, F. Shi, X. Yu and Y. Cui, *Nat. Energy*, 2019, **4**, 664–670.
- 191 W. S. LePage, Y. Chen, E. Kazyak, K.-H. Chen, A. J. Sanchez, A. Poli, E. M. Arruda, M. D. Thouless and N. P. Dasgupta, *J. Electrochem. Soc.*, 2019, **166**, A89–A97.
- 192 K. Zhao and Y. Cui, *Extreme Mech. Lett.*, 2016, **9**, 347–352.
- 193 M. R. Palacín and A. de Guibert, *Science*, 2016, **351**, 1253292.
- 194 C. Monroe and J. Newman, *J. Electrochem. Soc.*, 2005, **152**, A396–A404.
- 195 M. D. Tikekar, L. A. Archer and D. L. Koch, *Sci. Adv.*, 2016, **2**, e1600320.
- 196 S. Narayan and L. Anand, *Extreme Mech. Lett.*, 2018, **24**, 21–29.
- 197 A. Ferrese and J. Newman, *J. Electrochem. Soc.*, 2014, **161**, A1350–A1359.

- 198 X. Zhang, Q. J. Wang, K. L. Harrison, S. A. Roberts and S. J. Harris, *Cell Rep. Phys. Sci.*, 2020, **1**, 100012.
- 199 G. M. Stone, S. A. Mullin, A. A. Teran, D. T. Hallinan, A. M. Minor, A. Hexemer and N. P. Balsara, *J. Electrochem. Soc.*, 2012, **159**, A222–A227.
- 200 R. Khurana, J. L. Schaefer, L. A. Archer and G. W. Coates, *J. Am. Chem. Soc.*, 2014, **136**, 7395–7402.
- 201 Z. Tu, M. J. Zachman, S. Choudhury, S. Wei, L. Ma, Y. Yang, L. F. Kourkoutis and L. A. Archer, *Adv. Energy Mater.*, 2017, **7**, 1602367.
- 202 S. Choudhury, *Rational Design of Nanostructured Polymer Electrolytes and Solid–Liquid Interphases for Lithium Batteries*, Springer, 2019, pp. 59–79.
- 203 C. Xu, Z. Ahmad, A. Aryanfar, V. Viswanathan and J. R. Greer, *Proc. Natl. Acad. Sci. U. S. A.*, 2017, **114**, 57–61.
- 204 Y. Wang and Y.-T. Cheng, *Scr. Mater.*, 2017, **130**, 191–195.
- 205 S. Tariq, K. Ammigan, P. Hurh, R. Schultz, P. Liu and J. Shang, Li material testing-fermilab antiproton source lithium collection lens, in *Proceedings of the 2003 particle accelerator conference*, IEEE, 2003, vol. 3, pp. 1452–1454.
- 206 R. P. Schultz, *Lithium: Measurement of Young's Modulus and Yield Strength*, Fermi National Accelerator Lab., Batavia, IL (US), 2002.
- 207 W. M. Robertson and D. J. Montgomery, *Phys. Rev.*, 1960, **117**, 440.
- 208 E. G. Herbert, S. A. Hackney, N. J. Dudney and P. S. Phani, *J. Mater. Res.*, 2018, **33**, 1335–1346.
- 209 E. G. Herbert, S. A. Hackney, V. Thole, N. J. Dudney and P. S. Phani, *J. Mater. Res.*, 2018, **33**, 1361–1368.
- 210 E. G. Herbert, S. A. Hackney, V. Thole, N. J. Dudney and P. S. Phani, *J. Mater. Res.*, 2018, **33**, 1347–1360.
- 211 A. Raju Natarajan and A. Van der Ven, *Chem. Mater.*, 2019, **31**(19), 8222–8229.
- 212 R. Messer and F. Noack, *Appl. Phys.*, 1975, **6**, 79–88.
- 213 W. Yuan, S. K. Panigrahi, J. Q. Su and R. S. Mishra, *Scr. Mater.*, 2011, **65**, 994–997.
- 214 C. Campbell, Y. M. Lee, K. Y. Cho, Y.-G. Lee, B. Lee, C. Phatak and S. Hong, *Sci. Rep.*, 2018, **8**, 2514.
- 215 Y. Wang, D. Dang, M. Wang, X. Xiao and Y.-T. Cheng, *Appl. Phys. Lett.*, 2019, **115**, 043903.
- 216 J. Zhang, R. Wang, X. Yang, W. Lu, X. Wu, X. Wang, H. Li and L. Chen, *Nano Lett.*, 2012, **12**, 2153–2157.
- 217 J. Zheng, H. Zheng, R. Wang, L. Ben, W. Lu, L. Chen, L. Chen and H. Li, *Phys. Chem. Chem. Phys.*, 2014, **16**, 13229–13238.
- 218 H. Shin, J. Park, S. Han, A. M. Sastry and W. Lu, *J. Power Sources*, 2015, **277**, 169–179.
- 219 I. Yoon, S. Jurng, D. P. Abraham, B. L. Lucht and P. R. Guduru, *Nano Lett.*, 2018, **18**, 5752–5759.
- 220 C. M. Stafford, C. Harrison, K. L. Beers, A. Karim, E. J. Amis, M. R. VanLandingham, H.-C. Kim, W. Volksen, R. D. Miller and E. E. Simonyi, *Nat. Mater.*, 2004, **3**, 545.
- 221 P. Barai, K. Higa and V. Srinivasan, *J. Electrochem. Soc.*, 2017, **164**, A180–A189.
- 222 V. Yurkiv, T. Foroozan, A. Ramasubramanian, R. Shahbazian-Yassar and F. Mashayek, *MRS Commun.*, 2018, **8**, 1285–1291.
- 223 L.-G. Sundström and F. H. Bark, *Electrochim. Acta*, 1995, **40**, 599–614.
- 224 J. L. Barton and J. O. M. Bockris, *Proc. R. Soc. London, Ser. A*, 1962, **268**, 485–505.
- 225 P. Barai, K. Higa and V. Srinivasan, *Phys. Chem. Chem. Phys.*, 2017, **19**, 20493–20505.
- 226 P. Barai, K. Higa and V. Srinivasan, *J. Electrochem. Soc.*, 2018, **165**, A2654–A2666.
- 227 P. P. Natsiavas, K. Weinberg, D. Rosato and M. Ortiz, *J. Mech. Phys. Solids*, 2016, **95**, 92–111.
- 228 K. L. Harrison, K. R. Zavadil, N. T. Hahn, X. Meng, J. W. Elam, A. Leenheer, J.-G. Zhang and K. L. Jungjohann, *ACS Nano*, 2017, **11**, 11194–11205.
- 229 X. Yin, W. Tang, K. C. Phua, S. Adams, S. W. Lee and G. W. Zheng, *Nano Energy*, 2018, **50**, 659–664.
- 230 A. J. Louli, M. Genovese, R. Weber, S. G. Hames, E. R. Logan and J. R. Dahn, *J. Electrochem. Soc.*, 2019, **166**, A1291–A1299.
- 231 T. Z. Fahidy, *J. Appl. Electrochem.*, 1983, **13**, 553–563.
- 232 L. M. A. Monzon and J. M. D. Coey, *Electrochem. Commun.*, 2014, **42**, 38–41.
- 233 J. M. D. Coey and G. Hinds, *J. Alloys Compd.*, 2001, **326**, 238–245.
- 234 I. Mogi and M. Kamiko, *J. Cryst. Grow.*, 1996, **166**, 276–280.
- 235 H. Matsushima, A. Bund, W. Plieth, S. Kikuchi and Y. Fukunaka, *Electrochim. Acta*, 2007, **53**, 161–166.
- 236 K. Shen, Z. Wang, X. Bi, Y. Ying, D. Zhang, C. Jin, G. Hou, H. Cao, L. Wu and G. Zheng, *Adv. Energy Mater.*, 2019, **9**, 1900260, DOI: 10.1002/aenm.201900260.
- 237 A. Wang, Q. Deng, L. Deng, X. Guan and J. Luo, *Adv. Funct. Mater.*, 2019, **29**, 1902630, DOI: 10.1002/adfm.201902630.
- 238 C. Wagner, *J. Electrochem. Soc.*, 1949, **95**, 161–173.
- 239 W. J. Ward and O. H. Le Blanc, *Science*, 1984, **225**, 1471–1473.
- 240 Y. Fukunaka, K. Okano, Y. Tomii, Z. Asaki and K. Kuribayashi, *J. Electrochem. Soc.*, 1998, **145**, 1876–1881.
- 241 K. Nishikawa, Y. Fukunaka, E. Chassaing and M. Rosso, *Electrochim. Acta*, 2013, **100**, 342–349.
- 242 E. Karatay, M. B. Andersen, M. Wessling and A. Mani, *Phys. Rev. Lett.*, 2016, **116**, 194501.
- 243 M. Monev, L. Mirkova, I. Krastev, H. Tsvetkova and W. Richtering, *J. Appl. Electrochem.*, 1998, **28**, 1107–1112.
- 244 W. L. Tsai, P. C. Hsu, Y. Hwu, C. H. Chen, L. W. Chang, J. H. Je, H. M. Lin, A. Groso and G. Margaritondo, *Nature*, 2002, **417**, 139.
- 245 S. S. Zhang, *Front. Energy Res.*, 2014, **2**, 59.
- 246 R. Zhu, J. Feng and Z. Guo, *J. Electrochem. Soc.*, 2019, **166**, A1107–A1113.
- 247 D. Lin, Y. Liu, Y. Li, Y. Li, A. Pei, J. Xie, W. Huang and Y. Cui, *Nat. Chem.*, 2019, **11**, 382.
- 248 D. Aurbach, Y. Talyosef, B. Markovsky, E. Markevich, E. Zinigrad, L. Asraf, J. S. Gnanaraj and H.-J. Kim, *Electrochim. Acta*, 2004, **50**, 247–254.
- 249 N. W. Li, Y. X. Yin, J. Y. Li, C. H. Zhang and Y. G. Guo, *Adv. Sci.*, 2017, **4**, 1600400.
- 250 Y. Lu, S. K. Das, S. S. Moganty and L. A. Archer, *Adv. Mater.*, 2012, **24**, 4430–4435.

- 251 K. Wang, K. Jiang, B. Chung, T. Ouchi, P. J. Burke, D. A. Boysen, D. J. Bradwell, H. Kim, U. Muecke and D. R. Sadoway, *Nature*, 2014, **514**, 348.
- 252 C. Cao, Z.-B. Li, X.-L. Wang, X.-B. Zhao and W.-Q. Han, *Front. Energy Res.*, 2014, **2**, 25.
- 253 J. Y. Song, Y. Y. Wang and C. C. Wan, *J. Power Sources*, 1999, **77**, 183–197.
- 254 R. Koksang, I. I. Olsen and D. Shackle, *Solid State Ionics*, 1994, **69**, 320–335.
- 255 J. L. Nugent, S. S. Moganty and L. A. Archer, *Adv. Mater.*, 2010, **22**, 3677–3680.
- 256 S.-K. Kim, D.-G. Kim, A. Lee, H.-S. Sohn, J. J. Wie, N. A. Nguyen, M. E. Mackay and J.-C. Lee, *Macromolecules*, 2012, **45**, 9347–9356.
- 257 Q. Zhao, S. Stalin, C.-Z. Zhao and L. A. Archer, *Nat. Rev. Mater.*, 2020, **5**, 229–252.
- 258 K. Xu, *Chem. Rev.*, 2004, **104**, 4303–4418.
- 259 J. B. Goodenough and Y. Kim, *J. Power Sources*, 2011, **196**, 6688–6694.
- 260 M. Winter, *Z. Phys. Chem.*, 2009, **223**, 1395–1406.
- 261 Z. Tu, P. Nath, Y. Lu, M. D. Tikekar and L. A. Archer, *Acc. Chem. Res.*, 2015, **48**, 2947–2956.
- 262 X. B. Cheng, R. Zhang, C. Z. Zhao, F. Wei, J. G. Zhang and Q. Zhang, *Adv. Sci.*, 2016, **3**, 1500213.
- 263 X.-B. Cheng, R. Zhang, C.-Z. Zhao and Q. Zhang, *Chem. Rev.*, 2017, **117**, 10403–10473.
- 264 J. Qian, W. A. Henderson, W. Xu, P. Bhattacharya, M. Engelhard, O. Borodin and J.-G. Zhang, *Nat. Commun.*, 2015, **6**, 6362.
- 265 S. Wei, S. Choudhury, Z. Tu, K. Zhang and L. A. Archer, *Acc. Chem. Res.*, 2017, **51**, 80–88.
- 266 O. Y. Chusid, E. E. Ely, D. Aurbach, M. Babai and Y. Carmeli, *J. Power Sources*, 1993, **43**, 47–64.
- 267 R. Miao, J. Yang, X. Feng, H. Jia, J. Wang and Y. Nuli, *J. Power Sources*, 2014, **271**, 291–297.
- 268 H. Ota, Y. Sakata, A. Inoue and S. Yamaguchi, *J. Electrochem. Soc.*, 2004, **151**, A1659–A1669.
- 269 X. Q. Zhang, X. Chen, X. B. Cheng, B. Q. Li, X. Shen, C. Yan, J. Q. Huang and Q. Zhang, *Angew. Chem., Int. Ed.*, 2018, **57**, 5301–5305.
- 270 D. M. Seo, D. Chalasani, B. S. Parimalam, R. Kadam, M. Nie and B. L. Lucht, *ECS Electrochem. Lett.*, 2014, **3**, A91–A93.
- 271 L. Xing, X. Zheng, M. Schroeder, J. Alvarado, A. von Wald Cresce, K. Xu, Q. Li and W. Li, *Acc. Chem. Res.*, 2018, **51**, 282–289.
- 272 S. Choudhury, Z. Tu, S. Stalin, D. Vu, K. Fawole, D. Gunceler, R. Sundararaman and L. A. Archer, *Angew. Chem., Int. Ed.*, 2017, **56**, 13070–13077.
- 273 W. Li, H. Yao, K. Yan, G. Zheng, Z. Liang, Y.-M. Chiang and Y. Cui, *Nat. Commun.*, 2015, **6**, 7436.
- 274 C. Yan, X.-B. Cheng, C.-Z. Zhao, J.-Q. Huang, S.-T. Yang and Q. Zhang, *J. Power Sources*, 2016, **327**, 212–220.
- 275 H. Zhang, G. G. Eshetu, X. Judez, C. Li, L. M. Rodriguez-Martínez and M. Armand, *Angew. Chem., Int. Ed.*, 2018, **57**, 15002–15027.
- 276 A. Basile, A. I. Bhatt and A. P. O'Mullane, *Nat. Commun.*, 2016, **7**, 11794, DOI: 10.1038/ncomms11794.
- 277 W. Jia, Q. Wang, J. Yang, C. Fan, L. Wang and J. Li, *ACS Appl. Mater. Interfaces*, 2017, **9**, 7068–7074.
- 278 D. Lin, Y. Liu, W. Chen, G. Zhou, K. Liu, B. Dunn and Y. Cui, *Nano Lett.*, 2017, **17**, 3731–3737.
- 279 Q. Zhao, Z. Tu, S. Wei, K. Zhang, S. Choudhury, X. Liu and L. A. Archer, *Angew. Chem.*, 2018, **130**, 1004–1008.
- 280 F. Ding, W. Xu, G. L. Graff, J. Zhang, M. L. Sushko, X. Chen, Y. Shao, M. H. Engelhard, Z. Nie and J. Xiao, *J. Am. Chem. Soc.*, 2013, **135**, 4450–4456.
- 281 N. A. Sahalie, A. A. Assegie, W.-N. Su, Z. T. Wondimkun, B. A. Jote, B. Thirumalraj, C.-J. Huang, Y.-W. Yang and B.-J. Hwang, *J. Power Sources*, 2019, **437**, 226912.
- 282 J. L. Schaefer, Y. Lu, S. S. Moganty, P. Agarwal, N. Jayaprakash and L. A. Archer, *Appl. Nanosci.*, 2012, **2**, 91–109.
- 283 X.-B. Cheng, M.-Q. Zhao, C. Chen, A. Pentecost, K. Maleski, T. Mathis, X.-Q. Zhang, Q. Zhang, J. Jiang and Y. Gogotsi, *Nat. Commun.*, 2017, **8**, 336.
- 284 Z. Li, J. Huang, B. Y. Liaw, V. Metzler and J. Zhang, *J. Power Sources*, 2014, **254**, 168–182.
- 285 Y. Guo, H. Li and T. Zhai, *Adv. Mater.*, 2017, **29**, 1700007.
- 286 Y. Zhu, Y. Li, M. Bettge and D. P. Abraham, *Electrochim. Acta*, 2013, **110**, 191–199.
- 287 S. S. Zhang, *J. Power Sources*, 2006, **162**, 1379–1394.
- 288 J. Zheng, M. H. Engelhard, D. Mei, S. Jiao, B. J. Polzin, J.-G. Zhang and W. Xu, *Nat. Energy*, 2017, **2**, 17012.
- 289 R. Weber, M. Genovese, A. J. Louli, S. Hames, C. Martin, I. G. Hill and J. R. Dahn, *Nat. Energy*, 2019, **4**, 683–689.
- 290 Y. Yang, D. M. Davies, Y. Yin, O. Borodin, J. Z. Lee, C. Fang, M. Olguin, Y. Zhang, E. S. Sablina and X. Wang, *Joule*, 2019, **3**, 1986–2000.
- 291 L. Suo, O. Borodin, T. Gao, M. Olguin, J. Ho, X. Fan, C. Luo, C. Wang and K. Xu, *Science*, 2015, **350**, 938–943.
- 292 S.-K. Jeong, M. Inaba, Y. Iriyama, T. Abe and Z. Ogumi, *Electrochemical and Solid-State Letters*, 2003, **6**, A13–A15.
- 293 M. Nie, D. P. Abraham, D. M. Seo, Y. Chen, A. Bose and B. L. Lucht, *J. Phys. Chem. C*, 2013, **117**, 25381–25389.
- 294 Y. Yamada, K. Usui, C. H. Chiang, K. Kikuchi, K. Furukawa and A. Yamada, *ACS Appl. Mater. Interfaces*, 2014, **6**, 10892–10899.
- 295 Y. Yamada, K. Furukawa, K. Sodeyama, K. Kikuchi, M. Yaegashi, Y. Tateyama and A. Yamada, *J. Am. Chem. Soc.*, 2014, **136**, 5039–5046.
- 296 S.-K. Jeong, M. Inaba, Y. Iriyama, T. Abe and Z. Ogumi, *J. Power Sources*, 2008, **175**, 540–546.
- 297 P. Shi, H. Zheng, X. Liang, Y. Sun, S. Cheng, C. Chen and H. Xiang, *Chem. Commun.*, 2018, **54**, 4453–4456.
- 298 Z. Zeng, V. Murugesan, K. S. Han, X. Jiang, Y. Cao, L. Xiao, X. Ai, H. Yang, J.-G. Zhang and M. L. Sushko, *Nat. Energy*, 2018, **3**, 674.
- 299 S. Chen, J. Zheng, D. Mei, K. S. Han, M. H. Engelhard, W. Zhao, W. Xu, J. Liu and J. G. Zhang, *Adv. Mater.*, 2018, **30**, 1706102.
- 300 X. Ren, S. Chen, H. Lee, D. Mei, M. H. Engelhard, S. D. Burton, W. Zhao, J. Zheng, Q. Li and M. S. Ding, *Chem*, 2018, **4**, 1877–1892.

- 301 X. Cao, X. Ren, L. Zou, M. H. Engelhard, W. Huang, H. Wang, B. E. Matthews, H. Lee, C. Niu and B. W. Arey, *Nat. Energy*, 2019, **4**, 796–805.
- 302 H. Wu, Y. Cao, H. Su and C. Wang, *Angew. Chem., Int. Ed.*, 2018, **57**, 1361–1365.
- 303 A. Manthiram, X. Yu and S. Wang, *Nat. Rev. Mater.*, 2017, **2**, 16103.
- 304 A. M. Stephan, *Eur. Polym. J.*, 2006, **42**, 21–42.
- 305 G. J. N. Wang, L. Shaw, J. Xu, T. Kurosawa, B. C. Schroeder, J. Y. Oh, S. J. Benight and Z. Bao, *Adv. Funct. Mater.*, 2016, **26**, 7254–7262.
- 306 S.-O. Tung, S. Ho, M. Yang, R. Zhang and N. A. Kotov, *Nat. Commun.*, 2015, **6**, 6152.
- 307 D. T. Hallinan, S. A. Mullin, G. M. Stone and N. P. Balsara, *J. Electrochem. Soc.*, 2013, **160**, A464–A470.
- 308 S. Choudhury, R. Mangal, A. Agrawal and L. A. Archer, *Nat. Commun.*, 2015, **6**, 10101, DOI: 10.1038/ncomms10101.
- 309 J. Wan, J. Xie, X. Kong, Z. Liu, K. Liu, F. Shi, A. Pei, H. Chen, W. Chen and J. Chen, *Nat. Nanotechnol.*, 2019, **1**.
- 310 Y. Lu, M. Tikekar, R. Mohanty, K. Hendrickson, L. Ma and L. A. Archer, *Adv. Energy Mater.*, 2015, **5**, 1402073.
- 311 L. Ma, P. Nath, Z. Tu, M. Tikekar and L. A. Archer, *Chem. Mater.*, 2016, **28**, 5147–5154.
- 312 R. Bouchet, S. Maria, R. Meziane, A. Aboulaich, L. Lienafa, J.-P. Bonnet, T. N. T. Phan, D. Bertin, D. Gigmes and D. Devaux, *Nat. Mater.*, 2013, **12**, 452.
- 313 S. Jiao, X. Ren, R. Cao, M. H. Engelhard, Y. Liu, D. Hu, D. Mei, J. Zheng, W. Zhao and Q. Li, *Nat. Energy*, 2018, **3**, 739.
- 314 S. Li, Y.-M. Chen, W. Liang, Y. Shao, K. Liu, Z. Nikolov and Y. Zhu, *Joule*, 2018, **2**, 1838–1856.
- 315 S. Choudhury, Z. Tu, A. Nijamudheen, M. J. Zachman, S. Stalin, Y. Deng, Q. Zhao, D. Vu, L. F. Kourkoutis and J. L. Mendoza-Cortes, *Nat. Commun.*, 2019, **10**, 1–11.
- 316 Q. Zhao, X. Liu, S. Stalin, K. Khan and L. A. Archer, *Nat. Energy*, 2019, **4**, 365.
- 317 J. Li, C. Ma, M. Chi, C. Liang and N. J. Dudney, *Adv. Energy Mater.*, 2015, **5**, 1401408.
- 318 X. Han, Y. Gong, K. K. Fu, X. He, G. T. Hitz, J. Dai, A. Pearse, B. Liu, H. Wang and G. Rubloff, *Nat. Mater.*, 2017, **16**, 572.
- 319 C. Wang, Y. Yang, X. Liu, H. Zhong, H. Xu, Z. Xu, H. Shao and F. Ding, *ACS Appl. Mater. Interfaces*, 2017, **9**, 13694–13702.
- 320 Y. Gao, D. Wang, Y. C. Li, Z. Yu, T. E. Mallouk and D. Wang, *Angew. Chem., Int. Ed.*, 2018, **57**, 13608–13612.
- 321 P. R. Chinnam and S. L. Wunder, *ACS Energy Lett.*, 2016, **2**, 134–138.
- 322 L. Chen, Y. Li, S.-P. Li, L.-Z. Fan, C.-W. Nan and J. B. Goodenough, *Nano Energy*, 2018, **46**, 176–184.
- 323 L. Yang, Z. Wang, Y. Feng, R. Tan, Y. Zuo, R. Gao, Y. Zhao, L. Han, Z. Wang and F. Pan, *Adv. Energy Mater.*, 2017, **7**, 1701437.
- 324 X. Xu, G. Hou, X. Nie, Q. Ai, Y. Liu, J. Feng, L. Zhang, P. Si, S. Guo and L. Ci, *J. Power Sources*, 2018, **400**, 212–217.
- 325 J. Zheng, M. Tang and Y. Y. Hu, *Angew. Chem., Int. Ed.*, 2016, **55**, 12538–12542.
- 326 W. Liu, S. W. Lee, D. Lin, F. Shi, S. Wang, A. D. Sendek and Y. Cui, *Nat. Energy*, 2017, **2**, 17035.
- 327 X. Liu, S. Peng, S. Gao, Y. Cao, Q. You, L. Zhou, Y. Jin, Z. Liu and J. Liu, *ACS Appl. Mater. Interfaces*, 2018, **10**, 15691–15696.
- 328 C.-Z. Zhao, H. Duan, J.-Q. Huang, J. Zhang, Q. Zhang, Y.-G. Guo and L.-J. Wan, *Sci. China: Chem.*, 2019, **62**, 1286–1299.
- 329 B. D. Adams, J. Zheng, X. Ren, W. Xu and J. G. Zhang, *Adv. Energy Mater.*, 2018, **8**, 1702097.
- 330 W. Xu, J. Wang, F. Ding, X. Chen, E. Nasybulin, Y. Zhang and J.-G. Zhang, *Energy Environ. Sci.*, 2014, **7**, 513–537.
- 331 A. M. Stephan and K. S. Nahm, *Polymer*, 2006, **47**, 5952–5964.
- 332 J. Lopez, A. Pei, J. Y. Oh, G.-J. N. Wang, Y. Cui and Z. Bao, *J. Am. Chem. Soc.*, 2018, **140**, 11735–11744.
- 333 H. Zhang, C. Liu, L. Zheng, F. Xu, W. Feng, H. Li, X. Huang, M. Armand, J. Nie and Z. Zhou, *Electrochim. Acta*, 2014, **133**, 529–538.
- 334 S. Li, H. Wang, J. Cuthbert, T. Liu, J. F. Whitacre and K. Matyjaszewski, *Joule*, 2019, **3**(7), 1637–1646.
- 335 A. A. Assegie, J.-H. Cheng, L.-M. Kuo, W.-N. Su and B.-J. Hwang, *Nanoscale*, 2018, **10**, 6125–6138.
- 336 M. S. Kim, L. Ma, S. Choudhury and L. A. Archer, *Adv. Mater. Interfaces*, 2016, **3**, 1600450.
- 337 M. S. Kim, L. Ma, S. Choudhury, S. S. Moganty, S. Wei and L. A. Archer, *J. Mater. Chem. A*, 2016, **4**, 14709–14719.
- 338 M. S. Kim, J.-H. Ryu, Y. R. Lim, I. W. Nah, K.-R. Lee, L. A. Archer and W. I. Cho, *Nat. Energy*, 2018, **3**, 889.
- 339 R. Xu, X. Q. Zhang, X. B. Cheng, H. J. Peng, C. Z. Zhao, C. Yan and J. Q. Huang, *Adv. Funct. Mater.*, 2018, **28**, 1705838.
- 340 N.-S. Choi, Y. M. Lee, W. Seol, J. A. Lee and J.-K. Park, *Solid State Ionics*, 2004, **172**, 19–24.
- 341 S. Wu, Y. Qiao, H. Deng and H. Zhou, *J. Mater. Chem. A*, 2018, **6**, 9816–9822.
- 342 S. Jiang, Y. Lu, Y. Lu, M. Han, H. Li, Z. Tao, Z. Niu and J. Chen, *Chem. – Asian J.*, 2018, **13**, 1379–1385.
- 343 C. B. Bucur, A. Lita, N. Osada and J. Muldoon, *Energy Environ. Sci.*, 2016, **9**, 112–116.
- 344 B. Zhu, Y. Jin, X. Hu, Q. Zheng, S. Zhang, Q. Wang and J. Zhu, *Adv. Mater.*, 2017, **29**, 1603755.
- 345 K. Liu, A. Pei, H. R. Lee, B. Kong, N. Liu, D. Lin, Y. Liu, C. Liu, P.-c. Hsu and Z. Bao, *J. Am. Chem. Soc.*, 2017, **139**, 4815–4820.
- 346 A. C. Kozen, C.-F. Lin, A. J. Pearse, M. A. Schroeder, X. Han, L. Hu, S.-B. Lee, G. W. Rubloff and M. Noked, *ACS Nano*, 2015, **9**, 5884–5892.
- 347 E. Kazyak, K. N. Wood and N. P. Dasgupta, *Chem. Mater.*, 2015, **27**, 6457–6462.
- 348 L. Chen, J. G. Connell, A. Nie, Z. Huang, K. R. Zavadil, K. C. Klavetter, Y. Yuan, S. Sharifi-Asl, R. Shahbazian-Yassar and J. A. Libera, *J. Mater. Chem. A*, 2017, **5**, 12297–12309.
- 349 H.-K. Jing, L.-L. Kong, S. Liu, G.-R. Li and X.-P. Gao, *J. Mater. Chem. A*, 2015, **3**, 12213–12219.

- 350 Y. Lu, S. S. Moganty, J. L. Schaefer and L. A. Archer, *J. Mater. Chem.*, 2012, **22**, 4066–4072.
- 351 S. Choudhury, A. Agrawal, S. Wei, E. Jeng and L. A. Archer, *Chem. Mater.*, 2016, **28**, 2147–2157.
- 352 Y. Liu, D. Lin, P. Y. Yuen, K. Liu, J. Xie, R. H. Dauskardt and Y. Cui, *Adv. Mater.*, 2017, **29**, 1605531.
- 353 N. W. Li, Y. X. Yin, C. P. Yang and Y. G. Guo, *Adv. Mater.*, 2016, **28**, 1853–1858.
- 354 G. Ma, Z. Wen, M. Wu, C. Shen, Q. Wang, J. Jin and X. Wu, *Chem. Commun.*, 2014, **50**, 14209–14212.
- 355 T. Zhang and H. Zhou, *Nat. Commun.*, 2013, **4**, 1817.
- 356 Z. Tu, S. Choudhury, M. J. Zachman, S. Wei, K. Zhang, L. F. Kourkoutis and L. A. Archer, *Nat. Energy*, 2018, **3**, 310.
- 357 X. Liang, Q. Pang, I. R. Kochetkov, M. S. Sempere, H. Huang, X. Sun and L. F. Nazar, *Nat. Energy*, 2017, **2**, 17119.
- 358 K. Yan, Z. Lu, H.-W. Lee, F. Xiong, P.-C. Hsu, Y. Li, J. Zhao, S. Chu and Y. Cui, *Nat. Energy*, 2016, **1**, 16010.
- 359 C. Yang, Y. Yao, S. He, H. Xie, E. Hitz and L. Hu, *Adv. Mater.*, 2017, **29**, 1702714.
- 360 S. Jiao, J. Zheng, Q. Li, X. Li, M. H. Engelhard, R. Cao, J.-G. Zhang and W. Xu, *Joule*, 2018, **2**, 110–124.
- 361 W. Guo, S. Liu, X. Guan, X. Zhang, X. Liu and J. Luo, *Adv. Energy Mater.*, 2019, 1900193.
- 362 G. Yasin, M. Arif, T. Mehtab, X. Lu, D. Yu, N. Muhammad, M. Tariq Nazir and H. Song, *Energy Storage Mater.*, 2020, **25**, 644–678.
- 363 H. Yang, C. Guo, A. Naveed, J. Lei, J. Yang, Y. Nuli and J. Wang, *Energy Storage Mater.*, 2018, **14**, 199–221.
- 364 C. Yang, L. Zhang, B. Liu, S. Xu, T. Hamann, D. McOwen, J. Dai, W. Luo, Y. Gong and E. D. Wachsman, *Proc. Natl. Acad. Sci. U. S. A.*, 2018, **115**, 3770–3775.
- 365 S. Xu, D. W. McOwen, C. Wang, L. Zhang, W. Luo, C. Chen, Y. Li, Y. Gong, J. Dai and Y. Kuang, *Nano Lett.*, 2018, **18**, 3926–3933.
- 366 C. Yang, H. Xie, W. Ping, K. Fu, B. Liu, J. Rao, J. Dai, C. Wang, G. Pastel and L. Hu, *Adv. Mater.*, 2019, **31**, 1804815.
- 367 T. Krauskopf, B. Mogwitz, C. Rosenbach, W. G. Zeier and J. Janek, *Adv. Energy Mater.*, 2019, **9**, 1902568.
- 368 Y. Gu, H. Y. Xu, X. G. Zhang, W. W. Wang, J. W. He, S. Tang, J. W. Yan, D. Y. Wu, M. S. Zheng and Q. F. Dong, *Angew. Chem., Int. Ed.*, 2019, **58**, 3092–3096.
- 369 P. Zou, Y. Wang, S.-W. Chiang, X. Wang, F. Kang and C. Yang, *Nat. Commun.*, 2018, **9**, 464.
- 370 K. H. Chen, A. J. Sanchez, E. Kazyak, A. L. Davis and N. P. Dasgupta, *Adv. Energy Mater.*, 2019, **9**, 1802534.
- 371 H. Liu, E. Wang, Q. Zhang, Y. Ren, X. Guo, L. Wang, G. Li and H. Yu, *Energy Storage Mater.*, 2019, **17**, 253–259.
- 372 X. Ma, Z. Liu and H. Chen, *Nano Energy*, 2019, **59**, 500–507.
- 373 X.-Y. Yue, W.-W. Wang, Q.-C. Wang, J.-K. Meng, X.-X. Wang, Y. Song, Z.-W. Fu, X.-J. Wu and Y.-N. Zhou, *Energy Storage Mater.*, 2019, **21**, 180–189.
- 374 K. R. Adair, M. Iqbal, C. Wang, Y. Zhao, M. N. Banis, R. Li, L. Zhang, R. Yang, S. Lu and X. Sun, *Nano Energy*, 2018, **54**, 375–382.
- 375 X.-Y. Yue, W.-W. Wang, Q.-C. Wang, J.-K. Meng, Z.-Q. Zhang, X.-J. Wu, X.-Q. Yang and Y.-N. Zhou, *Energy Storage Mater.*, 2018, **14**, 335–344.
- 376 K. Huang, Z. Li, Q. Xu, H. Liu, H. Li and Y. Wang, *Adv. Energy Mater.*, 2019, 1900853.
- 377 H. Duan, J. Zhang, X. Chen, X.-D. Zhang, J.-Y. Li, L.-B. Huang, X. Zhang, J.-L. Shi, Y.-X. Yin and Q. Zhang, *J. Am. Chem. Soc.*, 2018, **140**, 18051–18057.
- 378 J. Pu, J. Li, K. Zhang, T. Zhang, C. Li, H. Ma, J. Zhu, P. V. Braun, J. Lu and H. Zhang, *Nat. Commun.*, 2019, **10**, 1896.
- 379 J. Li, P. Zou, S. W. Chiang, W. Yao, Y. Wang, P. Liu, C. Liang, F. Kang and C. Yang, *Energy Storage Mater.*, 2020, **24**, 700–706.
- 380 Y. Cheng, X. Ke, Y. Chen, X. Huang, Z. Shi and Z. Guo, *Nano Energy*, 2019, **63**, 103854.
- 381 J. Zhu, J. Chen, Y. Luo, S. Sun, L. Qin, H. Xu, P. Zhang, W. Zhang, W. Tian and Z. Sun, *Energy Storage Mater.*, 2019, **23**, 539–546.
- 382 C. Niu, H. Pan, W. Xu, J. Xiao, J.-G. Zhang, L. Luo, C. Wang, D. Mei, J. Meng and X. Wang, *Nat. Nanotechnol.*, 2019, **14**, 594.
- 383 Y. Xu, T. Li, L. Wang and Y. Kang, *Adv. Mater.*, 2019, **31**, 1901662, DOI: 10.1002/adma.201901662.
- 384 J. Zheng, Q. Zhao, X. Liu, T. Tang, D. C. Bock, A. M. Bruck, K. R. Tallman, L. M. Housel, A. M. Kiss and A. C. Marschilok, *ACS Energy Lett.*, 2018, **4**, 271–275.
- 385 W. Chang, J. H. Park and D. A. Steingart, *Nano Lett.*, 2018, **18**, 7066–7074.
- 386 X. Q. Zhang, X. Chen, R. Xu, X. B. Cheng, H. J. Peng, R. Zhang, J. Q. Huang and Q. Zhang, *Angew. Chem., Int. Ed.*, 2017, **56**, 14207–14211.
- 387 R. Rupp and A. Vlad, *J. Electrochem. Soc.*, 2019, **166**, A3122–A3131.
- 388 P. Albertus, S. Babinec, S. Litzelman and A. Newman, *Nat. Energy*, 2018, **3**, 16–21.
- 389 K. G. Gallagher, S. E. Trask, C. Bauer, T. Woehrle, S. F. Lux, M. Tschech, P. Lamp, B. J. Polzin, S. Ha and B. Long, *J. Electrochem. Soc.*, 2016, **163**, A138–A149.
- 390 M. Armand and J. M. Tarascon, *Nature*, 2008, **451**, 652.
- 391 J. Liu, Z. Bao, Y. Cui, E. J. Dufek, J. B. Goodenough, P. Khalifah, Q. Li, B. Y. Liaw, P. Liu and A. Manthiram, *Nat. Energy*, 2019, **4**, 180–186.
- 392 X.-B. Cheng, C. Yan, J.-Q. Huang, P. Li, L. Zhu, L. Zhao, Y. Zhang, W. Zhu, S.-T. Yang and Q. Zhang, *Energy Storage Mater.*, 2017, **6**, 18–25.
- 393 C. Niu, H. Lee, S. Chen, Q. Li, J. Du, W. Xu, J.-G. Zhang, M. S. Whittingham, J. Xiao and J. Liu, *Nat. Energy*, 2019, **4**, 551–559.
- 394 A.-R. O. Raji, R. Villegas Salvatierra, N. D. Kim, X. Fan, Y. Li, G. A. L. Silva, J. Sha and J. M. Tour, *ACS Nano*, 2017, **11**, 6362–6369.
- 395 X. Fan, L. Chen, X. Ji, T. Deng, S. Hou, J. Chen, J. Zheng, F. Wang, J. Jiang and K. Xu, *Chem*, 2018, **4**, 174–185.
- 396 X. Fan, L. Chen, O. Borodin, X. Ji, J. Chen, S. Hou, T. Deng, J. Zheng, C. Yang and S.-C. Liou, *Nat. Nanotechnol.*, 2018, **13**, 715–722.

- 397 F. Qiu, X. Li, H. Deng, D. Wang, X. Mu, P. He and H. Zhou, *Adv. Energy Mater.*, 2019, **9**, 1803372.
- 398 Y. Guo, P. Niu, Y. Liu, Y. Ouyang, D. Li, T. Zhai, H. Li and Y. Cui, *Adv. Mater.*, 2019, **31**, 1900342.
- 399 T. Wang, P. Zhai, D. Legut, L. Wang, X. Liu, B. Li, C. Dong, Y. Fan, Y. Gong and Q. Zhang, *Adv. Energy Mater.*, 2019, **9**, 1804000.
- 400 H. Wang, Y. Li, Y. Li, Y. Liu, D. Lin, C. Zhu, G. Chen, A. Yang, K. Yan and H. Chen, *Nano Lett.*, 2019, **19**, 1326–1335.
- 401 P. Zou, Y. Wang, S.-W. Chiang, X. Wang, F. Kang and C. Yang, *Nat. Commun.*, 2018, **9**, 1–9.
- 402 G. Zheng, S. W. Lee, Z. Liang, H.-W. Lee, K. Yan, H. Yao, H. Wang, W. Li, S. Chu and Y. Cui, *Nat. Nanotechnol.*, 2014, **9**, 618–623.
- 403 T.-T. Zuo, Y.-X. Yin, S.-H. Wang, P.-F. Wang, X. Yang, J. Liu, C.-P. Yang and Y.-G. Guo, *Nano Lett.*, 2018, **18**, 297–301.
- 404 H. Ye, Y.-X. Yin, S.-F. Zhang, Y. Shi, L. Liu, X.-X. Zeng, R. Wen, Y.-G. Guo and L.-J. Wan, *Nano Energy*, 2017, **36**, 411–417.
- 405 Z. Huang, C. Zhang, W. Lv, G. Zhou, Y. Zhang, Y. Deng, H. Wu, F. Kang and Q.-H. Yang, *J. Mater. Chem. A*, 2019, **7**, 727–732.
- 406 J. Luo, C. C. Fang and N. L. Wu, *Adv. Energy Mater.*, 2018, **8**, 1701482.
- 407 L.-L. Lu, J. Ge, J.-N. Yang, S.-M. Chen, H.-B. Yao, F. Zhou and S.-H. Yu, *Nano Lett.*, 2016, **16**, 4431–4437.
- 408 R. Xu, Y. Xiao, R. Zhang, X. B. Cheng, C. Z. Zhao, X. Q. Zhang, C. Yan, Q. Zhang and J. Q. Huang, *Adv. Mater.*, 2019, **31**, 1808392.
- 409 Z. Huang, G. Zhou, W. Lv, Y. Deng, Y. Zhang, C. Zhang, F. Kang and Q.-H. Yang, *Nano Energy*, 2019, **61**, 47–53.
- 410 S. H. Wang, Y. X. Yin, T. T. Zuo, W. Dong, J. Y. Li, J. L. Shi, C. H. Zhang, N. W. Li, C. J. Li and Y. G. Guo, *Adv. Mater.*, 2017, **29**, 1703729.
- 411 S. Liu, X. Xia, Y. Zhong, S. Deng, Z. Yao, L. Zhang, X. B. Cheng, X. Wang, Q. Zhang and J. Tu, *Adv. Energy Mater.*, 2018, **8**, 1702322.
- 412 C.-P. Yang, Y.-X. Yin, S.-F. Zhang, N.-W. Li and Y.-G. Guo, *Nat. Commun.*, 2015, **6**, 1–9.
- 413 H. Ye, S. Xin, Y.-X. Yin, J.-Y. Li, Y.-G. Guo and L.-J. Wan, *J. Am. Chem. Soc.*, 2017, **139**, 5916–5922.
- 414 E. Markevich, G. Salitra, F. Chesneau, M. Schmidt and D. Aurbach, *ACS Energy Lett.*, 2017, **2**, 1321–1326.
- 415 Y. Gao, Y. Zhao, Y. C. Li, Q. Huang, T. E. Mallouk and D. Wang, *J. Am. Chem. Soc.*, 2017, **139**, 15288–15291.
- 416 T. Zhou, Y. Zhao, J. W. Choi and A. Coskun, *Angew. Chem., Int. Ed.*, 2019, **58**, 16795–16799.
- 417 Z. Zhang, Z. Peng, J. Zheng, S. Wang, Z. Liu, Y. Bi, Y. Chen, G. Wu, H. Li and P. Cui, *J. Mater. Chem. A*, 2017, **5**, 9339–9349.
- 418 K. Yan, Z. Lu, H.-W. Lee, F. Xiong, P.-C. Hsu, Y. Li, J. Zhao, S. Chu and Y. Cui, *Nat. Energy*, 2016, **1**, 1–8.
- 419 R. Zhang, X. R. Chen, X. Chen, X. B. Cheng, X. Q. Zhang, C. Yan and Q. Zhang, *Angew. Chem., Int. Ed.*, 2017, **56**, 7764–7768.
- 420 X. B. Cheng, T. Z. Hou, R. Zhang, H. J. Peng, C. Z. Zhao, J. Q. Huang and Q. Zhang, *Adv. Mater.*, 2016, **28**, 2888–2895.
- 421 H. Zhao, D. Lei, Y. B. He, Y. Yuan, Q. Yun, B. Ni, W. Lv, B. Li, Q. H. Yang and F. Kang, *Adv. Energy Mater.*, 2018, **8**, 1800266.
- 422 Z. Liang, G. Zheng, C. Liu, N. Liu, W. Li, K. Yan, H. Yao, P.-C. Hsu, S. Chu and Y. Cui, *Nano Lett.*, 2015, **15**, 2910–2916.
- 423 G. Zheng, C. Wang, A. Pei, J. Lopez, F. Shi, Z. Chen, A. D. Sendek, H.-W. Lee, Z. Lu and H. Schneider, *ACS Energy Lett.*, 2016, **1**, 1247–1255.
- 424 W. Liu, D. Lin, A. Pei and Y. Cui, *J. Am. Chem. Soc.*, 2016, **138**, 15443–15450.
- 425 Q. Li, S. Zhu and Y. Lu, *Adv. Funct. Mater.*, 2017, **27**, 1606422.
- 426 C. Zhang, R. Lyu, W. Lv, H. Li, W. Jiang, J. Li, S. Gu, G. Zhou, Z. Huang and Y. Zhang, *Adv. Mater.*, 2019, **31**, 1904991.
- 427 K. Yan, B. Sun, P. Munroe and G. Wang, *Energy Storage Mater.*, 2018, **11**, 127–133.
- 428 K. Yan, H.-W. Lee, T. Gao, G. Zheng, H. Yao, H. Wang, Z. Lu, Y. Zhou, Z. Liang and Z. Liu, *Nano Lett.*, 2014, **14**, 6016–6022.
- 429 Z. Zhang, X. Xu, S. Wang, Z. Peng, M. Liu, J. Zhou, C. Shen and D. Wang, *ACS Appl. Mater. Interfaces*, 2016, **8**, 26801–26808.
- 430 Z. Fang, Q. Ma, P. Liu, J. Ma, Y.-S. Hu, Z. Zhou, H. Li, X. Huang and L. Chen, *ACS Appl. Mater. Interfaces*, 2017, **9**, 4282–4289.
- 431 Q. Yun, Y. B. He, W. Lv, Y. Zhao, B. Li, F. Kang and Q. H. Yang, *Adv. Mater.*, 2016, **28**, 6932–6939.
- 432 Z. L. Brown, S. Jurng and B. L. Lucht, *J. Electrochem. Soc.*, 2017, **164**, A2186.
- 433 L. Ma, M. S. Kim and L. A. Archer, *Chem. Mater.*, 2017, **29**, 4181–4189.
- 434 X. Ji, D.-Y. Liu, D. G. Prendiville, Y. Zhang, X. Liu and G. D. Stucky, *Nano Today*, 2012, **7**, 10–20.
- 435 R. Zhang, X. B. Cheng, C. Z. Zhao, H. J. Peng, J. L. Shi, J. Q. Huang, J. Wang, F. Wei and Q. Zhang, *Adv. Mater.*, 2016, **28**, 2155–2162.
- 436 W. Luo, L. Zhou, K. Fu, Z. Yang, J. Wan, M. Manno, Y. Yao, H. Zhu, B. Yang and L. Hu, *Nano Lett.*, 2015, **15**, 6149–6154.
- 437 W. Liu, W. Li, D. Zhuo, G. Zheng, Z. Lu, K. Liu and Y. Cui, *ACS Cent. Sci.*, 2017, **3**, 135–140.
- 438 Y. Gao, Z. Yan, J. L. Gray, X. He, D. Wang, T. Chen, Q. Huang, Y. C. Li, H. Wang and S. H. Kim, *Nat. Mater.*, 2019, **18**, 384.
- 439 G. Zheng, S. W. Lee, Z. Liang, H.-W. Lee, K. Yan, H. Yao, H. Wang, W. Li, S. Chu and Y. Cui, *Nat. Nanotechnol.*, 2014, **9**, 618.